MECHANISMS AND MODELS

OF SEISMIC ATTENUATION

A Thesis Submitted to the College of

Graduate and Postdoctoral Studies

In Partial Fulfillment of the Requirements

For the Degree of Doctor of Philosophy

In

Geophysics

In the Department of Geological Sciences

University of Saskatchewan

Saskatoon

By

WUBING DENG

PERMISSION TO USE

In presenting this thesis in partial fulfilment of the requirements for a Postgraduate degree from the University of Saskatchewan, I agree that the Libraries of this University may make it freely available for inspection. I further agree that permission for copying of this thesis in any manner, in whole or in part, for scholarly purposes may be granted by the professor or professors who supervised my thesis work or, in their absence, by the Head of the Department or the Dean of the College in which my thesis work was done. It is understood that any copying or publication or use of this thesis/dissertation or parts thereof for financial gain shall not be allowed without my written permission. It is also understood that due recognition shall be given to me and to the University of Saskatchewan in any scholarly use which may be made of any material in my thesis.

Requests for permission to copy or to make other use of material in this thesis in whole or part should be addressed to:

Head of the Department of Geological Sciences

University of Saskatchewan

Saskatoon, Saskatchewan (S7N 5E2)

ABSTRACT

Seismic attenuation is a subject of great interest for both industry and academia. In exploration seismology, wave attenuation must be well understood for interpreting seismic data and laboratory experiments with rocks, and improving the quality and resolution of reflection imaging of the subsurface. To achieve such understanding, mechanisms of seismic attenuation and the associated physical models need to be studied in detail. This dissertation focuses on analyzing several attenuation mechanisms and building first-principle mathematical models for them. The effects of seismic attenuation can be broadly subdivided into two groups: 1) caused by inelasticity of the material and 2) caused by small-scale elastic structures of the material or subsurface. From the first of these groups, I study solid viscosity and internal friction due to squirt flows and wave-induced fluid flows (WIFF) at different scales. This approach is based on a new rheological law called the General Linear Solid (GLS) and recently developed to describe macroscopic inelastic effects in multiphase solids. The GLS is a model composed by time/frequency independent parameters and based on Lagrangian continuum mechanics. By utilizing the GLS framework, I extend the well known-model called the Standard Linear Solid (SLS) to include internal inertial forces, which explains the primary wave and reveals additional highly diffusive wave modes. I also use the GLS to model P-waves with squirt flow dissipation by different configurations of the density, moduli, drag and solid viscosity matrices.

Seismic wave attenuation may not only be caused by inelastic properties but also by elastic processes such as reflectivity and scattering. I examine two types of such effects of the elastic structure of the material. First, in a laboratory experiment with several rock types, there is a modest influence of sample size on the measured level of attenuation and modulus

dispersion. Second, in a field experiment aimed at measuring Q from seismic reflectivity, the effect of elastic layering can be extremely strong and even completely equivalent to that of the Q. An important general observation from this study is that amplitude decays and phase delays measured from reflection seismic data can always be interpreted as either caused by inelasticity or by small-scale elastic structures.

An important complementary goal of studying the mechanisms and effects of seismic attenuation consists in correcting for its effects in seismic records and increasing the resolution of seismic images. In this dissertation, I briefly consider attenuation-correction techniques and develop a novel method for such correction by using time-domain deconvolution. Synthetic and field data are used to illustrate and test the performance of this approach.

ACKNOWLEDGMENTS

A five-year PhD study was like a blink of an eye, during which I have experienced five autumns and five winters in Saskatoon. I still remember what my supervisor Dr. Igor Morozov asked me before I came to Canada. He said that the weather, especially the winter, in Saskatoon would be very severe and asked whether I was ready to come and stay in Saskatoon for at least four years. The winter is indeed so chilly and long, but I found myself to love it more than be afraid of it. Saskatoon explained to me how the severe winter looks like and showed me what a gorgeous summer and lovely autumn it has. Scientific research is so alike Saskatoon's weather. Fortunately, Igor was/is always there for help. Not only did he teach me how to do research in a rigorous and scientific manner but also helped me build up confidence. At the GeoConvention 2013 in Calgary, I was the last presenter of the last day of the conference. Almost all people were heading back so that only five people attended my presentation. I couldn't tell how disappointed I was and I was becoming even more nervous. Those 20 minutes were just suffering. I can feel how bad my presentation was. However, Igor still gave a courageous smile and told me that I was doing very well. I was so moved by his encouragement. This was not the only moment that I felt being encouraged. During these years, Igor taught me so well that I have become more and more confident. I would like to send my full hearted grateful to Igor.

I might be one of the luckiest students to have great supervisors during my graduate study. I thank the supervisor of my MSc study, Dr. Prof. Liguo Han at Jilin University. Without his help, I might not have been able to pursue my PhD. Actually, I never thought about coming to Canada for my PhD until Dr. Han told me that I should think more and further about my academic achievement by doing a PhD program abroad. Without his help, I

might not be where I am today. The three years of Master's study supervised by Dr. Han found the basis of being a good researcher. He led me into the world of scientific research and taught me how to be self-motivated and co-operative individual. My first tutoring experience was also introduced by him, when I was a 2nd year undergraduate student. This experience was so valuable that it helped me a lot in TA positions at University of Saskatchewan.

I am grateful to Nancy Williams, who always treats me as her own child. Her words always encourage me. Her master-level culinary skill made me have one more thing to look forward. Every Thanksgiving and Christmas Days were full of joy because of Nancy. It was cold outside in winter, but sweet and warm inside.

I am grateful to my external examiner Dr. Robert Nowack from Purdue University. He really carefully reviewed my thesis and gave so many informative comments and suggestions. Not only professional advices, Robert also showed me how wonderful the life can be if a man is passionate with life itself.

I thank Dr. Samuel Bulter for his kindness of teaching me whenever I had questions and enquiries. He taught me a lot, especially on the microscopic-scale fluid flow in a pipe, which will benefit my future research.

I thank Dr. Jim Merriam for teaching me the theory of geophysics inversion, which helped me enhance my understanding of seismic inversion.

I would like to thank Dr. Alexey Shevyakov for being the committee member since 2012. Alexey taught me that it is very important to get fully understandings of those mathematical formulae before using them.

I thank Dr. Yuanming Pan to be the Committee Chair for my defense.

I thank Dr. Zoltan Hajnal for the talks we have had, which inspired me a lot. He is also my role model. He still insists on research even though he is over 80.

I would also like to thank the members of our seismology group. I thank Amin Baharvand Ahmadi for the nice chats we have had at almost every lunch time, which helped me efficiently adapted myself for my PhD program. I thank Le Gao for her kindness of teaching me Linux and seismic processing software which helped make my PhD more efficient. I also would like to thank Mohamed Haiba, Yichuan Wang, Kamal Abo Jnah, and Osama El Badri for accompanying me in the office for last two years of my study.

Over the years, I developed good friendships with many Chinese people in Saskatoon. Xue Yong and Zhibang Lv were the first two people I met after I arrived in town. We have had so many wonderful moments together. Xue is always very thoughtful and planned a lot of interesting events for our weekends. Zhibang really knows how to make the daily life exciting, such as making beer, fishing and working out. Tengfei Cui comes from the same college in China as me; we always have a lot to talk about. Kai Zhou is a good talker and has a great sense of humor; we enjoyed the time for chatting and playing soccer. Special thanks are given to Xue Yong and her husband Lin Cao who took me to the hospital and accompanied me during my surgery, which made me not alone nor afraid. With my friends, I enjoyed the bright summers and survived in the chilly winters.

Last but not least, I want to give my deepest gratitude to my parents, without whom I won't be who I am. I also want to thank my elder brother who encouraged and supported me so much. My wife, Liu Wang, took really good care of our home with everything. Without her support and love, I wouldn't have accomplished my PhD.

SYMBOLS AND ABBREVIATIONS

Symbol	Definition
1D, 1-D	One-Dimensional
2D, 2-D	Two-Dimensional
3D, 3-D	Three-Dimensional
AVO	Amplitude Variation with Offset
DVO	Dispersion Variation with Offset
GLS	General Linear Solid
GSLS	Generalized Standard Linear Solid
ITD	Iterative Time-Domain Deconvolution
MB	Maxwell Body
PFE	Pore-Fluid Effect
Q	Quality factor
QVO	*Q* Variation with Offset
SLS	Standard Linear Solid
VE	Visco-Elastic
WIFF	Wave-Induced Fluid Flow

TABLE OF CONTENTS

LIST OF TABLES

LIST OF FIGURES

CHAPTER 1

INTRODUCTION

Seismic waves are subjected to the complicated structure and inelasticity of the Earth which modify the propagating waveforms. These modifications generally include a reduction of amplitude and many types of amplitude and phase variations due to the heterogeneity of the elastic structure. In this dissertation, I use the term “inelasticity” to denote any effects converting a portion of the mechanical energy of deformation into heat, without any specification of the mechanism of this energy loss. Within the broad group of inelastic phenomena, term “anelasticity” is often used to denote reversible deformations described by the broadly-used viscoelastic (VE) model, and term “plasticity” refers to irreversible material flows (Lakes, 2009). By contrast to inelastic phenomena, elastic processes such as geometrical spreading, refraction, and reflections within thin layering, conserve the total energy but cause variations of the waveforms recorded at a given location. Both inelastic and elastic effects generally lead to amplitude reductions and phase rotations of the seismic waveforms. Measurement of such amplitude and waveform variations can be beneficial, for example, for identifying hydrocarbons or zones of small-scale heterogeneity, or alternatively, these variations may sometimes be treated as undesirable effects and corrected for in reflection seismic data processing. In both cases, understanding of the physics and mechanisms of seismic attenuation is of crucial importance.

In most existing studies in both exploration and earthquake seismology, seismic attenuation is approximated by the VE model. However, as shown further in this dissertation, this model is formulated purely mathematically, and most physical mechanisms of attenuation in realistic media are not accurately represented by it. Without knowing the

physical mechanisms, the accuracy of the VE approximation is difficult to evaluate but often questionable. To better understand seismic attenuation, first-principle physics should always be utilized.

The goal of this dissertation is to rigorously study several realistic attenuation mechanisms and develop physically meaningful models based on the principles of continuum mechanics. With those new models, many types of deformation processes encountered in laboratory and field seismic experiments can be explained with confidence and at the level of detail that is not available from the VE model.

1.1 Objectives

In this study, I aim at overcoming the aforementioned limitations of the VE model by making two conceptual improvements to the existing theory of seismic attenuation: 1) employing the Lagrangian mechanics to understand the first principles of both elastic and inelastic processes, and 2) considering detailed effects of elastic structures affecting the attenuation and dispersion effects. The objective of this work is to develop physically meaningful, specific, and detailed models of wave-propagation effects including the dissipation of mechanical energy. These models should be suitable for predicting seismic-wave propagation in many inelastic materials and in realistic experimental environments.

After achieving certain progress in understanding the mechanics of seismic attenuation, the third objective of this dissertation is to utilize this understanding in reflection seismic data processing by developing a new method for compensating attenuation and dispersion effects in reflection seismic records.

1.2 Contributions

The main contributions of this dissertation include:

a) A novel theoretical framework for describing internal friction within materials that we call the General Linear Solid (GLS; Morozov and Deng, 2016a, b). I show that this framework incorporates most known attenuation mechanisms and has the potential for constructing detailed and rigorous models explaining many types of experimental data.

b) Based on the GLS framework, I develop several applications of the so-called Generalized Standard Linear Solid (GSLS) model, squirt flow model for porous rock, explanation of the "memory variables" broadly used in finite-difference modeling of waves in inelastic media (Deng and Morozov, 2016), studies of the effects of fine layering (Deng and Morozov, 2017).

c) A novel time-domain inverse filtering method for correcting reflection seismic datasets for attenuation effects and improving the resolution of reflection imaging (Deng and Morozov, *in review*, Geophysical Prospecting).

1.3 Structure of this dissertation

This dissertation is based on several recent publications (Deng and Morozov, 2014, 2016, in review, in revision, in preparation, and Morozov and Deng, 2016a, b). Each of these papers is introduced in the respective Chapter and somewhat modified for integration in this dissertation. In the present Chapter 1, I give the objectives and outline the general approach, anticipated results, and the significance of this research.

In Chapter 2, I review two fundamental approaches to modeling seismic-wave attenuation and dispersion: 1) the existing phenomenological model based on the concept of a quality factor Q, and 2) approaches based on physical explanations of these phenomena. The physical approaches focus on pore-flow processes at different scales and reflectivity and

scattering in several types of elastic structures.

In Chapter 3, I start by briefly reviewing the Lagrangian mechanics in application to macroscopic models of multi-phase solids and discuss its applications to inelastic systems. By using this method, I derive wave equations for several types of different inelastic models, including conventional VE models and Biot's poroelasticity, and visco-poroelasticity. All these systems are considered from a common viewpoint of the GLS rheology (Morozov and Deng, 2016a).

In Chapter 4, I introduce a new type of the GLS model for a porous, fluid-saturated medium with squirt flows. I show that within the seismic frequency band, the effects of squirt flows are equivalent to those of solid viscosity of the rock frame.

In addition to linear, multi-phase GLS models presented in the preceding chapters, in Chapter 5, I propose a single-phase model with nonlinear elastic moduli and viscosity. This nonlinear model is used to explain the direct waves and reflections in a highly-attenuating fluid. The results of this Chapter provide a novel, detailed interpretation of recent experiments with acoustic waves in Crisco vegetable shortening (Lines et al., 2014).

Chapter 6 continues the analysis of the effects of the elastic structure on attenuation and dispersion measurements. As a specific example, I consider a finely-layered structure and show that its effect may be indistinguishable from those of intrinsic attenuation, which are commonly explained by the quality factor Q.

In Chapter 7, I address a question complementary to those discussed in the preceding chapters: assuming that we are able to model seismic-wave attenuation and dispersion within the medium, how can we reduce its detrimental effects on reflection seismic images? Based on our recent generalized approach of "A-compensation" (Morozov et al., in revision), I

propose a time-domain deconvolution offering some unique capabilities for enhancing seismic images.

Finally, in the concluding Chapter 8, I summarize and integrate the most important results of this dissertation and suggest several directions for the future research.

CHAPTER 2

ATTENUATION AND DISPERSION OF OSCILLATIONS IN EARTH MATERIALS

Due to the inelasticity of the Earth materials, amplitudes of seismic signals are reduced and their waveforms are distorted during wave propagation. The amplitude decay is also associated with a reduction of mechanical energy carried by the wave, which is usually described as “attenuation”. The waveform (phase) distortion is usually expressed by broadening (dispersion) of the wave packet, which can also be explained by different frequency components of wave traveling at different phase velocities in a lossy medium.

The amplitude decay and dispersion in imperfect media are concomitant, in the sense that a wave exhibiting a decaying amplitude is always dispersive and vice versa. In practical seismology (including theoretical, field and laboratory observations, interpretation, and seismic data processing), a phenomenological quantity called the quality factor (Q) is commonly used to describe these effects. However, several key questions remain unanswered by this quantity, such as the required or possible frequency dependences of Q, its uniqueness and dependence on the procedure of its measurement. Morozov and Baharvand Ahmadi (2015) gave a taxonomy and critical analysis of the concept of Q in exploration geophysics. They argued that the Q should generally be understood as an apparent property, i.e. attribute of a propagating wave or of the measurement procedure in the laboratory. Earlier, Morozov (2008, 2010) also discussed the concept of Q in many areas of earthquake seismology and its dependence on measurement procedures, such as laboratory set-up and geometric spreading in field measurements.

Thus, the physical characters of attenuation and dispersion processes need to be

carefully considered together with their models and phenomenology. In this Chapter, I discuss the general principles of these physical mechanisms and models. I start from a brief overview of the background on seismic attenuation (section 2.1), then I introduce the conventional, phenomenological *Q* model (section 2.2) and in section 2.3, I overview some of the current physical models used to describe seismic attenuation.

2.1 Background on Seismic Attenuation

The concept of seismic attenuation always involves some type of measurements of the relative decay of mechanical energy stored in an oscillation process. This energy decay can be observed as a spatial logarithmic decrement of amplitude for a traveling wave, as a temporal decay of a standing wave (free oscillation), or as broadening of a spectral peak and/or strain-stress phase lag in a stationary (subresonant) forced-oscillation test with a rock sample in the laboratory. Because attenuation always implies a measurement of energy, two fundamental types of attenuation are recognized based on the role of this measurement: intrinsic and elastic attenuation. The intrinsic attenuation describes the net loss of mechanical energy converted into heat, which is due to the inelasticity of the medium. The elastic attenuation represents the fraction of mechanical energy that is preserved but diverted from the specific observation, for example, by broadening (dispersion) of a wave onset caused by scattering. Conventionally, both the intrinsic attenuation and scattering on small-scale heterogeneities are described by inverse *Q*-factors $Q_{\text{intrinsic}}^{-1}$ and $Q_{\text{scattering}}^{-1}$, which are combined in the total observed inverse *Q* factor (next subsection) by the broadly used relation (Wu, 1985):

$$Q_{\text{observed}}^{-1} = Q_{\text{intrinsic}}^{-1} + Q_{\text{scattering}}^{-1}. \tag{2.1}$$

Separation of the intrinsic and scattering contributions to attenuation is a complex

subject that is beyond the scope of this dissertation. To point out the key challenges of this separation, note that only the sum Q^{-1}_{observed} can be measured, for example, by using the slope of the logarithmic scale of the spectral ratio curve (Hauge, 1981). The two terms $Q^{-1}_{\text{intrinsic}}$ and $Q^{-1}_{\text{scattering}}$ can only be separated based on their expected frequency dependences or by assuming some specific form of the (elastic) geometric spreading for the waves involved in the measurement (Wu, 1985), or some specific model of scattering. However, Morozov (2010) argued that in practice, the background models cannot be sufficiently accurate, and the inferred $Q^{-1}_{\text{scattering}}$ is always affected by residual geometric spreading (remaining after corrections based on imperfect background models). It is difficult to isolate the scattering Q from geometric spreading, because both of them are caused by the averaged small-scale structure and have similar effects on recorded seismograms (Morozov, 2010). The separation between $Q^{-1}_{\text{intrinsic}}$ and $Q^{-1}_{\text{scattering}}$ in eq. (2.1) contains a subjective element and depends on the degree of detail of the employed model of elastic structure. In particular, $Q^{-1}_{\text{scattering}}$ can include "fluctuation Q" caused by limited spatial sampling of fine layering (Morozov and Baharvand Ahmadi, 2015). Examples of such "fluctuation Q" in a 1-D layered structure are given in Chapter 6.

In Chapters 2 to 5, I focus on the models for the intrinsic attenuation $Q^{-1}_{\text{intrinsic}}$. It is generally believed that in upper-crustal and particularly sedimentary environments, wave attenuation is primarily caused by fractures and viscous fluid flows in the cracks and pores within the material. Chapman (2003) demonstrates that larger fractures (at mesoscopic scales rather than grain scale usually sampled in laboratory experiments) can result in frequency-dependent anisotropic responses within the seismic frequency band (1 to 500 Hz) and lower

characteristic frequencies for squirt-flow (i.e. caused by fluid flows within cracks) attenuation. Fractures not only cause anisotropy but also heterogeneity. With a wide range of possible types of heterogeneity, a range of relaxation frequencies can be expected, which means that heterogeneity of the microstructure of the material should cause broad attenuation spectra (Masson and Pride, 2007).

Fluid viscosity is an important physical factor of seismic wave attenuation and dispersion in sedimentary rocks, which is commonly caused by pore-fluid effects (PFEs). PFEs are usually classified into three different scales: macroscopic, microscopic and mesoscopic. Macroscopic effects are defined as those occurring on the spatial scale much shorter than the seismic wavelength but longer than any heterogeneity of the material. The well-known model of macroscopic PFE is Biot's poroelasticity, which describes the global flow of a viscous fluid within the pores (Biot, 1956). The fluid flow is considered as quasi-uniform at the macroscopic scale and insensitive to any microstructure of the material. This mechanism dominates the attenuation near "Biot's characteristic frequency", which is usually located within the higher-frequency ultrasonic frequency band (> 20 kHz).

At the opposite, microscopic scale, the PFEs are specifically related to the granularity of the material. An important mechanism of such kind is caused by the so-called squirt flows occurring within rocks containing near-planar and compliant cracks often called "soft" pores. The fluid within the soft pores is squeezed in and out of them, and viscous-fluid friction causes attenuation of the wave passing through the rock (Murphy et al., 1986). This process produces a considerable amount of attenuation which can occur at sonic (20 to 20,000 Hz) frequencies (Chapman, 2003; Müller et al, 2010).

The mesoscale of PFE is intermediate between micro and macro scales and refers to

pore flows within rock with larger-scale internal heterogeneity (such as containing pockets of different fluids or gas) but still at the scale much shorter than the seismic wavelength. This scale has been recognized as the most important for seismic attenuation, and pore-fluid flows at this scale are also called the wave-induced fluid flows (WIFFs). WIFFs have been illustrated by many models, each emphasizing different types of heterogeneity. For example, a class of WIFF models considers a single fluid in a material with heterogeneous distribution of poroelastic properties (Rubino and Holliger, 2013). Another type of WIFF assumes a homogenous lithology saturated by contrasting immiscible fluids, such as pockets of oil, brine, or gas (White et al., 1975; Pride et al., 2004; Beresnev, 2014). At the mesoscopic scale, combinations of such factors can generate broad frequency spectra of attenuation effects.

With the exception of Biot's poroelasticity, the final products of PFE models consist in analytic derivations or numerical modeling of the frequency-dependent effective viscoelastic (VE) moduli (Gurevich et al., 2010; Quintal et al., 2012; Rubino et al., 2013). Layered mesoscopic heterogeneities or those with preferred orientation cause frequency-dependent anisotropy of the resulting effective moduli (Chapman, 2003). O'Connell (1984), Murphy et al. (1986), Dvorkin et al (1994) and Gurevich et al. (2010) also utilize the frequency-dependent fluid bulk and shear moduli to describe the squirt-flow mechanism. Pride et al. (2004) introduce a frequency-dependent transport coefficient to describe the PFE at mesoscopic scale in the differential equations of motion, but ultimately also derive effective VE moduli to describe the medium.

Although the VE representation provides familiar ways for numerical modeling in the frequency domain and high flexibility of the models in fitting experimental data, it also has significant limitations. The VE picture of materials is not as simple and intuitive as it may

seem. The key limitation of this picture for porous rock is that, as argued by Morozov (2015), Morozov and Baharvand Ahmadi (2015), and Morozov and Deng (2016b), multiple moduli exist for fast and slow traveling P waves, and also for every standing-wave within a rock sample in a subresonant attenuation experiment. Morozov (2015 and in review) showed that the VE moduli derived from wave velocities in field or ultrasonic laboratory experiments (for example, Young's modulus $E = \rho V^2$ for an extensional-mode wave within a rod) are generally different from the moduli inferred from stress/strain ratios ($E = \sigma/\varepsilon$ within the same rod). In addition, the different "moduli" that can be inferred for poroelastic rock (P-wave, S-wave, Young's, bulk, and Poisson's ratio) are not automatically related by the relations known for elastic materials (White, 1986; Morozov, 2015). Multiple VE moduli are also needed to make the VE model "Biot-consistent", i.e. able to describe the coupling between the rock frame and pore fluid (Thomsen, 1985). Also, as shown by Berryman and Wang (2000) and Pride et al. (2004), two slow P-waves should result from PFE with dual porosity (such as in rock with squirt flows).

Although VE models can approximate both fast and slow P-waves by carefully constructing multiple memory variables, they do not naturally contain Biot-consistency and predict the existence of those P-waves from material properties. Conversely, VE models usually postulate special material properties in order to explain the slow waves. For example, Carcione and Gurevich (2011) successfully approximate the fast P-wave mode for squirt-flow dissipation and the slow P-wave for Biot's global flow, but this description is quite elaborate (containing five Zener's solids and a different set of them for slow waves), but the second slow P-wave due to squirt flow is still absent completely. Another limitation of the VE approximation is the complexity and artificial character of wave modeling in media with

broad attenuation spectrum, where many memory variables are needed.

2.2 Phenomenological Description of Attenuation

The most common way to account for attenuation effects in seismic data is the phenomenological dimensionless quantity *Q*, which is called the quality factor. This quantity is expected to lump together all mechanisms of attenuation without considering their detail. A general definition of *Q* is given by the ratio of the peak stored elastic energy *E* to the energy δE lost in one cycle of harmonic oscillation (Aki and Richards, 2002):

$$Q(f) = 2\pi \frac{E}{\delta E}. \tag{2.2}$$

A low value of *Q* means strong attenuation and a high *Q* indicates weak attenuation. For example, for a wave in a weathered sedimentary rock (with strong attenuation), the typical *Q* is around 30, whereas for a wave in granite (weak attenuation), the *Q* is about 1000 (Sheriff and Geldart, 1995).

To obtain the observational effects of *Q*, consider a plane wave

$$u = A\exp\left[-i\left(\omega t - k^* x\right)\right], \tag{2.3}$$

where *u* is the particle displacement, *A* is the amplitude, $\omega = 2\pi f$ is the angular frequency, *f* is the frequency, *t* denotes the time, *x* is the travel distance, and k^* is the complex wavenumber:

$$k^* = k(\omega) + i\alpha(\omega). \tag{2.4}$$

Here, *k* is the frequency-dependent wavenumber and α is the frequency-dependent attenuation coefficient, which can be measured by the logarithmic spatial decrement of the amplitude. This decrement can be due to geometric spreading, scattering and intrinsic attenuation, and other factors (Baharvand Ahmadi and Morozov, 2013). From the

definition (2.2) and assuming a linear stress-strain relation and $Q \gg 1$, the Q for a propagating wavelet can be written as (Bourbié et al., 1987; Aki and Richards, 2002)

$$Q(\omega) = \frac{\omega}{2\alpha c} = \frac{\pi}{\alpha \lambda}, \tag{2.5}$$

where $c = \omega / k$ is the phase velocity at frequency *f*. Therefore, in terms of *Q*, the plane-wave displacement can be written as,

$$u = A \exp\left(-\frac{\omega}{2Qc} x \right) \cdot \exp\left[-i(\omega t - k x) \right]. \tag{2.6}$$

This equation shows that with increasing travel distance, the amplitude of the plane wave decays exponentially, and this decay increases with frequency. For example, in Figure 2.1, after traveling a certain distance, the wavelet (blue line) amplitude decreases from 1 to around 0.2 (red line, Figure 2.1a). The peak frequency of the input source (blue line, Figure 2.1b) is shifted to lower frequencies (red line, Figure 2.1b). Attenuation and dispersion are concomitant, which means that frequency-dependent amplitude decay in eq. (2.6) is always associated with a frequency-dependent phase velocity *c* and vice versa (Aki and Richards, 2002). Figure 2.2 illustrates the phase velocity dispersion by three commonly-used models, which are Futtermann's (1962) and Kjartansson's (1979) constant-*Q* model and the near-constant-*Q* model by Liu et al. (1976), also called the Generalized Standard Linear Solid (GSLS). GSLS is a superposition of several Zener's (or Standard Linear Solid, SLS) solids (Zener, 1948). Figure 2.2 shows that the phase velocity increases with increasing frequencies. This is different from the case of an elastic-wave, in which the phase velocity is independent of frequency. The dispersion of phase velocity distorts the phase of the wavelet; for example, a zero-phase wavelet becomes increasingly phase-rotated with propagation time (red line in Figure 2.1a).

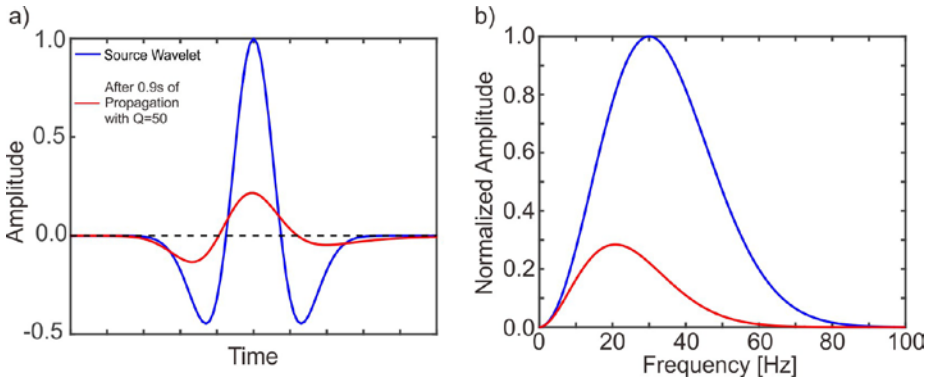

Figure 2.1 a) Time-domain waveform variation and b) frequency spectra changes due to inelasticity. The Q is selected to be 50.

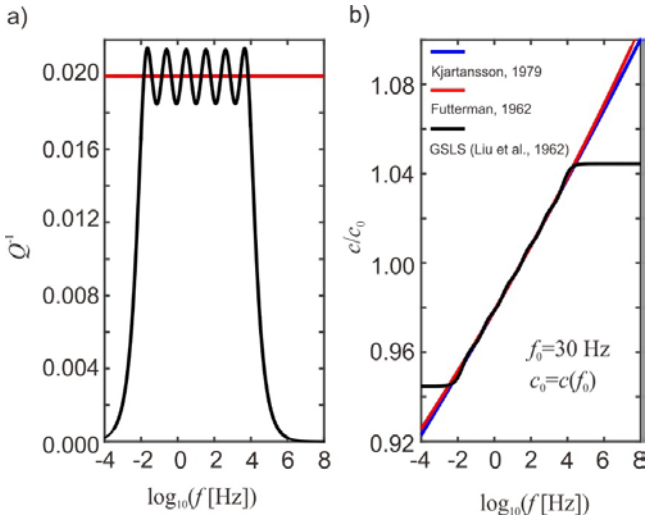

Figure 2.2. Constant Q models' a) inverse-Q spectra and corresponding b) phase velocity dispersion. The reference phase velocity c_0 is selected at reference frequency f_0 = 30 Hz.

Although the Q defined in eqs. (2.5) is a function of frequency, constant-Q or near-constant-Q models are often used for body waves (Varela et al., 1993; Blanch et al., 1995; Bohlen, 2002; Zhu et al, 2013). In reflection seismology, the frequency band is relatively narrow, and a constant Q^{-1} is usually viewed as a viable practical approximation. A near-constant Q^{-1} within a limited frequency band is always used in finite-difference waveform-modeling algorithms (Bohlen, 2002; Zhu et al, 2013). Generally, these constant- or near-constant-Q models are equivalent within the seismic frequency band (Figure 2.2), but they may vastly differ outside of this band and when expressed in the form of time-domain

equations.

Although widely used for describing seismic wave attenuation, the assumptions of constant- or near-constant-Q models have significant limitations. For example, laboratory experiments usually show frequency-dependent Q within and above the seismic frequency band (e.g., Spencer, 2013; Tisato and Quintal, 2013; Tisato et al, 2014; Pimienta et al, 2015a, 2015b). Also, phenomenological Q models only state the fact of attenuation but cannot help estimating the hydraulic or poroelastic properties responsible for it. For example, a reduced or even negative Q might be not only caused by inelasticity but also by some elastic structures, such as fine layering (White et al., 1975; Chapter 6 in this dissertation). Therefore, first-principle physical explanations are needed instead of (or in addition to) the phenomenological Q.

The key question of such a first-principle model is what property of the subsurface should be viewed as the physical cause of wave attenuation. Although Q-based approaches dominate today's attenuation studies and are often believed to be closely related to rheologic properties of the subsurface, Q cannot be viewed as a true property of the medium (Morozov and Baharvand Ahmadi, 2015). Definition (2.5) shows that Q is only a property of the traveling wave, similar to its angular frequency ω and wavelength λ. The Q may vary if a different traveling or standing wave mode is considered or when the source operates at a different frequency. Also note that in Figure 2.2 when $f \to 0$, Q^{-1} tends to be zero. There is no reason for Q^{-1} to automatically equal zero for zero frequency. The Q is a frequency-domain property, and consequently it cannot be localized in space (Morozov and Baharvand Ahmadi, 2015). It is also very difficult to construct consistent differential wave equation containing the Q (Knopoff, 1964), unless by utilizing artificial "memory variables" (e.g., Zhu

et al., 2013). Therefore, rather than assuming the *Q* to be a property of the medium, it is more appropriate to consider it as only a property of the wave, and try explaining it by physical mechanisms.

2.3 Physical Mechanisms of Attenuation

Reduction of oscillation amplitudes and dispersive waveforms can result from a variety of physical processes, and accordingly there exist numerous types of *Q*s (Morozov and Baharvand Ahmadi, 2015). In this section, I review some of these mechanisms relevant to porous fluid-saturated rock. Seismic attenuation can be caused by either linear or nonlinear mechanical mechanisms (Day et al., 1998; Coulman et al., 2013; Sleep and Nakata, 2017). For linear attenuation, the stress represents a linear combination of the strain and strain rate, whereas for nonlinear deformation, there exists no simple relation of this kind, and different wave modes may interact and transform during propagation. In this dissertation, only linear attenuation mechanisms are considered, with a small exception of the near-source zone discussed in Chapter 5.

The most general differentiation of such attenuation phenomena consists in the separation of elastic and inelastic processes. Elastic-attenuation processes are characterized by the conservation of the total mechanical energy of the medium in the process of its oscillation or wave propagation. In field experiments with propagating waves, such effects include the geometric spreading or scattering, or reflectivity on finely-layered structures (White et al., 1975; Aki, 1980; Morozov, 2010). Geometric spreading (GS), as the simplest case of which is the spherical divergence, is a phenomenon describing the loss of wave energy with increasing travel distance from the source. Scattering is another elastic process resulting in apparent attenuation caused by inhomogeneities of the medium. For a finely

layered structure, interferences of seismic reflections cause attenuation and dispersion, which may be misinterpreted as inelastic attenuation (Chapter 6).

Inelastic dissipation is considered a major contributor to Q^{-1} in most circumstances. However, dissipation of mechanical energy is only one measure of the process of internal mechanical friction within the material. The most common physical processes of friction include granular sliding friction, friction at cracks, thermoelasticity, and pore-fluid flow effects (Biot, 1956; Savage, 1966; Walsh, 1966; Mavko and Nur, 1979; Winkler et al., 1982; Murphy, 1982; Murphy et al., 1986). Of all these mechanisms, pore-fluid effects (PFEs) are of particular interest in exploration geophysics. PFE represents the physical phenomenon of internal friction of fluid flow relative to the solid due to pressure gradients caused by the passing waves. This mechanism is broadly accepted as a major cause of the observed seismic-wave attenuation (Pride et al., 2004; Müller et al, 2010; Rubino et al., 2013).

PFEs have been investigated at three different scales: macroscopic, mesoscopic, and microscopic. The attenuation and dispersion effects caused by global fluid flows at the macroscopic scale are theoretically described by Biot's poroelastic model (Biot, 1956; Bourbié et al., 1987). This model predicts two types of P-waves, which are the usual (also called primary, relatively fast and weakly attenuative) wave and the slow and diffusive secondary P-wave. The fast P-wave is commonly observed in both field and higher-frequency laboratory experiments. Slow P waves within short paths were observed in laboratory ultrasonic experiments by Plona (1980) and Bouzidi and Schmitt (2009), but they are generally viewed as unobservable in the field due to their diffusive nature. Biot's attenuation of fast P-wave is significant at frequencies of about 100 kHz, which is much higher than the seismic frequency band (up to 500 Hz). However, conversions between the

fast and slow P-waves occur on any heterogeneities, and consequently slow P-wave modes should actually be present in waves propagating within layered reflection sequences in the field (Morozov and Deng, 2016b). Moreover, slow Biot's P waves must be present in sub-resonant measurements of seismic attenuation in the laboratory (Morozov 2015; Morozov and Deng, 2016a, b) and they may dominate recent observations of so-called "drained-undrained" transitions in sandstone samples (Morozov, in review).

On the opposite, microscopic end of the length-scale spectrum the dominant attenuation mechanism is the so-called squirt fluid flow (Murphy at al., 1986). A schematic model of this type of pore flow is given by a penny-shaped disk connected to a donut-shaped "stiff" pore shown in Figure 2.3a (Murphy et al., 1986). The gap within a soft pore oscillates under the pressure caused by the passing wave, and the fluid is squeezed out from it and into the adjoining stiff pores. The shear deformation of the "squirting" fluid is much greater than the average deformation of the rock, and consequently a considerable dissipation of mechanical energy occurs in it. The attenuation caused by squirt flows is stronger and occurs at lower frequencies than Biot's poroelastic peak (O'Connell and Budiansky, 1977; Murphy et al., 1986; Dvorkin et al., 1994; Rubino and Holliger, 2013; Deng and Morozov, 2016).

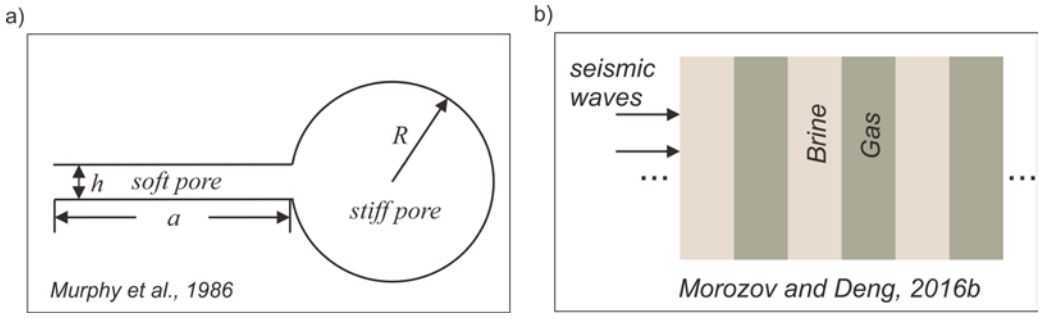

Figure 2.3. Schematic graphs of pore-flow attenuation mechanisms: a) Cross-section of a "penny-shaped" soft pore connected to a donut-shaped stiff pore; and b) mesoscopic wave-induced fluid flow (WIFF) in a layered medium, with alternating brine- and gas-saturated layers. *R* is the radius of the stiff pore, *h* is the gap width and *a* is the soft pore's radius (applied from Murphy et al., 1986).

Nevertheless, despite this suggestion of "squirting" fluid, its velocities and displacements are still much lower than typically encountered in fluid mechanics. For example, evaluating the Reynolds number $R = \rho \dot{u} a / \eta$ (where ρ is the density of the fluid, η is its viscosity, $\dot{u}$ is its relative velocity, and L is the characteristic length a in Figure 2.3a; Landau and Lifshitz, 1987) for a seismic wave with strain $\varepsilon = 10^{-6}$ in typical wet sandstone (Chapter 4), I estimate $R \approx 1$. Such small value of R shows that this fluid flow is laminar (Quintal et al., 2016), and the deformation of pore fluids is reversible and can be treated as that of a solid.

If material structure (for example, fluid saturation) is heterogeneous at the mesoscopic scale, then upon passage of a seismic wave, fluid flows between these heterogeneities would cause significantly stronger attenuation and dispersion effects than in a uniform rock (Müller et al., 2010). The peaks in the wave-energy dissipation spectra are usually stronger and occur at lower frequencies than Biot's or squirt-attenuation peaks. To observe a significant attenuation within the seismic frequency band, strong heterogeneity is required, such as patchy saturation or fracturing of the reservoir (Müller et al., 2010).

WIFF effects are often studied by scattering-theory based numerical modeling. White et al. (1975) modeled the mesoscopic WIFF effects by modeling a poroelastic rock containing spherical gas inclusions. This model was improved by Dutta and Odé (1979) and used in several recent studies (e.g., Carcione and Picotti, 2006; Müller et al. 2010). Rubino et al. (2009), Quintal et al (2012), Rubino and Holliger (2013), and Kuteynikova et al. (2014) performed 2-D and 3-D numerical modeling for the effective VE moduli and mesoscopic fluid flows in oscillatory compressibility tests. Tisato and Quintal (2013) performed laboratory experiments by using a broadband apparatus to measure attenuation at seismic

frequency band on rock sample with partial saturation. Tisato and Quintal's (2013) experimental results showed a good agreement with the above numerical model of WIFF in media with partial saturation.

Morozov and Deng (2016b) also considered an example of WIFF effects in one dimension, by modeling an infinite sequence of planar, alternating gas- and water-saturated poroelastic layers (Figure 2.3b). Unlike Rubino et al. (2009), Quintal et al (2012), Rubino and Holliger (2013), and Kuteynikova et al. (2014), Morozov and Deng (2016b) argued that for fluid-saturated media, modeling only one frequency-dependent effective modulus is insufficient, and the model should be Biot-consistent (Thomsen, 1985), i.e. it should contain two moduli, coupling between them, and potentially Darcy (Biot's) drag friction between the effective frame and the pore fluid. An approximation for such an effective model for a layered structure with WIFF was derived based on the GLS theoretical framework (Morozov and Deng, 2016b).

The parameters selected for characterizing the effective media with WIFF, such as statistical distributions of saturation or dimensions and shapes of heterogeneities can be selected in many ways. Similar to Morozov and Deng (2016b), some researchers studied the WIFF by modifying Biot's poroelastic model. For example, Lo et al. (2005) and Beresnev (2014) included two immiscible fluids and capillary effects by extending Biot's poroelastic 2×2 matrices into 3×3 matrices. Deng and Morozov (2016; Chapter 4 in this dissertation) modeled squirt-flow attenuation by adding an additional 2×2 viscosity matrix.

CHAPTER 3

MODELS OF INELASTIC MEDIA

As outlined in Chapter 2, there exist two general yet fundamentally different approaches to modeling seismic attenuation: 1) phenomenological model based on a *Q* factor that is free of physical detail, and 2) models without a *Q* attributed to the material and based on the specific physics of processes and models of rock microstructure. In this Chapter, I describe a new, physics-based phenomenological framework providing a comprehensive and rigorous view on both of these groups of approaches. In the following sections, I first introduce Lagrangian continuum mechanics, explain how the conventional *Q* model relates to it, and then discuss Biot's poroelastic model and introduce a generalized macroscopic model called the General Linear Solid (GLS) (Morozov and Deng, 2016a).

The presentation in this Chapter is based on the following published paper and a paper in preparation:

Morozov, I. B., and ***W. Deng****, 2016. Macroscopic framework for viscoelasticity, poroelasticity and wave-induced fluid flows – Part I: General Linear Solid: Geophysics, 81, no. 1, L1-L13, doi: 10.1190/GEO2014-0171.1.*

Deng, W*., and Morozov, I. B. Double-porosity models for squirt flows in sandstone, in preparation for Geophysical Prospecting*

 My contribution to the first paper consisted in participation in the development of the approach and development of the numerical algorithms and examples. The texts were modified and reformatted for incorporation in the present dissertation.

3.1 Lagrangian Continuum Mechanics with Energy Dissipation

Most of the theoretical analysis in this dissertation is based on Lagrangian mechanics. The Lagrangian formalism is one of the most powerful and productive approaches to the mechanics of continuous media, which has been used in many areas of theoretical physics (Landau and Lifshitz, 1986). Because of its origin in the Hamiltonian variational principle, this approach greatly simplifies the mathematical formulation while making it rigorous and universally applicable. Unfortunately, Lagrangian mechanics is still poorly utilized in seismology, perhaps with the exception of Biot's theory of poroelasticity (Bourbié et al., 1987).

The general steps for formulating a Lagrangian description for a mechanical system starts from selecting a set of generalized coordinates. The generalized coordinates can be arbitrary and are selected in order to completely and conveniently characterize the deformation of interest. Depending on the spatial scale of analysis, this deformation can include the microscopic or macroscopic displacements of parts of the system. In terms of these selected coordinates and their time derivatives, the kinetic energy T and potential energy V need to be defined and combined in the Lagrangian density L as

$$L \equiv T - V . \tag{3.1}$$

In this dissertation, I only discuss macroscopic-scale models, and therefore the generalized coordinates are macroscopic and represent the displacement of the reference elementary volumes (REV) taken at different points in space. The kinetic energy T is a function of the corresponding velocities, and V is a function on the displacements and/or strains. The functional form of the Lagrangian uniquely describes the conservative mechanical system (Morse and Feshbach, 1953). To describe a system with inelasticity, a dissipation function or dissipation pseudo-potential D is needed (Bourbié et al., 1987). This

pseudo-potential provides an "external" frictional force acting on the conservative system (Landau and Lifshitz, 1986). For the pseudo-potential, the principal dependence is on the velocities (i.e. time derivatives of the generalized coordinates) and consequently also on the strain rates. Fortunately, and similarly to *L*, quadratic dependences of *D* on its arguments can usually be considered. Such quadratic dependences lead to linear equations of motion, which are usually sufficient for weak deformations occurring for a seismic wave propagation.

Specifying a pair of functions *L* and *D* gives a complete description of a wide range of elastic or inelastic deformation mechanisms within rock (Morozov and Deng, 2016a; 2016b). To obtain the equations of motion, the Euler-Lagrange equation is applied to the (*L*, *D*) pair (Landau and Lifshitz, 1986):

$$\frac{\partial}{\partial t}\frac{\partial L}{\partial \dot{u}_i}+\frac{\partial}{\partial x_j}\frac{\partial L}{\partial u_{i,j}}-\frac{\partial L}{\partial u_i}+\frac{\partial D}{\partial \dot{u}_i}+\frac{\partial}{\partial x_j}\frac{\partial D}{\partial \dot{u}_{i,j}}=0\,, \tag{3.2}$$

where u_i is the generalized displacement variable, $u_{i,j}\equiv \partial u_i/\partial x_j$ denotes its spatial partial derivatives, $\dot{u}_i\equiv \partial u_i/\partial t$ is its time derivative, and $i,\ j=1,\ 2,\ 3$ denote the Cartesian coordinates. In this equation, quantities u_i , $\dot{u}_i$, $u_{i,j}$ and $\dot{u}_{i,j}$ are treated as independent arguments of functions *L* and *D*. If we omit the pseudo-potential *D* and consider *L* independent of time, then the system is conservative (conserving the total energy). The meaning of the Euler-Lagrange equation (3.2) then represents the Hamiltonian variational principle, which states that for the true time-dependent deformation of the medium, its Hamiltonian action $S=\int Ld^3xdt$ is stationary: $\delta S=0$ (Morse and Feshbach, 1953). The additional terms containing function *D* in eq. (3.2) representing a way for including external forces (friction in this case) in Lagrangian mechanics.

The significance of the different terms in eq. (3.2) varies for different mechanical

systems. For example, the term $\partial L/\partial u_i$ is absent in Biot's model described below, but it can be useful for describing squirt flows or gravitational or electric-potential energy in propagating waves. When the initial conditions and boundary conditions are appropriately specified, all parameters of the resulting oscillatory or transient deformation (seismic wave) can be rigorously solved for by using eq. (3.2).

3.2 Phenomenological Physics-Based Macroscopic Models

With appropriately selected variables and functions *L* and *D*, the two equations (3.1) and (3.2) represent a complete description of any mechanical system (Landau and Lifshitz, 1986). These equations allow us to study complex mechanical systems using a common, convenient, compact, and rigorous formulation. In the following sections, this formulation is developed for an arbitrary macroscopic, multi-phase, linear, and isotropic medium and applied to several specific cases. In the following, I call this general theoretical model the "General Linear Solid" (GLS; Morozov and Deng, 2016a, b).

The GLS models of this chapter are still phenomenological in the sense of being derived not from any specific model for the microstructure or mechanics of the medium but only from the general principles of isotropy and linearity of interactions (Landau and Lifshitz, 1986). In this sense, these models are analogous to the model of VE moduli and *Q* discussed in Chapter 2. However, there exist three fundamental differences of this phenomenology from those based on VE and *Q* concepts:

1) The Lagrangian model focuses on identifying true material properties describing the elastic, inertial, and frictional behavior of the material. These properties are not specifically geared for describing "energy dissipation" (such as *Q*) and can (in principle) be measured in other types of experiments.

2) In contrast to the *Q* model, the new model focuses on deriving the time-domain differential equations of motion first and then finding the oscillatory solutions and effective (apparent) VE moduli and *Q* factors for them.
3) In contrast to the VE model, the model uses only time- and frequency-independent material properties and explains the frequency-dependent observed (apparent) *Q*s and other effects through them.

As shown in the following sections, despite such major differences from viscoelasticity, the GLS model contains all "physically-realizable" VE models of materials (Liu et al., 1976). Because of its foundations in basic physics, this model also contains Biot's poroelasticity and allows for extending it in many ways.

3.3 The General Linear Solid model

All GLS models presented in this dissertation can be viewed as mechanical continuum models with *N* spatial variables. The first of these variables will normally be the observable displacement *u* of a macroscopic point within the material, whereas others can be the relative displacements of pore fills or some other properties based on different assumptions. For example, if a porous medium is considered, then $N = 2$, and in addition to *u*, the second variable will be the relative displacement of pore fluid. With *N* variables, the most general quadratic forms of the Lagrangian density *L* (eq. (3.1)) and the pseudo-potential *D* are (Morozov and Deng, 2016a)

$$\begin{cases} L = \frac{1}{2}\dot{\mathbf{u}}_i^T \boldsymbol{\rho} \dot{\mathbf{u}}_i - \left(\frac{1}{2}\boldsymbol{\Delta}^T \mathbf{K} \boldsymbol{\Delta} + \tilde{\boldsymbol{\varepsilon}}_{ij}^T \boldsymbol{\mu} \tilde{\boldsymbol{\varepsilon}}_{ij} \right), \\ D = \frac{1}{2}\dot{\mathbf{u}}_i^T \mathbf{d} \dot{\mathbf{u}}_i + \left(\frac{1}{2}\dot{\boldsymbol{\Delta}}^T \boldsymbol{\eta}_K \dot{\boldsymbol{\Delta}} + \dot{\tilde{\boldsymbol{\varepsilon}}}_{ij}^T \boldsymbol{\eta}_\mu \dot{\tilde{\boldsymbol{\varepsilon}}}_{ij} \right), \end{cases} \tag{3.3}$$

where u_i is the vector for displacement, $\boldsymbol{\Delta}$ is the matrix for volumetric strain and

$\tilde{\boldsymbol{\varepsilon}}_{ij} \equiv \boldsymbol{\varepsilon}_{ij} - \frac{\boldsymbol{\Delta}}{3}\delta_{ij}$ is the pure shear (deviatoric) strain. All matrix products in eq. (3.3) are evaluated in the *N*-dimensional model space, implied (Einstein) summations are used for pairs of repeated spatial indices. In eq. (3.3), $\boldsymbol{\rho}$ is the density matrix; $\mathbf{K}$ and $\boldsymbol{\mu}$ are the elastic matrices for bulk moduli and shear moduli; $\boldsymbol{\eta}_K$ and $\boldsymbol{\eta}_\mu$ are their viscosity counterparts; and *i*, *j* = 1, 2, 3 denote the spatial coordinates. Matrix $\mathbf{d}$ is the "damping" term for Darcy's friction. Matrices $\boldsymbol{\rho}$, $\mathbf{K}$, $\boldsymbol{\mu}$, $\boldsymbol{\eta}_K$, $\boldsymbol{\eta}_\mu$ and $\mathbf{d}$ should be symmetric and non-negative definite. Different configurations of these matrices determine the different types of media, such as elastic, viscoelastic, poroelastic, or their extensions (next subsections). Expressions (3.3) follow from only three very general considerations (Landau and Lifshitz, 1986): 1) dependence of the elastic energy and viscous friction on the strain tensors only; 2) isotropy of the medium (and hence the dependence of *L* and *D* on only two rotational invariants of tensors $\boldsymbol{\varepsilon}$ and $\dot{\boldsymbol{\varepsilon}}$), and 3) linearity of the resulting equations of motion, which corresponds to quadratic forms for *L* and *D*. Note that in general, viscosity terms are allowed in the dissipation function (the terms in parentheses in *D* in relations (3.3)) as naturally and uniquely as the corresponding elasticity terms in *L* (parentheses in equation (3.3); Landau and Lifshitz, 1986).

By applying the Euler-Lagrange equation (3.2), the Lagrangian and dissipation function in equations (3.3) lead to a matrix equation of motion for wave propagation,

$$\boldsymbol{\rho}\ddot{\mathbf{u}}_i = -\mathbf{d}\dot{\mathbf{u}}_i + \partial_j \boldsymbol{\sigma}_{ij}, \tag{3.4}$$

where the strain-related (elastic and viscous) stress tensor equals:

$$\boldsymbol{\sigma}_{ij} = \mathbf{K}\boldsymbol{\Delta}\delta_{ij} + 2\boldsymbol{\mu}\tilde{\boldsymbol{\varepsilon}}_{ij} + \boldsymbol{\eta}_K\dot{\boldsymbol{\Delta}}\delta_{ij} + 2\boldsymbol{\eta}_\mu\dot{\tilde{\boldsymbol{\varepsilon}}}_{ij}. \tag{3.5}$$

Assuming a uniform GLS media and consider the attenuation of a P-wave in which all spatial displacements are oriented in the direction of axis *x*, the following generalized eigenvalue problem is obtained from (3.4) and (3.5):

$$\boldsymbol{\rho}^{*}\boldsymbol{\upsilon}^{(n)} = \gamma^{(n)}\mathbf{M}^{*}\boldsymbol{\upsilon}^{(n)}\,. \tag{3.6}$$

Here, $\gamma(n) = k^{*2}/\omega^2$ is the eigenvalues for n-th mode and $\boldsymbol{\upsilon}^{(n)}$ is the corresponding wave mode. Here, k^* denotes the complex wavenumber. The complex-valued density $\boldsymbol{\rho}^*$ and complex-valued P-wave modulus $\mathbf{M}^*$ are

$$\boldsymbol{\rho}^{*} \equiv \boldsymbol{\rho} + \frac{i}{\omega}\mathbf{d}\ ,\ \mathbf{M}^{*} \equiv \mathbf{M} - i\omega\boldsymbol{\eta}\,, \tag{3.7}$$

where ω is the angular frequency of the plane wave. Such complex-valued and frequency-dependent properties are often also called "dynamic" properties. Relations (3.7) represent the rigorous (matrix) correspondence principle for poro- and visco-elasticity (Morozov and Deng, 2016a). P-wave modulus $\mathbf{M} \equiv \mathbf{K} + 4\boldsymbol{\mu}/3$ and its viscosity counterpart $\boldsymbol{\eta} \equiv \boldsymbol{\eta}_K + 4\boldsymbol{\eta}_\mu/3$. The phase velocity of n-th mode is

$$V_{\text{phase}} = \omega/k = \left(\text{Re}\left(\sqrt{\gamma}\right)\right)^{-1}\,, \tag{3.8}$$

and by the definition (2.5), the dissipation factor Q^{-1} is

$$Q^{-1} \equiv 2\alpha/k = 2\,\text{Im}\left(\sqrt{\gamma}\right)\Big/\text{Re}\left(\sqrt{\gamma}\right). \tag{3.9}$$

Thus, the GLS approach allows accurate solutions for attenuation ($Q(\omega)$) and velocity dispersion ($V_{\text{phase}}(\omega)$) relations for harmonic waves that are usually considered in the literature. However, the key contribution of this approach to modeling porous rock consists in its explicit time-domain character (eq. (3.4)). Most current theoretical models of squirt flows and numerical models of wave-induced fluid flows (WIFF) are performed in the frequency domain and often rely on frequency-dependent material properties (for example, Masson et al., 2006, Rubino et al., 2007, and Quintal et al., 2012). Although also allowing frequency-domain analysis (eqs. (3.6)), the GLS requires no time- and frequency-dependent parameters, and the time-domain equations (3.4) naturally lead to finite-difference forward

modeling (Appendix A).

3.3.1 Standard linear solid and its extensions

The broadly used Standard Linear solid (SLS), also known as Zener's model (Zhu et al., 2013), uses a linear combination of two springs and a dashpot for modeling the behavior of a VE material. These mechanical elements are representations for the elastic and viscous properties of the medium, respectively. The SLS can be viewed as a special case of the "Generalized SLS" (GSLS) model schematically described by the mechanical system in Figure 3.1a. The uppermost spring in this system (modulus M_1 in Figure 3.1a) is the "relaxed" (zero-frequency) elastic modulus operating in a quasi-static (infinitely slow) deformation (Carcione, 2014), and each spring-dashpot pair below it is the so-called Maxwell's body (MB). As shown in Figure 3.1b, for an SLS (one elastic spring and one MB), one attenuation peak near 10-Hz frequency and the corresponding transition between the "relaxed" and "unrelaxed" (infinite-frequency) levels of the modulus are predicted.

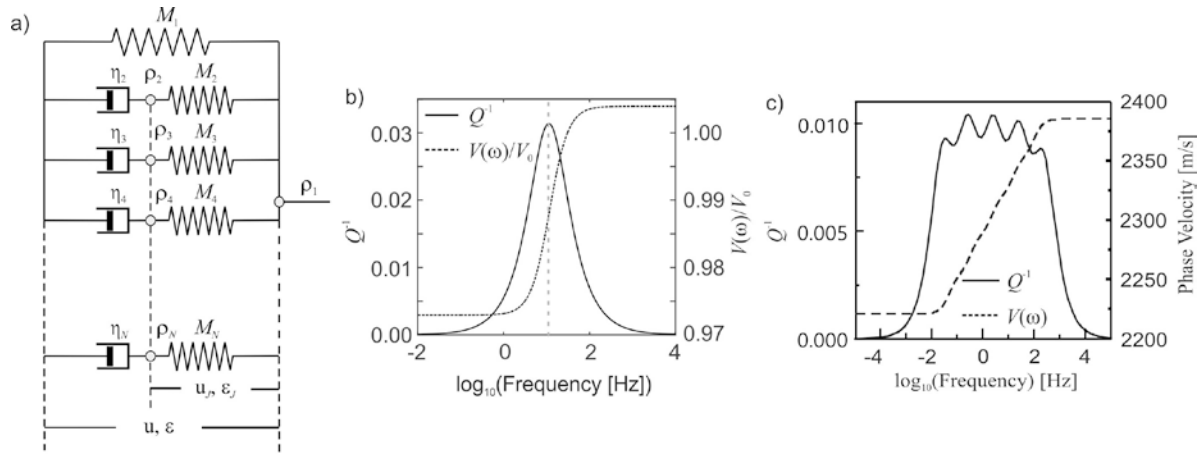

Figure 3.1. Attenuation and dispersion of a Generalized Standard Linear Solid (GSLS). With one MB ($N = 2$), this solid gives the Standard Linear Solid (SLS, or Zener's solid). a) mechanical diagrams; b) attenuation (Q^{-1}) and phase velocity (V) dispersion for SLS ($N = 2$); c) attenuation and dispersion for $N = 6$. Vertical gray dashed line in plot b) indicates the peak frequency of Q^{-1}.

In the GLS form (eqs. (3.3)), the mechanical Lagrangian and dissipation pseudo-

potential of the SLS model is obtained by setting $N = 2$ and the following 2×2 matrices:

$$\boldsymbol{\rho} = \begin{bmatrix} \rho_1 & 0 \\ 0 & 0 \end{bmatrix},\ \mathbf{M} = \begin{bmatrix} M_1 & 0 \\ 0 & M_2 \end{bmatrix},\ \boldsymbol{\eta} = \begin{bmatrix} \eta_2 & -\eta_2 \\ -\eta_2 & \eta_2 \end{bmatrix} \text{ and } \mathbf{d} = \begin{bmatrix} 0 & 0 \\ 0 & 0 \end{bmatrix}. \qquad (3.10)$$

Here, the density ρ_1 and elastic modulus M_1 correspond to the "external" variable u_1 (i.e., observable deformation of the rock usually measured in experiments), whereas parameter M_2 is the elasticity of the internal structure of the system represented by parameter u_2 (the deformation of the spring with stiffness M_2 in Figure 3.1a). The viscosity η_2 is a property of the communication between these two variables, and it cannot be simply attributed to either of them alone. Because the mechanical system reproduces the SLS exactly, the attenuation spectrum and phase-velocity dispersion predicted by this configuration of $\boldsymbol{\rho}$, $\mathbf{M}$, $\boldsymbol{\eta}$ and $\mathbf{d}$ are identical to those in Figure 3.1b.

For the general GSLS model with $N > 2$ (Figure 3.1a), the GLS parameter matrices are

$$\boldsymbol{\rho} = \begin{bmatrix} \rho_1 & 0 & 0 & \cdots & 0 \\ 0 & 0 & 0 & \cdots & 0 \\ 0 & 0 & 0 & \ddots & \vdots \\ \vdots & \vdots & \ddots & \ddots & 0 \\ 0 & 0 & \cdots & 0 & 0 \end{bmatrix},\ \mathbf{M} = \begin{bmatrix} M_1 & 0 & 0 & \cdots & 0 \\ 0 & M_2 & 0 & \cdots & 0 \\ 0 & 0 & M_3 & \ddots & \vdots \\ \vdots & \vdots & \ddots & \ddots & 0 \\ 0 & 0 & \cdots & 0 & M_N \end{bmatrix},$$

$$\boldsymbol{\eta} = \begin{bmatrix} \sum_{J=1}^{N} \eta_J & -\eta_2 & -\eta_3 & \cdots & -\eta_N \\ -\eta_2 & \eta_2 & 0 & \cdots & 0 \\ -\eta_3 & 0 & \eta_3 & \ddots & \vdots \\ \vdots & \vdots & \ddots & \ddots & 0 \\ -\eta_N & 0 & \cdots & 0 & \eta_N \end{bmatrix} \text{ and } \mathbf{d} = \mathbf{0}. \qquad (3.11)$$

Here, parameters ρ_1, M_1 again correspond to the external variable while all others correspond to the internal variables. Note that all MBs in both SLS and GSLS are massless, which is shown by the internal densities $\rho_{2,\ \ldots,\ N}$ equal zero. Substitute (3.11) into eq. (3.7), we can

solve the eigenvalue problem (3.6) for the phase velocity in (3.8) and dissipation factor Q^{-1} in (3.9). For example, with five MBs ($N = 6$) with parameters shown in Table 3.1, the eigenvalue problem in equation (3.6) yields the well-known shapes of phase velocity and Q^{-1} spectra in Figure 3.1c.

3.3.2 Internal densities

The density of the internal variable (white circles in Figure 3.1a and vector $\boldsymbol{\rho}$ in equation (3.6)) have significant influence on the phase velocity and quality factor Q. For example, in Figure 3.1c, the zero mass densities assigned to the internal variables cause four of five eigenmodes of the GSLS to have zero eigenvalues. These zero densities mean that the kinetic energy of the internal variables is identically zero, which causes them to behave as "memory variables", i.e. be expressed by integrals over the preceding history of the observed strain (Deng and Morozov, 2013). However, if we seek some physical phenomena underlying this memory process, massless variables generally appear problematic. Real physical processes always possess kinetic energy, although it may be small and negligible in certain limiting cases. It is therefore interesting to check how an introduction of small densities for the internal variables would affect the predicted dispersion and Q^{-1} spectra of a GSLS.

The GSLS model contains a relatively large number of internal variables connected in a fairly specific pattern, with many coupling parameters set equal zero. This model can be altered in many ways, and it is possible that such alterations might correspond to reality. To investigate the effects of nonzero internal density, I tried adding equal diagonal elements to the density matrix: $\rho_J = b\rho_1$, where $J = 2, \ldots, N$. Thus, the density matrix in (3.11) becomes

$$\boldsymbol{\rho} = \begin{bmatrix} \rho_1 & 0 & \cdots & 0 \\ 0 & \rho_2 & \ddots & \vdots \\ \vdots & \ddots & \ddots & 0 \\ 0 & \cdots & 0 & \rho_N \end{bmatrix}. \tag{3.12}$$

For $b > 0$, additional P-wave modes appear. Similarly to the poroelastic case, I identify the 'primary' P-wave mode with the one having the largest "observable" displacement u_1. The near-constant spectra of $Q^{-1}(\omega)$ for the primary mode are achieved by progressive "freezing", with increasing frequency, of the internal variables containing lower damping factors (Table 3.1). This freezing increases the attenuation at higher frequencies (Figures 3.2a and 3.2c).

There exists an important dividing case $b = b_0$ for which the ratios of the moduli to the densities are equal in all MBs (Figure 3.1a). In this case, the internal variables are not excited by the primary wave, and the wave is therefore nondispersive and attenuation-free. For a GSLS with parameters given in Table 3.1, this case corresponds to $b_0 = 0.015$. Note that this is a relatively small value of the order of the dissipation rate (Q^{-1}) of the original GSLS.

Table 3.1 Parameters of the Generalized Standard Linear Solid (GSLS) medium

			GSLS model (Figure 3.1c)	GSLS with 1% (5%) internal densities (Figure 3.2)
J	M_J, (GPa)	η_J (Pa·s)	ρ_J (kg/m3)	ρ_J (kg/m3)
1	10	0	2000	2000
2	0.15	$9.3 \cdot 10^8$	0	20 (100)
3	0.15	$9.3 \cdot 10^7$	0	20 (100)
4	0.15	$9.3 \cdot 10^6$	0	20 (100)
5	0.15	$9.3 \cdot 10^5$	0	20 (100)
6	0.15	$9.3 \cdot 10^4$	0	20 (100)

For values of b below and above b_0, and the effects of density are different. For $b < b_0$, $Q^{-1}(\omega)$ of the primary mode is near-constant and decreases with b, and the velocity

dispersion is positive. The secondary modes in this case are faster than the primary V_{phase}, as suggested by their greater M_J/ρ_J ratios. This case is illustrated by selecting $b = 0.01$ in Figures 3.2a and 3.2b.

For $b > b_0$, the $Q^{-1}(\omega)$ increases with b, the dispersion is negative, as shown for $b = 0.05$ in Figures 3.2c and 3.2d. In this case, the additional modes are slower than V_{phase}. Note that the increase of the phase velocity with frequency does not automatically follow from a band-limited near-constant $Q^{-1}(\omega)$, as it is often thought (Figure 3.2d). The low-frequency asymptotes of phase velocities in all models are reduced because of the net increases of their densities, and the levels of Q^{-1} for the primary mode vary by 2–3 times. However, these variations can be corrected by adjusting the values of ρ_1, M_J, and/or η_J (Table 3.1).

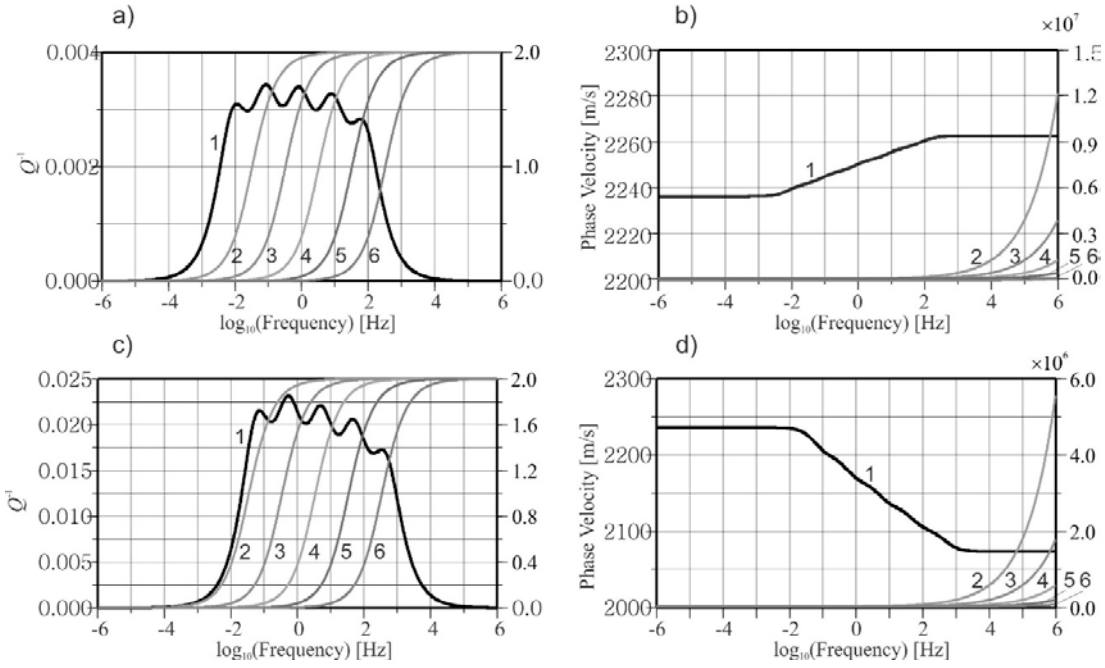

Figure 3.2. Propagation of a plane P wave in a GSLS medium with densities assigned to the internal variables: a) attenuation for internal density levels of 1% of the main density (Table 3.1), b) phase velocity for 1% internal densities, c) and d) the same for 5% internal densities (Table 3.1). The numbers of the wave modes are labeled. Black lines indicate the primary mode, and gray lines are the additional modes due to the internal densities.

With no physical argument for the internal ("memory") variables as well as for their densities, damping factors, and moduli, it is impossible to say which of the above internal-density models is correct or more realistic. In terms of achieving a near-constant Q^{-1} for the primary mode within the ~0.01–1000 Hz frequency band, all of these models are practically equivalent. Observations of secondary P-wave modes near velocity/density contrasts would certainly be a criterion of validity for such models. However, physical meanings need again to be assigned to the internal variables and the corresponding measurement procedures need to be designed in order to detect such secondary modes.

From the theoretical point of view, multiple internal variables with zero densities in the GSLS model appear extremely unrealistic. The poroelastic model (next subsection) shows that the internal variables should likely be coupled. The models of linear solids were originally designed to explain quasi-static lab experiments (Lakes, 2009), in which the density effects are insignificant and cannot be assessed. However, the quasi-static limit is inappropriate for seismic waves, in which the effect of inertia is intertwined with the elastic and frictional ones (equation 3.6). The selection of sparse matrices $\mathbf{M}$ and $\boldsymbol{\eta}$ with $\mathbf{d} = \mathbf{0}$ in GSLS equations (3.4) is done only for mathematical convenience, and similar spectra of $Q^{-1}(\omega)$ could likely be achieved with fewer variables but fuller-rank matrices. Thus, the GSLS may be oversimplified physically but over-parameterized mathematically way to model seismic attenuation. Due to the over-parameterization, this model easily fits most experimental $Q^{-1}(\omega)$ spectra; however, it remains an open question how well this model reproduces the actual processes of wave propagation.

3.3.3 Biot's poroelasticity

With two variables ($N = 2$) and zero solid viscosity ($\boldsymbol{\eta} = \mathbf{0}$), equation (3.3) represents

Biot's (1962) poroelasticity. In this case, external displacement u_1 is the observable deformation of the fluid-saturated rock, and the internal variable u_2 is the filtration displacement (relative displacement between the fluid and its unperturbed position in the host matrix) multiplied by the porosity ϕ: $\mathbf{u}_2 \equiv -\mathbf{w} \equiv -\phi(\mathbf{u}_{\text{fluid}} - \mathbf{u}_1)$. With such selection of variables, matrices **K**, **μ**, and **d**, are (Bourbié et al., 1987; Morozov and Deng, 2016a)

$$\mathbf{K} = \begin{bmatrix} K_U & -\alpha M \\ -\alpha M & M \end{bmatrix},\ \boldsymbol{\mu} = \begin{bmatrix} \mu & 0 \\ 0 & 0 \end{bmatrix},\ \boldsymbol{\rho} = \begin{bmatrix} \rho & -\rho_f \\ -\rho_f & a\rho_f/\phi \end{bmatrix}, \text{ and } \mathbf{d} = \begin{bmatrix} 0 & 0 \\ 0 & \eta/\kappa \end{bmatrix}. \quad (3.13)$$

Here, ρ_f is the density of the pore fluid, $a \geq 1$ is the tortuosity of the pore space, and ϕ is the porosity of the rock. Material properties K_U, α, M, η, and κ are first set as phenomenological constants in the L and D functions, and their physical meanings are further established by considering a set of deformational and fluid-flow experiments with this material (Bourbié et al., 1987; Morozov and Deng, 2016b). These experiments show that K_U can be measured as the undrained bulk modulus of the system with constant fluid content ($u_2 = 0$) and parameter M is the pressure that needs to be exerted on the fluid to increase the fluid content by a unit value at constant volume (when $\Delta_1 = 0$). Parameter $\alpha \in [0,1]$ is the Biot-Willis coefficient measuring the proportion of the apparent dilatational strain caused by a variation in fluid content. These parameters are related to the bulk modulus of a drained rock frame K_D by $\alpha^2 M = K_U - K_D$ (Bourbié et al., 1987). Similarly, η is the pore-fluid viscosity, and κ can be interpreted as the absolute permeability measured in a static filtration-flow experiment (Bourbié et al., 1987).

Solution of the eigenvalue equation (3.6) show that two P-waves exist in a poroelastic medium, which are the so-called fast (primary) and Biot's slow (secondary) P waves (Figure 3.3). The attenuation of the fast P-wave peaks at frequencies much higher than

seismic frequencies (Figure 3.3a).

The attenuation and velocity dispersion spectra of poroelastic rock (Figure 3.3) are generally similar to those of an SLS (Figure 3.1b), and many authors have approximated poroelastic media with a SLS medium (Geertsma and Smit, 1961). Such approximations are particularly important for developing finite-difference algorithms for modeling seismic waves. Geertsma and Smit (1961) showed that the attenuation and dispersion spectra of fast P-waves can be exactly modeled by a carefully designed SLSs (circles in Figures 3.3a and 3.3b). However, a major drawback of this approximation is that it only models one (fast) of the two poroelastic wave modes (Morozov and Deng, 2016b). The slow P-wave can be modeled separately, by using a GSLS with multiple MBs (Carcione and Gurevich, 2011). As an example, in Figure 3.3c and 3.3d, I approximate the slow P-wave $Q^{-1}(\omega)$ spectra by utilizing a GSLS with $N = 10$. The attenuation spectra for slow P waves can never be perfectly reproduced by GSLS, regardless of the number of MBs involved. This difficulty occurs because of a different lower frequency limit of $Q^{-1}(\omega)$ of poroelastic slow P-waves and GSLS model. Thus, although the approximation of the attenuation/dispersion spectra for fast and/or slow P waves in Figure 3.3c and 3.3d may be acceptable for fitting band-limited $Q^{-1}(\omega)$ data, their explanation by GSLSs are different and remote from physical reality of Biot's poroelasticity. This complexity and lack of physical correctness may result in excessive complexity (for example, numerous "memory variables") and inaccuracy of numerical forward modeling.

Since Biot's dissipation peaks occur at extremely high frequencies, poroelastic models cannot directly explain the attenuation observed in field or laboratory experiments. However, pore-fluid flows are still considered the basic mechanism of seismic attenuation in

sedimentary rock (Müller et al., 2010), and many realistic models of seismic attenuation are based on Biot's theory. Most of those models explain the observed attenuation by viewing some of the Biot's rock parameters as frequency-dependent. For example, Murphy et al. (1986) and Gurevich et al. (2010) introduced a frequency-dependent bulk modulus of the

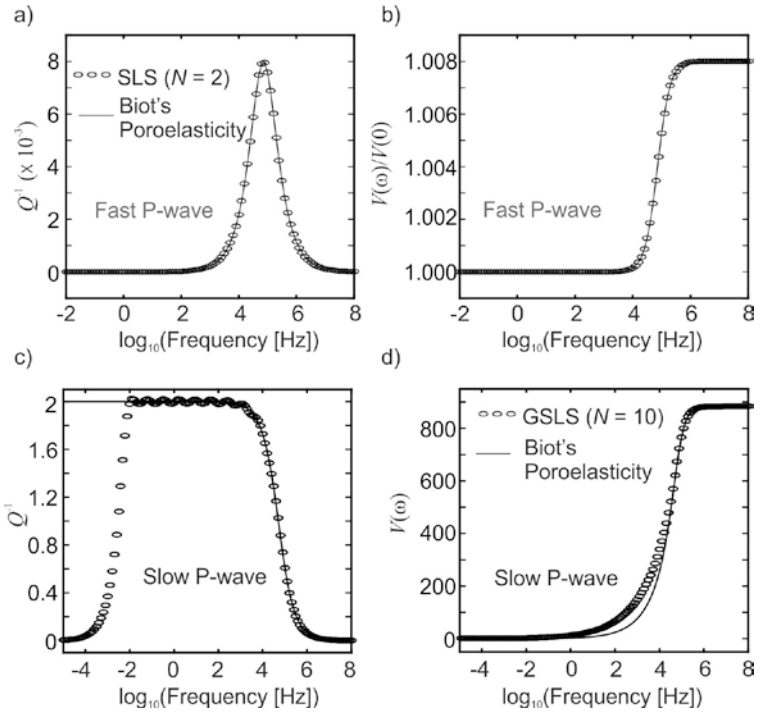

Figure 3.3. Attenuation and dispersion of Biot's poroelasticity. a) inverse-*Q* spectrum of fast P-wave and b) the corresponding phase velocity dispersion; c) inverse-Q spectrum of slow P-wave and d) the corresponding phase velocity dispersion. Solid line indicates the result obtained from solving eq. (3.6) with matrices in (3.13). The circles show the same spectra approximated by using a SLS or GSLS.

"modified effective rock frame" in order to take account of squirt flows within thin compliant cracks.

3.4 Biot-Consistent Models for Dual Porosity

Several authors considered poroelasticity with multiple filtration fluids. For example, Beresnev (2014) recently developed a quasi-static model for porous rock saturated with two non-viscous fluids with interfacial tension. This model was also based on the principles of

linearity and rotational invariants of the strain tensors, and consequently it also belongs to the class of GLS models (equations (3.3)) with $N = 3$. Let us consider the squirt-flow case for example, in which the two porosities involved are the "stiff" Biot's-type pores comprising most of the pore space and a small volume of "soft" pores containing fast and local "squirt" flows. In the following subsections, I consider two different ways for accounting for dual-porosity effects on the fast and slow P-wave modes. One of them is a straightforward extension of Biot's poroelasticity by considering dual permeability and dual tortuosity. The second, alternate approach represents the dual-porosity rock as a combination of Biot's poroelasticity and viscoelasticity. For both of these models, the generalized eigenvalue problem (3.6) can be solved to obtain the phase velocity dispersion (3.8) and Q^{-1} spectrum in eq. (3.9).

3.4.1 Poroelasticity with two fluids

One useful application of the case $N = 3$ is the model of rocks containing "soft" (compliant) and "stiff" porosities (Mavko and Jizba, 1991). These two types of porosity differ in that fluid in soft pores can be squeezed out during passage of a seismic wave. The amounts of the two porosities, ϕ_{soft} and ϕ_{stiff}, can vary with the imposed effective stress (*ibid*). In the GLS form, the difference between fluids in stiff and soft pores can be described by the moduli, density and drag matrices:

$$\mathbf{M} = \begin{bmatrix} M_{\text{P}} & \alpha_{\text{stiff}} M_{\text{stiff}} & \alpha_{\text{soft}} M_{\text{soft}} \\ \alpha_{\text{stiff}} M_{\text{stiff}} & M_{\text{stiff}} & M_{\text{cp}} \\ \alpha_{\text{soft}} M_{\text{soft}} & M_{\text{cp}} & M_{\text{soft}} \end{bmatrix}, \quad \boldsymbol{\rho} = \begin{bmatrix} \rho & \rho_f & \rho_f \\ \rho_f & \dfrac{a_{\text{stiff}}}{\phi_{\text{stiff}}} \rho_f & \rho_{\text{cp}} \\ \rho_f & \rho_{\text{cp}} & \dfrac{a_{\text{soft}}}{\phi_{\text{soft}}} \rho_f \end{bmatrix}, \text{ and}$$

$$\mathbf{d} = \begin{bmatrix} 0 & 0 & 0 \\ 0 & \eta/\kappa_{\text{stiff}} & 0 \\ 0 & 0 & \eta/\kappa_{\text{soft}} \end{bmatrix}, \tag{3.14}$$

where the volume fraction of fluid occupying the stiff porosity is assigned model variable u_2, and u_3 describes the volume of fluid in soft pores. ρ_{cp} is the possible inertial coupling effects of fluids in stiff and soft pores. M_{cp} is the possible moduli coupling effects. Here, αs and Ms have the same meaning as in (3.13) but for different fluids/pores. The low mobility of fluids in stiff pores suggests that $\eta/\kappa_{\text{stiff}} \gg \eta/\kappa_{\text{soft}}$ and possibly $a_{\text{stiff}}/\phi_{\text{stiff}} \gg a_{\text{soft}}/\phi_{\text{soft}}$. Large values of $\mathbf{d}_{22}$ and $\boldsymbol{\rho}_{22}$ should then "freeze" the fluid within stiff pores from moving at high (ultrasonic) frequencies, creating the apparent "unrelaxed" effective modulus and faster wave velocities discussed by Mavko and Jizba (1991). Eq. (3.14) can also be regarded as two different fluids in the pores.

Although the size of the moduli matrix should also be 3×3, the details of this matrix are generally unknown beyond some possible constraints from Beresnev's (2014) study and the symmetric and positive-definite character of the Lagrangian density. Instead of trying to develop the moduli matrix theoretically from some specific micromechanical model of a porous solid, I take the following simplified approach. By taking Biot's poroelasticity with squirt effects as an example (Carcione and Gurevich's, 2011), I investigate it numerically by fitting the P-waves attenuation and dispersion curves. Under the requirements of symmetry and positive-definite characters, I test three different configurations of the density ($\boldsymbol{\rho}$) and moduli ($\mathbf{M}$) matrices for different understanding of the pores and fluids. Among the elements of the constitutive matrices, the measurable quantities M_{p}, ρ, ρ_f are considered known and fixed in the tests, which here are given by 38.193 GPa, 2328 kg/m^3 and 1040 kg/m^3 respectively. The remaining parameters need to be derived by either physical analysis or by

fitting some specific quantities, such as Q^{-1} spectrum. In this section, I only consider deriving such parameters by fitting the Q^{-1} spectrum by using nonlinear least-squares method (Nocedal and Wright, 2000).

In the first approximation, assume that the fluids are only coupled to the rock. Therefore, the inertial and rigidity coupling effects can be neglected, so that $\rho_{cp} = M_{cp} = 0$ in (3.14). With this configuration, eq. (3.14) is substituted into (3.6) to solve eqs. (3.8) and (3.9) by fitting Carcione and Gurevich's (2011) Q^{-1} spectrum (black line, Figure 3.4) by utilizing the nonlinear least-squares method. The optimized $\boldsymbol{\rho}$, $\mathbf{d}$ and $\mathbf{M}$ are obtained as:

$$\boldsymbol{\rho} = \begin{bmatrix} 2328 & 1040 & 1040 \\ 1040 & 11959 & 0 \\ 1040 & 0 & 2080 \end{bmatrix} \frac{\text{kg}}{\text{m}^3},\ \mathbf{d} = \begin{bmatrix} 0 & 0 & 0 \\ 0 & 4.11 & 0 \\ 0 & 0 & 0.0103 \end{bmatrix} \frac{\text{GPa}\cdot\text{s}}{\text{m}^2}, \text{ and}$$

$$\mathbf{M} = \begin{bmatrix} 38.193 & 32.392 & 21.165 \\ 32.392 & 47.635 & 0 \\ 21.165 & 0 & 29.396 \end{bmatrix} \text{GPa}\,. \tag{3.15}$$

The values of the elements of matrices $\boldsymbol{\rho}$ and $\mathbf{d}$ related to pore fluids show that the above conditions $\eta/\kappa_{\text{stiff}} \gg \eta/\kappa_{\text{soft}}$ and $a_{\text{stiff}}/\phi_{\text{stiff}} \gg a_{\text{soft}}/\phi_{\text{soft}}$ are satisfied in this case. The obtained model (3.15) gives one fast P-wave and two slow P-waves (Figure 3.4). The fast P-wave attenuation and dispersion match the results by Carcione and Gurevich (2011) well (Figure 3.4a and 3.4b). Although the Q^{-1} spectra for the two slow P-waves the associated phase-velocity dispersion do not match Carcione and Gurevich's (2011) results, they are very diffusive and show zero phase velocity at the limit of zero frequencies (Figures 3.4c and d). In addition to Biot's slow P-wave, the GLS model predicts another slow P-wave corresponding to fluid flows within soft pores. This squirt-flow related slow P-wave's attenuation is weaker than for Biot's slow P-wave, but the corresponding velocity dispersion

is extremely high. Two reasonable explanations for such peculiar behavior of the squirt-flow related slow P-wave might be: 1) the fluid in soft pores is considered not coupled with the fluid within stiff pores (which are responsible for Biot's slow wave), and therefore their movements are independent; 2) the fluid within soft pores is less affected by the inertial force and drag forces, and consequently it moves more freely.

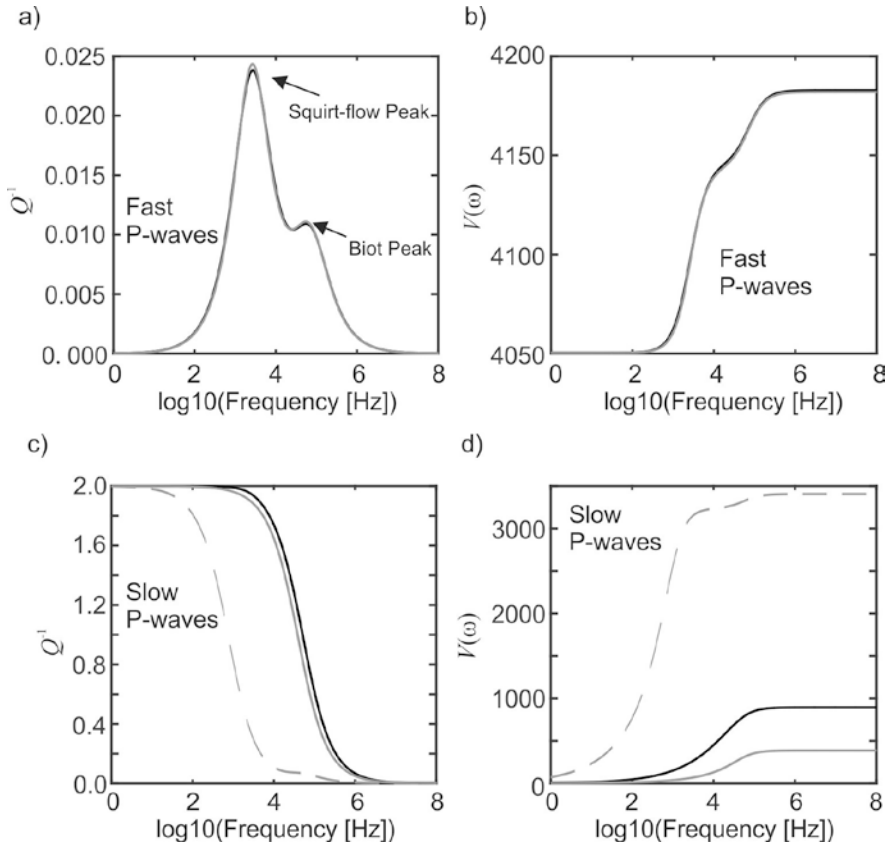

Figure 3.4. GLS model for Biot's poroelasticity with squirt flows under the assumption that fluids/pores are not coupled. a) fast P-wave attenuation and b) the associated velocity dispersion; c) slow P-wave attenuation and d) the associated velocity dispersion. Solid black lines are the attenuation and dispersion curves by Carcione and Gurevich (2011). Solid gray lines show the fast and slow P-waves from my GLS model. Dashed gray lines in plots c) and d) are the squirt-flow related slow P-wave from the GLS model.

In the second end-member model, the fluids in soft stiff pores are coupled by means of elastic moduli only. Therefore, only inertial coupling is neglected, so that $\rho_{cp} = 0$ and $M_{cp} \neq 0$. With this configuration, the details of $\boldsymbol{\rho}$, $\mathbf{d}$ and $\mathbf{M}$ are obtained as:

$$\boldsymbol{\rho} = \begin{bmatrix} 2328 & 1040 & 1040 \\ 1040 & 11959 & 0 \\ 1040 & 0 & 10867 \end{bmatrix} \frac{\text{kg}}{\text{m}^3}, \ \mathbf{d} = \begin{bmatrix} 0 & 0 & 0 \\ 0 & 4.684 & 0 \\ 0 & 0 & 0.167 \end{bmatrix} \frac{\text{GPa} \cdot \text{s}}{\text{m}^2},$$

$$\mathbf{M} = \begin{bmatrix} 38.193 & 26.804 & 34.174 \\ 26.804 & 39.418 & 28.977 \\ 34.174 & 28.977 & 40.246 \end{bmatrix} \text{GPa} . \tag{3.16}$$

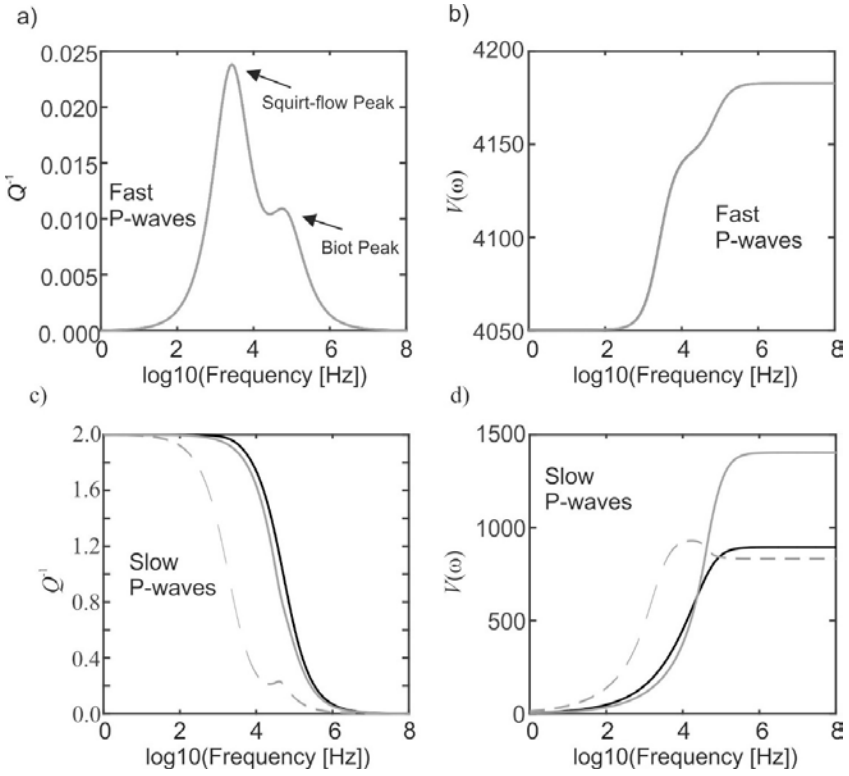

Figure 3.5. GLS model for Biot's poroelasticity with squirt flows under the assumption that fluids/pores are coupled in terms of moduli only. a) fast P-wave attenuation and b) the associated velocity dispersion; c) slow P-wave attenuation and d) the associated velocity dispersion. The indications of different lines are the same as in Figure 3.4

In this case, the expected relation $a_{\text{stiff}}/\phi_{\text{stiff}} \gg a_{\text{soft}}/\phi_{\text{soft}}$ (i.e., $\rho_{22} \gg \rho_{33}$) is not satisfied. However, model (3.16) perfectly predicts both the $Q^{-1}(\omega)$ and dispersion spectra for the fast P-wave by Carcione and Gurevich (2011) (Figures 3.5a and b). Similarly to the preceding case, two types of slow P-waves are produced by this GLS model. The attenuation spectra of Biot's flow produced by Carcione and Gurevich (2011) and by GLS model are close, but the

associated velocity dispersions are different (Figure 3.5c and d). The differences of the attenuation and dispersion characters of these two slow P-waves are because of the different elastic coupling effects.

In the third test, I assume that the fluids within the soft and stiff pores are coupled in terms of both densities and moduli, which means $\rho_{cp} \neq 0$ and $M_{cp} \neq 0$. The resulting matrices obtained by nonlinear least-squares fitting of Carcione and Gurevich's solutions (2011) are

$$\boldsymbol{\rho} = \begin{bmatrix} 2328 & 1040 & 1040 \\ 1040 & 11959 & 9605 \\ 1040 & 9605 & 24975 \end{bmatrix} \frac{\text{kg}}{\text{m}^3}, \ \mathbf{d} = \begin{bmatrix} 0 & 0 & 0 \\ 0 & 3.143 & 0 \\ 0 & 0 & 0.412 \end{bmatrix} \frac{\text{GPa} \cdot \text{s}}{\text{m}^2},$$

$$\mathbf{M} = \begin{bmatrix} 38.193 & 36.481 & 43.169 \\ 36.481 & 53.649 & 43.725 \\ 43.169 & 43.725 & 60.729 \end{bmatrix} \text{GPa}. \tag{3.17}$$

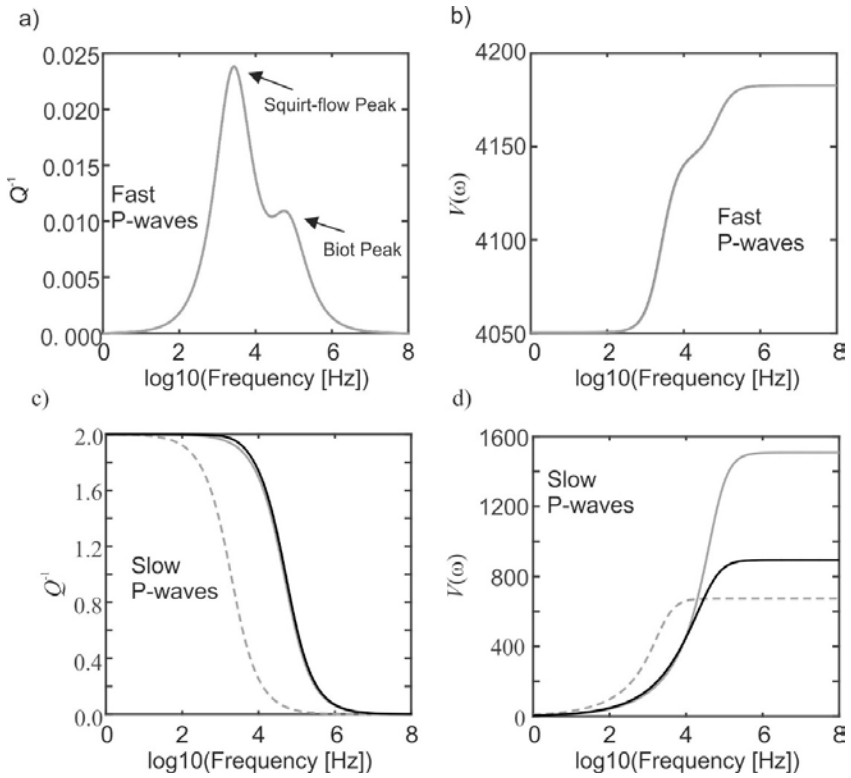

Figure 3.6. GLS model for Biot's poroelasticity with squirt flows under the assumption that fluids in soft pores and stiff pores are coupled in terms of both density and moduli. a) fast P-wave attenuation and b) the associated velocity dispersion; c) slow P-wave attenuation and d) the associated velocity dispersion. The indications of different lines are the same as in Figure 3.4

As in the preceding case, $a_{\text{stiff}}/\phi_{\text{stiff}} < a_{\text{soft}}/\phi_{\text{soft}}$ here. Model (3.17) also predicts the attenuation and dispersion of the fast P-wave by Carcione and Gurevich (2011) perfectly (Figure 3.6a and b). The properties of the Biot's slow P-wave reproduced by the GLS model still differ from those by Carcione and Gurevich (2011), and they also differ from those given by two GLS models discussed above (Figure 3.6c and d). These differences indicate that the elastic and inertial-coupling effects are important in the GLS as well as in Biot's model. This observation suggests that using a fixed and over-simplified elastic-coupling model as in a GSLS (section 3.3.1) should be insufficient for modeling porous fluid-saturated rock.

Representing elastic, inelastic, and poroelastic media in the common language of the GLS allows a better understanding of Biot's-type inelasticity and time-domain numerical modeling of various types of WIFF at different scales. To my knowledge, additional slow P-waves associated with squirt flows have still not been reported by researches, maybe with an exception of a brief suggestion by Morozov and Deng (2016a and 2016b). Although they are unlikely to be observed by direct-wave measurements in field or ultrasonic laboratory records, both Biot's and squirt-flow slow P waves could affect P-wave reflectivity in finely-layered media (which is a common case in the field) and subresonant attenuation measurements in small samples in the laboratory (Morozov, 2015 and in review). Therefore, the squirt-flow related slow wave and more general GLS models of wave-propagating media deserve more attention. For example, the slow P-wave observed by Bouzidi and Schmitt (2009) by using a large ultrasonic transmitter might actually not be Biot's slow P-wave but a squirt-flow related slow P-wave. However, more experimental and theoretical studies are needed in order to verify this conjecture.

3.4.2 Poro-viscoelasticty

In this section, I explore a simple way for combining poroelastic and viscoelastic (VE) properties of a material. Several extensions of Biot's poroelasticity to poro-viscoelastic cases have been proposed. Most of these extensions focus on some models of the microstructure. Thus, Coussy (2004) developed models of poro-plasticity and -elasticity by using the notions of plastic strains and stresses in a porous medium. By considering squirt flows in narrow compliant pores, Dvorkin et al. (1993) propose an extended Biot/squirt (BISQ) model, and Gurevich et al. (2010) show that the effects of squirt flows can be described by a complex-valued bulk modulus of the frame. Chotiros and Isakson (2004) extended the BISQ model by adding linear equations relating the pressure on the compliant-pore gap and shear drag forces within it, which also led to complex-valued effective VE moduli. A related approach consists of using Cole-Cole laws for frequency dependences of the moduli combined with Gassmann's fluid-substitution equations (Mavko, 2013). In terms of the GLS model (eqs. (3.3)), all of the above models with complex moduli correspond to nonzero viscosities.

Without considering a microstructure or Gassmann's equation, Carcione (1998) developed phenomenological macroscopic equations of motion by constructing N memory variables to represent the rock frame by a GSLS (Figure 3.1b, with $\rho_J = 0$ for $J = 2, \ldots, N$) and included an additional memory variable for the Darcy-type pore-fluid friction. For Biot's poroelasticity with fluid flow within compliant pores, Carcione and Gurevich (2011) used GSLS with $N = 3$ to model the fast P-wave but with $N = 6$ to model the slow P-wave. Note that these models therefore do not describe the material itself but are instead attuned to certain desired types of wave solutions. Also, as argued above, such sparsity and massless variables may represent serious physical drawbacks.

Here, I propose a GLS-type poro-viscoelastic model for a dual-porosity material. Following eq. (3.1), I select the material-property matrices for 1-D (P-wave) deformation as

$$\mathbf{M}=\begin{bmatrix} M_P & \alpha_{\text{stiff}}M_{\text{stiff}} & 0 \\ \alpha_{\text{stiff}}M_{\text{stiff}} & M_{\text{stiff}} & 0 \\ 0 & 0 & M_1 \end{bmatrix},\quad \boldsymbol{\rho}=\begin{bmatrix} \rho & \rho_f & 0 \\ \rho_f & \dfrac{a_{\text{stiff}}}{\phi_{\text{stiff}}}\rho_f & 0 \\ 0 & 0 & 0 \end{bmatrix},\quad \text{and}$$

$$\mathbf{d}=\begin{bmatrix} 0 & 0 & 0 \\ 0 & \eta/\kappa_{\text{stiff}} & 0 \\ 0 & 0 & 0 \end{bmatrix} \text{ and } \boldsymbol{\eta}=\begin{bmatrix} \eta_1 & 0 & -\eta_1 \\ 0 & 0 & 0 \\ -\eta_1 & 0 & \eta_1 \end{bmatrix}. \tag{3.18}$$

As shown in Figure 3.1a, M_1 and η_1 are the modulus and solid viscosity for the MB, which are responsible for squirt-flow attenuation in eq. (3.18). The remaining term $\eta/\kappa_{\text{stiff}}$ in $\mathbf{d}$ is responsible for the Biot's poroelasticity. By fitting Carcione and Gurevich's (2011) Q^{-1} spectrum as in previous numerical examples, the elements in (3.18) are found to be:

$$\boldsymbol{\rho}=\begin{bmatrix} 2328 & -1040 & 0 \\ -1040 & 11959 & 0 \\ 0 & 0 & 0 \end{bmatrix}\frac{\text{kg}}{\text{m}^3},\ \mathbf{d}=\begin{bmatrix} 0 & 0 & 0 \\ 0 & 4.68 & 0 \\ 0 & 0 & 0 \end{bmatrix}\frac{\text{GPa}\cdot\text{s}}{\text{m}^2},$$

$$\mathbf{M}=\begin{bmatrix} 38.193 & -29.240 & 0 \\ -29.240 & 43.001 & 0 \\ 0 & 0 & 1.804 \end{bmatrix}\text{GPa},$$

$$\text{and}\quad \boldsymbol{\eta}=10^5\times\begin{bmatrix} 1.063 & 0 & -1.063 \\ 0 & 0 & 0 \\ -1.063 & 0 & 1.063 \end{bmatrix}\text{Pa}\cdot\text{s}. \tag{3.19}$$

With these model parameters, the results for fast and slow P-wave attenuation and dispersion are shown in Figure 3.7. The fast P-wave attenuation and dispersion match very well the models by Carcione and Gurevich (2011) (Figures 3.7a and b). The $Q^{-1}(\omega)$ for the slow P-wave also matches the model by Carcione and Gurevich (2011) well (Figure 3.7). Interestingly, the velocity dispersion curves for slow P-wave in these two models do not

match. The high-frequency plateau of the slow P-wave dispersion produced by the GLS model is significantly higher than from Carcione and Gurevich's (2011) model.

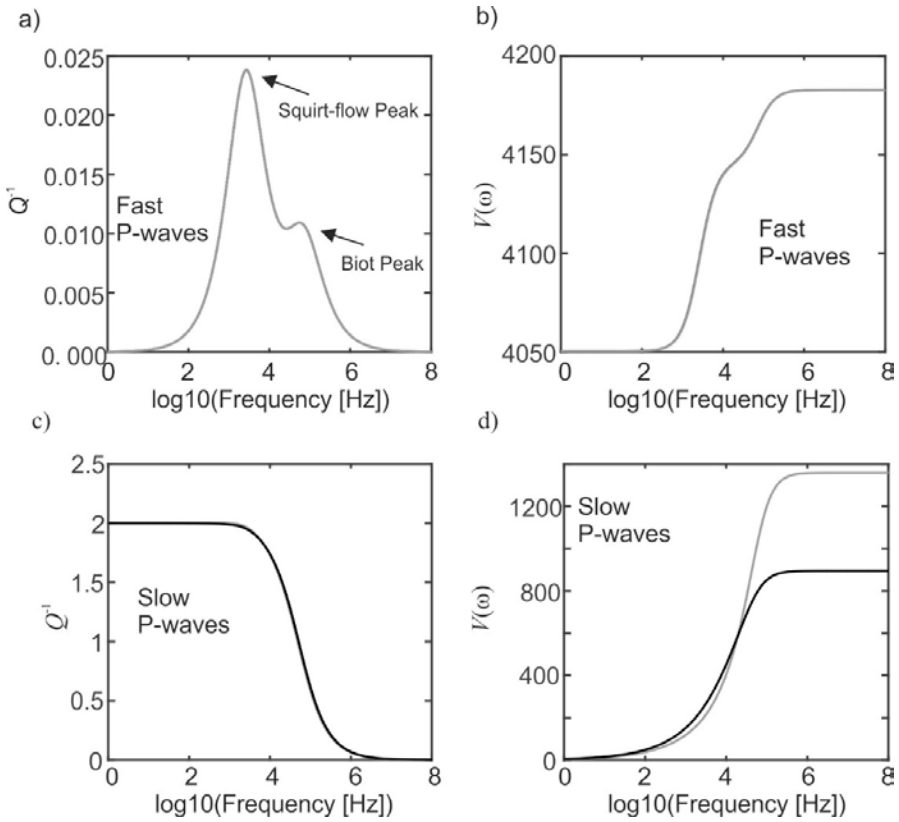

Figure 3.7. GLS visco-poroelastic model for Biot's poroelasticity with additional squirt flows. a) fast P-wave attenuation and b) the associated velocity dispersion; c) slow P-wave attenuation and d) the associated velocity dispersion. Solid black line indicates the attenuation/dispersion is given by Carcione and Gurevich (2011); solid gray lines illustrate the GLS predictions for fast and slow P waves.

The difference between the velocity dispersion curves predicted by the GLS model and the model by Carcione and Gurevich (2011) is significant for deciding which of these two models is more viable. For band-limited $Q^{-1}(\omega)$ such as shown in Figure 3.7a, the velocity dispersion function $V(\omega)$ can be derived from $Q^{-1}(\omega)$ by using the causality (Kramers-Krönig) relations (Aki and Richards, 2002). Therefore, the difference between the inferred $V(\omega)$ with identical $Q^{-1}(\omega)$ dependences shows that one of these models likely violates causality. The Lagrangian model is based on instantaneous interactions and defined

in the time domain, and consequently it is guaranteed to be causal (Landau and Lifshitz, 1986). By contrast, the model by Carcione and Gurevich's (2011) was constructed in the frequency-domain by an intricate frequency-dependent combination of five or seven SLSs. The causality of this construction is difficult to identify, and the comparison in Figures 3.7c and d suggests that it may be violated for slow P-waves. In addition, compared to the Carcione and Gurevich's (2011) model employing seven mathematical memory variables, I extend Biot's poroelasticity by using only one additional internal variable, which also has a clearer interpretation of fluid flow within "soft" pores. Thus, although the models given in eqs. (3.15) through (3.19) represent only selected end-member examples, they show that the GLS formulation provides a solid and comprehensive approach to studying the properties of realistic multi-phase media.

CHAPTER 4

SQUIRT-FLOW VISCOSITY AT SEISMIC FREQUENCIES

At the end of Chapter 3, I discussed several possible extensions of Biot's (1962) poroelastic model allowing incorporation of squirt-flow effects occurring within additional compliant pores within the rock. Here, I continue this subject by showing that most currently accepted squirt-flow models can be viewed as poro-viscoelastic GLS models (Chapter 3). The presentation is based on the following paper:

> ***Deng, W.**, and I. B. Morozov. 2016, Solid viscosity of fluid-saturated porous rock with squirt flows at seismic frequencies. Geophysics, 81, no. 4, D394-D404. doi: 10.1190/geo2015-0406.1*

4.1 Abstract

In this Chapter, I develop a macroscopic model for a two-phase medium (solid porous rock frame + saturating pore fluid) with squirt flows based on the GLS framework (Chapter 3). The model focuses on improved physics of rock deformation, including explicit differential equations in the time domain, causality, linearity, frequency-independent parameters with clear physical meanings, and absence of mathematical internal or memory variables. The approach shows that all existing squirt-flow models can be viewed as macroscopic models of viscosity for solid rock. As in existing models, the pore space is differentiated into compliant and relatively stiff pores. At lower frequencies, the effects of fluid flows within compliant pores are described by bulk and shear solid viscosities of the

effective porous frame. Squirt-flow effects are “Biot-consistent,” which means that there exists a viscous coupling between the rock frame and the fluid in stiff pores. Biot’s poroelastic effects associated with stiff porosity and global flows are also fully included in the model. Comparisons to several squirt-flow models show good agreement in predicting wave attenuation up to 1-kHz frequencies. The squirt-flow viscosity for sandstone is estimated in the range of 10^6–10^8 cP, which is close to field observations. Because of its origins in rigorous mechanics, the model can be used to describe any wave-like and transient deformations of heterogeneous porous media or finite bodies encountered in many field and laboratory experiments. The model also leads to new numerical algorithms for wavefield modeling (Appendix A), which are illustrated by 1-D finite-difference waveform modeling.

4.2 Introduction

Squirt flows within porous rock represent an important mechanism of seismic attenuation. Squirt-flow models (Figure 4.1) usually consider a rock containing two different types of pores: relatively compliant and planar “soft” pores or cracks and “stiff” pores (Murphy et al., 1986; Dvorkin et al., 1995; Pride et al., 2004; Gurevich et al., 2010). The volume fraction of soft pores, denoted by ϕ_c below, is usually much smaller than that of the stiff pores, ϕ. Upon compression and extension occurring during the passage of a seismic wave, the soft pores squeeze and expand, thereby moving the fluid or gas at relatively fast rates within their planes (Dvorkin and Nur, 1993; Figure 4.1). This fast deformation of viscous fluid or gas absorbs the mechanical energy and eventually attenuates the seismic wave. For a given viscosity of the pore fluid, this attenuation is stronger and occurs at lower frequencies than Biot’s attenuation in stiff pores (see, for example, Figure 2 in Carcione and Gurevich, 2011). The dependence of the peak-attenuation frequency on viscosity is also

opposite to that in Biot's poroelasticity (e.g., Rubino et al., 2009).

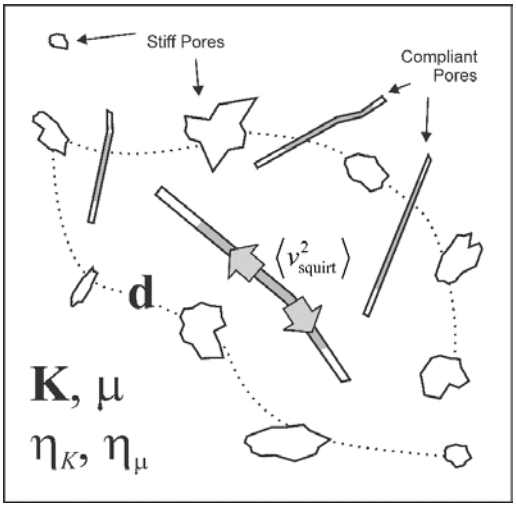

Figure 4.1. Schematic diagram of the Lagrangian model for squirt-flow model described by equation (3.3) as well as in existing models. The porosity is assumed to consist of stiff and compliant pores. The compliant pores are predominantly 2-D but do not have to be of any simple shapes or equal dimensions. Matrices **K** and **μ** describe the macroscopic bulk and shear elastic responses of the matrix with fluid-saturated stiff pores, and matrices $\boldsymbol{\eta}_K$ and $\boldsymbol{\eta}_\mu$ are the respective solid viscosities. These viscosities are due to the average squared velocities $\langle v^2_{squirt} \rangle$ of the fluid induced by the deformation within compliant pores. Matrix d describes the communication between stiff pores (dotted lines). Note that the squirt flows should affect both elastic and viscous coupling between the fluid in stiff pores and solid frame.

Most existing squirt-flow models describe the effect of soft pores by frequency-dependent effective VE moduli of the rock frame and use the (sometimes modified) Gassmann's equation to account for stiff pores. By solving for the radial flow rate caused by oscillating pressure within a narrow gap, Murphy (1986) and Gurevich et al. (2010) defined the effective time-delayed gap stiffness, from which they determined the effective moduli of the rock frame with squirt. Dvorkin et al. (1995) similarly constructed a frequency-dependent modified-frame bulk modulus to account for squirt flows. O'Connell and Budiansky (1977) derived VE moduli of a fluid-saturated solid by using a self-consistent model including interconnections between soft pores or cracks. Carcione and Gurevich (2011) used Zener's mechanical model to transform the theory by Gurevich et al. (2010) into the time domain.

Pride et al. (2004) used a squirt-transport equation to explain the squirt-flow effects. Each of these models possesses certain advantages based on somewhat different models of the compliant-pore microstructure (Figure 4.1).

Although very effective in modeling the observed attenuation and wave-velocity spectra, frequency-dependent constitutive properties such as effective moduli are quite elaborate, difficult to understand physically and require artificial mechanisms for implementing in the time domain. Such properties imply time-dependent interactions such as strain-stress "memory" within the material. However, "memory" is only a postulated mathematical concept (Volterra time integral) which always requires explanations by some specific microstructures or mechanical laws. Implementing a material memory requires postulating certain true or artificial internal structures of the material. For example, Carcione and Gurevich (2011) recast the model by Gurevich et al. (2010) in the time domain by constructing Zener's solids for each of the five elastic parameters in Biot's poroelastic model (denoted K, K_G, μ_G, M, and αM in that paper). Each of these Zener solids contains a specification of the relaxed level and two relaxation-time constants. When included in Biot-Gassmann's equations, the Zener solids reproduce the attenuation peak and velocity dispersion of a seismic wave (Gurevich et al., 2010). However, although matching the phase-velocity and Q spectra by construction, it is difficult to say how close these Zener solids are to the actual mechanism of deformation of a rock with double (soft and stiff) porosity. In reality, the squirt-flow friction is only caused by Biot's elastic coupling and fluid viscosity within compliant pores, and all fifteen parameters of Zener solids represent elaborate combinations of these physical properties (Carcione and Gurevich, 2011). Furthermore, in this and similar models, it is assumed that the five effective Biot's moduli with memory can

be used in Gassmann's equations at nonzero frequencies. This assumption also needs to be verified from first-principle physics.

To reveal the meanings of effective-moduli models and reduce their assumptions and intricacies, it would be useful to find a theoretical approach based on rigorous physics, such as classical continuum mechanics (Landau and Lifshitz, 1986). The key principles of a mechanical approach are the differential equations in the time domain and material properties independent of any specific deformation processes. Mechanical approaches explain the observed dispersion and attenuation effects by frequency- and time-independent material properties. Biot's (1956) poroelasticity is an example of such an approach to porous rock. The double-porosity model by Pride et al. (2004) also starts from differential equations in the time domain without "memory" and introduces squirt effects through additional kinetic equations. Another requirement for a rigorous mechanical model is Biot-consistency (Thomsen, 1985), meaning that squirt flows should generally affect not only the effective rock frame but also its interaction with stiff pores.

To describe the internal friction within a material, it is insufficient to only give the energy dissipation rate (or Q^{-1}, which is commonly assumed), but one must also specify the precise dependence of frictional forces on deformation. In this Chapter, I propose a simple model for such squirt-flow forces based on the concept of solid viscosity. Similar to the viscosity of fluids, solid viscosity means that frictional stresses are proportional to strain rates and governed by the Navier-Stokes equations (Landau and Lifshitz, 1986). The model is purely macroscopic and describes the same double-porosity microstructure in Figure 4.1, but with strongly relaxed requirements on the shapes of compliant pores. The macroscopic solid viscosity is caused by flows within compliant pores and therefore called "squirt-flow

viscosity" further in this Chapter.

To focus on the key approach only, I derive the parameters of the proposed model without considering any detailed microstructure but by utilizing the low-frequency limit of the well-known model by Gurevich et al. (2010). This limit appears to be adequate for describing the attenuation of porous rock with squirt at seismic frequencies of up to 1 kHz. The frequency-independent rigidities and viscosities of the material have straightforward interpretations as basic properties of fluid-saturated rock. Most importantly, these properties are (at least in principle) independently measurable in physical experiments other than involving wave propagation. Instead of phenomenological relaxation times, the squirt-flow related internal friction is characterized by solid viscosities, which are completely analogous to the viscosities of fluids. As shown in section 4.3, the advantage of this point of view is in producing time-domain differential equations of motion fully consistent with Biot's and Gassmann's models and Landau and Lifshitz's (1986) mechanics, and absence of *ad hoc* frequency-dependent parameters and material memory. In section 4.4, predictions of this model are compared to several squirt-flow models in the literature. Finally, in section 4.5 and Appendix A, I show how the Lagrangian approach allows solving many physical problems in different application areas. In two examples, I illustrate a 1-D time-domain finite-difference forward modeling and discuss a quasi-static creep experiment with fluid-saturated porous rock.

4.3 Method

Morozov and Deng (2016a and 2016b) formulated a theoretical framework of the Generalized Linear Solid (GLS) based on Lagrangian continuum mechanics (Landau and Lifshitz, 1986) and extending Biot's (1956) poroelasticity to multi-phase solids. In this

section, I summarize this approach for a two-phase medium (poroelasticity) and point out that two-component (matrix) solid viscosity is essentially the only way for describing the frictional effects omitted in Biot's theory (Sahay, 2008). Once allowing a solid viscosity in principle, the only remaining question is to determine its values resulting from squirt flows. This determination is made by analyzing the low-frequency limit of the model by Gurevich et al. (2010).

4.3.1 Lagrangian Description of a Multi-Phase Solid with Internal Friction

To formulate the squirt-flow model, I consider a fluid-saturated rock shown in Figure 4.1, which can be formulated by (3.3) with nonzero viscosity matrices $\boldsymbol{\eta}_\lambda$ and $\boldsymbol{\eta}_\mu$. These viscosity matrices equal zero in Biot's (1956) poroelasticity, but this is not required and can be viewed as an omission of this model (Sahay, 2008). In the following, I utilize these matrices to describe the effects of squirt flows within soft pores.

When considering a harmonic oscillation of angular frequency ω, the standard derivation (Landau and Lifshitz, 1986) leads from equations (3.3) and (3.13) to the equations of motion, in which the moduli and viscosity matrices can be combined in complex-valued, matrix moduli $\mathbf{K}^* \equiv \mathbf{K} - i\omega\boldsymbol{\eta}_K$ and $\boldsymbol{\mu}^* \equiv \boldsymbol{\mu} - i\omega\boldsymbol{\eta}_\mu$. For example, the matrix wave equation for P waves is (Morozov and Deng, 2016a):

$$\boldsymbol{\rho}\ddot{\mathbf{u}} = -\mathbf{d}\dot{\mathbf{u}} + \left(\mathbf{K}^* + \frac{4}{3}\boldsymbol{\mu}^*\right)\mathbf{u}'', \tag{4.1}$$

where $\mathbf{u}$ here is the displacement vector for P wave, and $\mathbf{u}''$ is its second spatial derivative in the direction of wave propagation. The phase velocities and Q factors for the fast and slow waves are then obtained by solving these equations for multiple eigenmodes (Morozov and Deng, 2016a). The scalar, effective frequency-dependent moduli M_P and M_S arise only after

the velocities V_P and V_S of the P- and S-wave eigenmodes obtained, and are defined as $M_{P,S} \equiv \rho V_{P,S}^2$. Thus, frequency-dependent moduli are properties of wave modes and not of the material (Morozov, 2015). Such properties are absent in the Lagrangian model.

4.3.2 Solid Viscosity due to Squirt Flows

The GLS squirt-flow model describes the same microstructure as models by Murphy et al. (1986), Dvorkin et al. (1995), and Gurevich et al. (2010) (Figure 4.1). However, this microstructure is not limited to planar and circular shapes, equal sizes of compliant pores or specific boundary conditions on their circumferences. To include compliant fluid-filled pores in relations (3.3), one would generally need to add a third variable to the model vector u and expand all matrices into three dimensions. As it will be shown in a later publication, a rigorous macroscopic description of the squirt-flow mechanism requires terms containing products $\mathbf{u\varepsilon}$ and $\dot{\mathbf{u}}\dot{\boldsymbol{\varepsilon}}$ in functions (3.3). However, here, I take a simplified approach and approximate the effect of compliant pores by modifying only the viscosity matrices in the two-phase model given by relations (3.3). This simplification is analogous to those by Murphy et al. (1986), Dvorkin et al. (1995) and Gurevich et al. (2010), who included the effects of squirt flows in the VE modulus of the solid frame. Indeed, similarly to fluids, viscous stresses (related to strain rates) can be expected in solids (Landau and Lifshitz, 1986), which makes the effective moduli "viscoelastic." However, viscous effects may also extend to the coupling between the solid and the fluid in stiff pores, which means that viscosities $\boldsymbol{\eta}_K$ and $\boldsymbol{\eta}_\mu$ must be matrix quantities (Figure 4.1).

To see how solid viscosities arise for squirt flows, consider a relatively slow deformation in which the kinetic energy of the fluid in compliant pores is negligible. One can then make two simple observations. First, the spatially-averaged velocity of squirt flows

within a deformed volume must be proportional to the strain rate, $\dot{\boldsymbol{\varepsilon}}_{ij}$, and therefore the averaged squared velocity, $\left\langle v_{\text{squirt}}^2 \right\rangle$, is proportional to $\left(\dot{\boldsymbol{\varepsilon}}_{ij}\right)^2$ (Figure 4.1). Second, from dimensionality considerations, this average $\left\langle v_{\text{squirt}}^2 \right\rangle$ is also proportional to the square of the characteristic scale length of the pores. The relevant scale length is the gap width of the compliant pores, which I denote *z*. Therefore, the average squared squirt-flow velocity can be expressed as products of z^2 with the only two rotational invariants of the strain-rate tensor, similarly to the construction of functions *L* and *D* in relations (3.3) (Figure 4.1):

$$\left\langle v_{\text{squirt}}^2 \right\rangle = z^2 \left(\frac{1}{2} \dot{\boldsymbol{\Delta}}^T \mathbf{S}_K \dot{\boldsymbol{\Delta}} + \dot{\tilde{\boldsymbol{\varepsilon}}}_{ij}^T \mathbf{S}_\mu \dot{\tilde{\boldsymbol{\varepsilon}}}_{ij} \right), \tag{4.2}$$

where $\mathbf{S}_K$ and $\mathbf{S}_\mu$ are dimensionless 2×2 "form-factor" matrices describing the effects of the strains of the rock frame and its pore fluid (in stiff pores) on the squirt-flow velocities. These effects are determined by the geometries and statistics of compliant pores and the compressibility of the pore fluid relative to the matrix.

The average squirt-flow velocities (4.2) cause two modifications of the macroscopic Lagrangian and dissipation function in relations (3.3). First, they increase the kinetic energy by:

$$\delta L_{\text{squirt}} = \frac{1}{2} \phi_c \rho_{fl} \left\langle v_{\text{squirt}}^2 \right\rangle = \frac{1}{2} \phi_c \rho_{fl} z^2 \left(\frac{1}{2} \dot{\boldsymbol{\Delta}}^T \mathbf{S}_K \dot{\boldsymbol{\Delta}} + \dot{\tilde{\boldsymbol{\varepsilon}}}_{ij}^T \mathbf{S}_\mu \dot{\tilde{\boldsymbol{\varepsilon}}}_{ij} \right). \tag{4.3}$$

Second, squirt-flow velocity also increases the dissipation function by:

$$\delta D_{\text{squirt}} = \frac{1}{2} \phi_c D_0 \left\langle v_{\text{squirt}}^2 \right\rangle = \frac{1}{2} \phi_c D_0 z^2 \left(\frac{1}{2} \dot{\boldsymbol{\Delta}}^T \mathbf{S}_K \dot{\boldsymbol{\Delta}} + \dot{\tilde{\boldsymbol{\varepsilon}}}_{ij}^T \mathbf{S}_\mu \dot{\tilde{\boldsymbol{\varepsilon}}}_{ij} \right), \tag{4.4}$$

where $D_0 = 12\eta / z^2$ is the viscous hydrodynamic resistance of a narrow channel in a Poiseuille flow (equation (17) in Murphy et al., 1986). Compared to Murphy et al. (1986), D_0 in eq. (4.4) is multiplied by *z* because it is related to the average flow velocity (u_r in

Murphy et al., 1986) and not to the volume flow rate. Adding the kinetic energy δL_{squirt} to the Lagrangian is, generally speaking, necessary, but with low ϕ_c, it would make a relatively small correction to the kinetic energy already contained in L (equation (3.13)). Modifications of the kinetic energy caused by squirt flows (equation (4.3)) are not considered in the theoretical treatments by Murphy et al. (1986), Dvorkin et al. (1995), and Gurevich et al. (2010), and I will similarly disregard them here.

In contrast to the kinetic energy, the modification of the dissipation function (equation (4.4)) is significant because the poroelastic D contains no similar terms. From relation (4.4), squirt flows produce macroscopic internal friction characteristic of solid viscosity (terms in parentheses in the second equation (3.3). The corresponding bulk and shear viscosity matrices are:

$$\boldsymbol{\eta}_K = 6\phi_c \eta \mathbf{S}_K \text{ and } \boldsymbol{\eta}_\mu = 6\phi_c \eta \mathbf{S}_\mu . \tag{4.5}$$

This solid viscosity is linear (meaning that D_0 is constant and therefore functions L and $D + \delta D$ squirt are quadratic with respect to the strains and strain rates) up to the frequencies of about 1 MHz (Murphy et al., 1986).

4.3.3 Low-frequency Approximation

Similar to solving for effective media models in elasto-statics (e.g., Eshelby, 1957) evaluation of the form-factor matrices $\mathbf{S}_K$ and $\mathbf{S}_\mu$ in equations (4.5) requires solving for the microscopic deformation in the presence of the specific volumes, shapes, topologies, and connectivities of the network of compliant and stiff pores (Figure 4.1; Morozov and Deng, 2016b). For disconnected “penny-shaped” compliant pores, evaluation of these matrices involves modeling radial Poiseuille flows with appropriate boundary conditions at the edges, as in the existing approaches (Murphy et al., 1986; Dvorkin et al., 1995; and

Gurevich et al., 2010). A common assumption of these models is that compliant pores do not participate in the global Darcy flow and consequently do not modify the matrix **d** (equation (3.13)). I also uphold this assumption here and focus on the resulting viscosity matrices.

Instead of detailed derivations for the different microscopic models, in this Chapter, I only consider the model by Gurevich et al. (2010) and obtain matrices $\mathbf{S}_K$ and $\mathbf{S}_\mu$ indirectly, from the low-frequency asymptote of its effective moduli. At low frequencies, we can keep only linear terms in all dependences on ω. The effective frame modulus by Gurevich et al. (2010) equals:

$$K_D^* = K_{cD}\left[1 - i\omega\eta\frac{3\gamma^2}{8\phi_c\sigma^2 K_{cD}}\right], \tag{4.6}$$

which is the equation (26) by Gurevich et al. (2010), where I substituted the expression for the complex wavenumber k^* for the diffusion wave of the fluid flow within a compliant pore (equation (21) in Gurevich et al. (2010)):

$$k^{*2} = \frac{12i\omega\eta}{z^2 K_{fl}}. \tag{4.7}$$

In these expressions, K_{cD} is the elastic bulk modulus of the dry matrix, K_h is the bulk modulus of a hypothetical dry rock with compliant pores absent, $\gamma \equiv 1 - K_{cD}/K_h$ is the relative increase in the dry modulus caused by removing the compliant pores, σ is the aspect ratio, and η is the viscosity of the pore fluid, and z is the thickness of the pore gap. These formulas were also changed according to our sign convention for the exponent of the harmonic plane wave: $u \propto \exp(-i\omega t + ikx)$, which follows Landau and Lifshitz (1986) and Aki and Richards (2002) but is opposite to Gurevich et al. (2010) and Carcione and Gurevich (2011).

The expression (4.6) can be written as (Landau and Lifshitz, 1986):

$$K_D^* = K_{cD} - i\omega\eta_{KD}, \tag{4.8}$$

where η_{KD} can be called the effective bulk viscosity of the modified frame:

$$\eta_{KD} = \eta \frac{3\gamma^2}{8\phi_c \sigma^2}. \tag{4.9}$$

This effective viscosity is proportional to η but much larger because of the small aspect ratio $\sigma \ll 1$ Note that this viscosity does not depend on K_{fl}. Quantity γ is proportional to ϕ_c (Shapiro, 2003) and therefore η_{KD} also increases with compliant porosity. Through ϕ_c and σ, this viscosity also depends on the confining pressure.

Equation (4.6) shows that at low frequencies, the modified frame by Gurevich et al. (2010) behaves as a Kelvin-Voigt solid with relatively large bulk viscosity. The inverse Q factor for a "bulk wave" in this solid is proportional to frequency as:

$$Q_{KD}^{-1} = \omega \frac{\eta_{KD}}{K_{cD}}. \tag{4.10}$$

I can now constrain the low-frequency range in which the above equations are valid. The first constraint is given by relation $\omega \ll K_{cD} / \eta_{KD}$, which can also be written as $Q_{KD}^{-1} \ll 1$, or:

$$\omega \ll \frac{8\phi_c \sigma^2 K_{cD}}{3\eta\gamma^2}. \tag{4.11}$$

An additional condition on low frequencies comes from relation (23) in Gurevich et al. (2010). In the notation of this dissertation, this condition is:

$$|ka|^2 \ll \frac{8\phi_c K_{cD}}{\gamma K_f} \tag{4.12}$$

or in terms of frequency:

$$\omega \ll \frac{8\phi_c \sigma^2 K_{cD}}{3\eta\gamma} \tag{4.13}$$

Above this frequency, the real part of the modulus K_D^* (equation (4.6)) is frequency-dependent (Gurevich et al., 2010). The constraints (4.11) and (4.13) differ by a constant factor γ.

Further in the model by Carcione and Gurevich (2011), the modified frame modulus is used to derive the undrained modulus from Gassmann's equation. It is convenient to perform this derivation in three steps. First, the Biot-Willis coefficient $\alpha = 1 - K_{cD}/K_s$ attains a positive complex part: $\alpha^* = \alpha + i\omega\tau_\alpha$, where the "relaxation time" equals:

$$\tau_\alpha = \frac{\eta_{KD}}{K_s}. \tag{4.14}$$

As above, the linearity in frequency approximation is subject to the constraint $\omega \ll K_s/\eta_{KD}$, which differs from the constraint (4.11) by a factor of order one. Next, the poroelastic modulus *M* satisfies Gassmann's equation:

$$M = \frac{1}{(\alpha - \phi)K_s^{-1} + \phi K_{fl}^{-1}}, \tag{4.15}$$

where ϕ is the stiff porosity. In the VE model by Carcione and Gurevich (2011), this equation is also considered valid for complex-valued α. Therefore, at low ω, modulus *M* is modified to $M^* = M - i\omega\eta_M$, where the "effective viscosity" associated with *M* equals:

$$\eta_M = \tau_\alpha \frac{M^2}{K_s} = \eta_{KD}\frac{M^2}{K_s^2}. \tag{4.16}$$

Finally, the undrained modulus equals $K_U = K_{cD} + \alpha^2 M$ (Bourbié et al., 1987), and Carcione and Gurevich (2011) also extend this equation to complex moduli at nonzero frequencies. Denoting the complex-valued K_U by $K_U^* = K_U - i\omega\eta_{KU}$, the corresponding "effective viscosity" becomes:

$$\eta_{KU} = \eta_{KD} - 2\alpha\tau_\alpha M + \alpha^2\eta_M = \\ = \eta_{KD}\left[1 - 2\alpha\frac{M}{K_s} + \left(\alpha\frac{M}{K_s}\right)^2\right] = \eta_{KD}\left(1 - \alpha\frac{M}{K_s}\right)^2. \quad (4.17)$$

With the above complex moduli, the complex-valued Biot's rigidity matrix **K** in relations (3.13) becomes:

$$\mathbf{K}^* = \begin{bmatrix} K_U^* & -\alpha^* M^* \\ -\alpha^* M^* & M^* \end{bmatrix}. \quad (4.18)$$

Again keeping the first-order terms with respect to $\omega\tau_\alpha$ and $\omega\tau_M$, this matrix can be written as:

$$\mathbf{K}^* = \mathbf{K} - i\omega\boldsymbol{\eta}_K, \quad (4.19)$$

where the poroelastic matrix modulus **K** is the same as in relations (3.13), and the bulk viscosity matrix equals:

$$\boldsymbol{\eta}_K = \begin{bmatrix} \eta_{KU} & -\tau_\alpha M + \alpha\eta_M \\ -\tau_\alpha M + \alpha\eta_M & \eta_M \end{bmatrix} = \eta_{KD}\begin{bmatrix} \chi^2 & -\frac{M}{K_s}\chi \\ -\frac{M}{K_s}\chi & \frac{M^2}{K_s^2} \end{bmatrix}, \quad (4.20)$$

where it is denoted using $\chi \equiv 1 - \alpha M / K_s$. Note that the structure of this matrix is similar to those of matrices $\boldsymbol{\rho}$ and **K** in relations (3.13). Thus, at low frequencies, the model by Carcione and Gurevich (2011) is equivalent to a GLS (equations (3.3).; Morozov and Deng, 2016) with Darcy-flow friction caused by stiff pores and Newtonian bulk viscosity due to compliant pores.

To estimate the contribution of squirt flows to the shear-viscosity matrix $\boldsymbol{\eta}_\mu$, I further use the relation for modified frame moduli from Mavko and Jizba (1991) (formula (4) in Gurevich et al. (2010)), which I write as:

$$\frac{1}{\mu_D^*} - \frac{4}{15}\frac{1}{K_D^*} = \frac{1}{\mu_{cD}} - \frac{4}{15}\frac{1}{K_{cD}}, \quad (4.21)$$

where μ_{cD} is the shear modulus of dry matrix and μ_D^* is the effective shear modulus due to squirt flows. This relation was inferred by Mavko and Jizba (1991) from directional averaging of the VE compliances orthogonal to the planar compliant pores. At frequencies satisfying the constraints (4.11) and (4.13), the effect of squirt flow adds small terms $-i\omega\eta_{\mu D}$ and $-i\omega\eta_{KD}$ to μ_{KD} and K_{cD}, and consequently:

$$\frac{i\omega\eta_{\mu D}}{\mu_{cD}^2}-\frac{4}{15}\frac{i\omega\eta_{KD}}{K_{cD}^2}=0\,. \tag{4.22}$$

Therefore, the squirt-related shear viscosity of dry rock is related to the bulk one by the following factor:

$$\upsilon\equiv\frac{\eta_{\mu D}}{\eta_{KD}}=\frac{4}{15}\left(\frac{\mu_{cD}}{K_{cD}}\right)^2, \tag{4.23}$$

and the resulting shear-viscosity matrix equals:

$$\boldsymbol{\eta}_\mu=\eta_{KD}\upsilon\begin{bmatrix}1 & 0\\ 0 & 0\end{bmatrix}. \tag{4.24}$$

In terms of viscosity values, the pressure caused by internal friction in a P-wave is a combination of the bulk and shear pressures:

$$\eta_{\mathrm{P}D}=\eta_{KD}+\frac{4}{3}\eta_{\mu D}=\eta_{KD}\left(1+\frac{4}{3}\upsilon\right). \tag{4.25}$$

This relation is analogous to the expression for the elastic P-wave modulus. Similarly to the elastic moduli, matrices $\boldsymbol{\eta}_K$ and $\boldsymbol{\eta}_\mu$ can be used to produce solid viscosities corresponding to other shapes of elastic deformations. In particular, a Lamé-type viscosity matrix can be defined by $\boldsymbol{\eta}_\lambda=\boldsymbol{\eta}_K-2\boldsymbol{\eta}_\mu/3$.

4.4 Comparison to Squirt-Flow Models and Data

In this section, I derive the P-wave velocities and *Q* factors in sandstone resulting

from the solid-viscosity model (4.20) and (4.24) and compare them to four squirt-flow models from the literature (Murphy et al., 1986; Dvorkin et al., 1995; Pride et al., 2004; and Gurevich et al., 2010). The mechanical properties of the medium are shown in Table 4.1. Most of the literature models contain tuning parameters such as characteristic pore radii or transport coefficients. These parameters were adjusted by making the predicted frequency dependences of Q close for all models (Figure 4.2 and Figure 4.3).

Table 4.1: Mechanical properties of brine-saturated sandstone (Carcione and Gurevich, 2011)

Solid		
K_{cD}	18 GPa	Bulk modulus of dry matrix
K_h	20 GPa	Bulk modulus
K_s	50 GPa	Bulk modulus of solid grains
μ_{cD}	12 GPa	Shear modulus of dry matrix
ρ_s	2650 kg/m3	Density of solid grains
ϕ	0.2	Porosity
ϕ_c	0.0002	Soft porosity
σ	0.0004	Grain-contact aspect ratio
κ	200 mD	Permeability
τ	2.3	Tortuosity
Brine		
K_{fl}	2.25 GPa	Bulk modulus
ρ_{fl}	1040 kg/m3	Density

In the GLS model, there exist no frequency-dependent effective moduli of the frame, and therefore the comparison has to be carried out with respect to the observable wave speeds and attenuation in fluid-saturated rock. The comparison is performed by solving the wave equation (4.1) and evaluating the frequency-dependent P-wave velocities and Qs.

With sandstone parameters listed in Table 4.1, the squirt-viscosity matrices (4.20) and (4.24) equal

$$\boldsymbol{\eta}_K = \begin{bmatrix} 0.88 & -0.21 \\ -0.21 & 0.05 \end{bmatrix} \times 10^8 \text{ cP} \quad \text{and} \quad \boldsymbol{\eta}_\mu = \begin{bmatrix} 0.14 & 0 \\ 0 & 0 \end{bmatrix} \times 10^8 \text{ cP}. \tag{4.26}$$

Note that matrix $\boldsymbol{\eta}_K$ is clearly nondiagonal, showing the importance of bulk viscous coupling

between the frame and pore fluid (called "Biot-consistency" by Thomsen, 1985). The elements of $\boldsymbol{\eta}_K$ and $\boldsymbol{\eta}_\mu$ are much larger than the viscosity of brine (approximately 1 cP), showing that the thin films of fluid confined in compliant cracks dissipate much more energy per unit volume than a uniform fluid. These levels of $\boldsymbol{\eta}_K$ and $\boldsymbol{\eta}_\mu$ are lower but comparable to the viscosity $\eta \approx 3.8 \cdot 10^9$ cP for shale estimated from field data by Ricker (1941). This comparison suggests that squirt flows represent a likely mechanism of internal friction under field conditions, where they should be complemented by other fluid-related mechanisms such as wave-induced fluid flows (Müller et al., 2010). The squirt-related viscosity could also reach Ricker's (1941) values if the pore fluid had a viscosity of about 100 cP, such as in bitumen (gray-dot line in Figure 4.4), or if the compliant-pore aspect ratio equaled $\sim 4 \cdot 10^{-5}$ (grey-dot line in Figure 4.5). The spectral peak of wave attenuation would then appear within the seismic range of 10 to 100 Hz.

GLS results in Figures 4.2 and 4.3 are nearly identical to those by Murphy et al. (1986), showing that their model effectively represents an estimate of solid viscosity. With the exception of the model by Dvorkin et al. (1995), the predictions of P-wave Q^{-1} and velocity dispersion are similar in the existing models at frequencies up to about 1 kHz (Figure 4.1). This frequency limit corresponds to the low-frequency range by Gurevich et al. (2010) used in our approximation. At these frequencies, all models in Figure 4.2 show little velocity dispersion. Above ~1 kHz, the GLS and Murphy's et al. (1986) model show an increased V_P compared to the models by Dvorkin et al. (1995), Pride et al. (2004), and Gurevich et al. (2010) (Figure 4.2). These increases are due to reduced deformation of the compliant pores, which is accounted for by using the Gassmann's equation with respect to the compliant porosity. This effect is caused by the elastic-forces within the compliant pores,

which are not considered in our two-phase GLS model. A very strong dispersion occurs in the GLS and Murphy's et al. (1986) models above about 10 kHz (Figure 4.2).

The inverse P-wave Q factor in the GLS model shows a good agreement with all other models below 1 kHz (Figure 4.3). In the GLS and Murphy's et al. (1986), the Q^{-1} increases near-linearly at all frequencies (Figure 4.3), which is characteristic of linear viscosity (Landau and Lifshitz, 1986). In the rest of the models, stronger velocity dispersion occurs at frequencies corresponding to the plateaus in $Q^{-1}(\omega)$ (Figure 4.2).

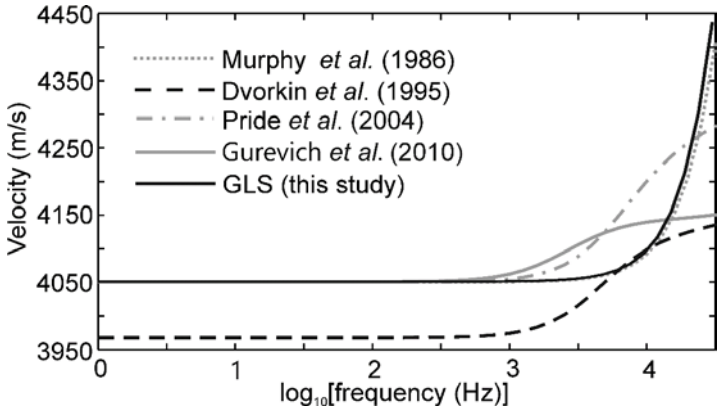

Figure 4.2. Frequency dependence of P-wave velocity for five squirt-flow models (legend). Material properties are shown in Table 4.1.

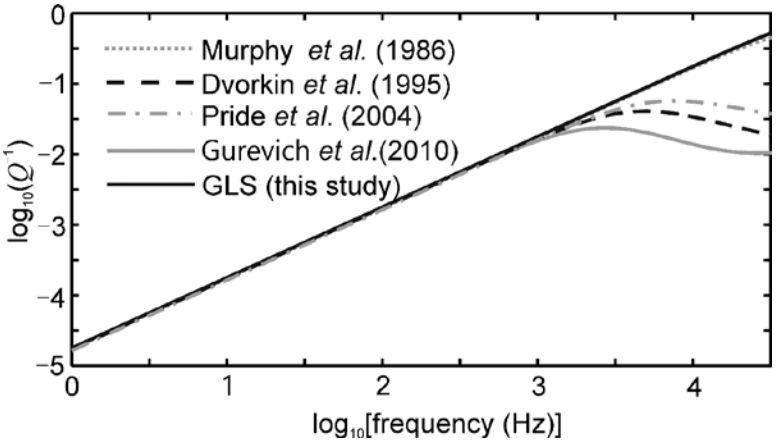

Figure 4.3. Frequency-dependent P-wave attenuation for the GLS model (black line) and other squirt-flow models. Material properties are shown in Table 4.1.

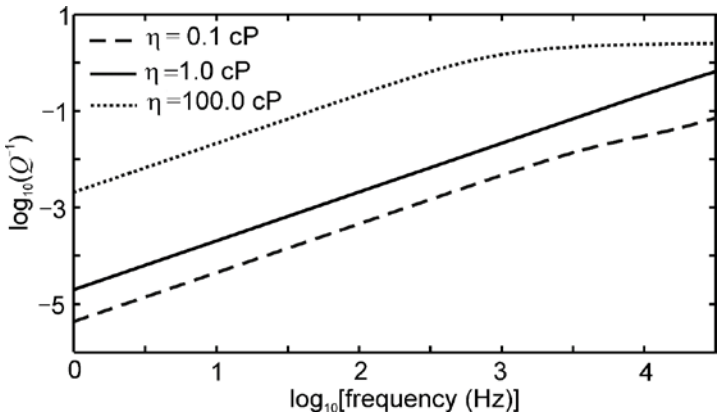

Figure 4.4. P-wave attenuation in the GLS model with different viscosities of the fluid in compliant pores.

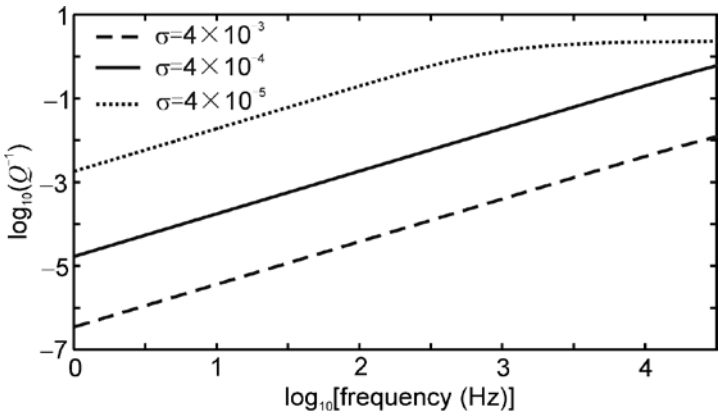

Figure 4.5. Attenuation factors modeled in the GLS model for three values of the aspect ratio σ of compliant pores.

At lower frequencies, the attenuation rate increases as approximately $Q^{-1} \propto \omega$ in all models as expected from linear Newtonian viscosity (Figure 4.3). To show that the attenuation modeled in Figure 4.3 is due to the solid (squirt-flow related) viscosity and not to Biot's poroelasticity, I compute several models with different values of fluid viscosity (Figure 4.4). It is well known that with increasing viscosity of the pore fluid, Biot's dissipation peak moves toward higher frequencies. By contrast, in the GLS and other squirt-flow models, the attenuation peak moves toward lower frequencies with increasing fluid viscosities (Figure 4.4). Such opposite dependences on fluid viscosity were recognized by many researchers (e.g., Rubino et al., 2009) and represent the key discriminants between

these internal-friction mechanisms. In Figure 4.5, I also show the P-wave attenuation predicted by the GLS model with a constant fluid viscosity equal 1 cP and variable aspect ratios of compliant pores. The effect of increasing σ is analogous to that of decreasing pore-fluid viscosity. This result is also consistent with the model by Pride et al. (2004) and other squirt-flow models.

In Figure 4.6, I compare the predictions of the GLS model for shear waves to laboratory observations in Berea sandstone by Winkler and Nur (1982) and Jones and Nur (1983). These observations were also used by Murphy et al (1986). The aspect-ratio in the GLS model is taken equal 1.2×10^{-4}, which is close to the value of 1.0×10^{-4} used by Murphy et al (1986). The dry shear modulus is estimated from the velocities at low frequencies (Jones and Nur, 1983). GLS predictions (solid lines in Figure 4.6b) are close to those by Murphy et al (1986) (Figure 4.2 and Figure 4.3), and hence the data comparisons are similar. The velocity dispersions are in good agreement with the observations by Winkler and Nur (1982) (black circles in Figure 4.6a, shown as frequency dependence of the effective shear modulus $\mu(\omega) \equiv \rho V_S^2(\omega)$). The results for Q_S^{-1} are close to the data by Jones and Nur (1983) below about 1 kHz (Figure 4.6b). Although the Jones-Nur and Winkler-Nur datasets have a good agreement in attenuation, they significantly disagree in shear-modulus dispersion (Figure 4.6a). As noted by Jones and Nur (1983), this difference could be due to inferring the frequency-dependent modulus from measurements made at variable temperatures. The strong dispersion observed by Jones and Nur (1983) (gray symbols in Figure 4.6a) is likely not dynamic and caused by hardening of the shear modulus at lower temperatures. By contrast, Winkler and Nur (1982) used standing waves within rock samples at a constant temperature. Such conditions are within the scope of the basic wave-mechanics model (3.3), and the

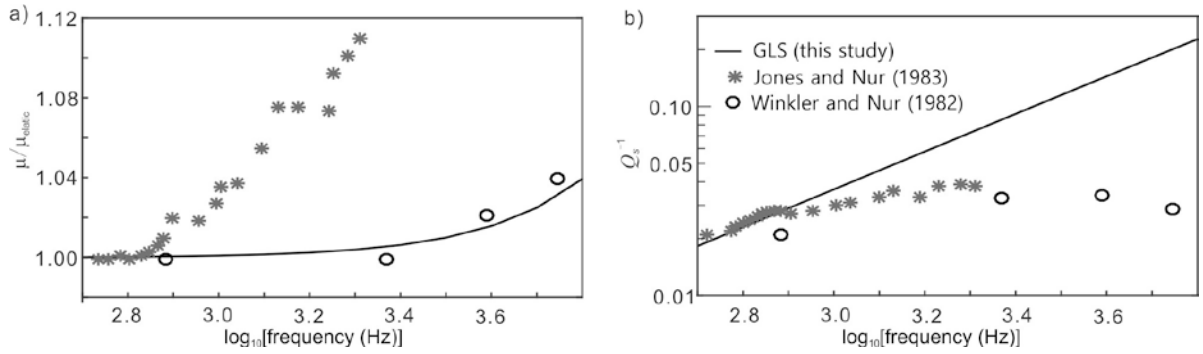

Figure 4.6. Comparison between the GLS model (black lines) and observed data (legend) (a) Dispersion of the effective shear modulus $\mu = \rho V_S^2$; (b) shear attenuation Q_S^{-1}.

agreement with the observations is reasonable (Figure 4.6). The matching frequency dependences of Q_S^{-1} in the Jones-Nur and Winkler-Nur datasets (Figure 4.6b) suggest that similarly to fluid viscosity, squirt-flow viscosity obeys the temperature-frequency scaling relations.

4.5 Discussion

The matching predictions of the attenuation and dispersion spectra (Figure 4.2, Figure 4.3, and Figure 4.6) corroborate the GLS model (equations (3.3), (4.20) and (4.24)) at lower frequencies. However, this model is much more significant than yet another empirical model matching the spectra. The GLS model reveals the common reason for the $Q^{-1}(\omega)$ being nearly proportional to ω in all squirt-flow models (Figure 4.3) at seismic frequencies. This reason consists in compliant fluid-filled pores producing linear solid viscosity of the rock frame. Appropriate combinations of tuning parameters in these models (e.g. radii and aspect ratios of the compliant pores and viscosities of pore fluid) lead to the levels of solid viscosity estimated in section 4.4. The resulting solid-viscosity matrices explain the observed relations $Q^{-1}(\omega)$ and $V(\omega)$ for plane waves.

The GLS model differs from all other models by being based on macroscopic

continuum mechanics instead of empirical relations and correspondence-principle based analogies. This difference yields major methodological advantages:

All constitutive properties are time- and frequency-independent, and the dynamics of the material is described by time-domain differential equations of mechanics. Because the constitutive properties are frequency-independent, they can be measured and compared not only for waves but in any kind of physical experiments. There is no need for postulating material memory and implementing it by memory integrals in finite-difference simulations.

The mechanical formulation is much more general and powerful than effective-moduli models. It is valid for any deformations even including those that do not satisfy the equations of motion (Landau and Lifshitz, 1986). All mechanical effects are contained in the simple and compact expressions (3.3). Expressions (3.3) clearly separate viscosity effects from those of Darcy flows and inertia. These expressions are also straightforward to extend to multiple pore geometries and pore fluids, and nonlinearity (Morozov and Deng, 2016a).

The model reveals that similar to elasticity, there exists viscous coupling between the rock frame and pore fluid, as described by matrices (4.20) and (4.24). This point should be of the most practical importance. None of the observable moduli (drained, undrained, or of solid grains) are truly "viscoelastic," i.e. contain well-defined viscosities. Only the matrix moduli $\mathbf{K}$ (or μ) and viscosities $\boldsymbol{\eta}_K$ ($\boldsymbol{\eta}_\mu$) in equations (3.13) can be combined to form VE moduli. Note that when considering Biot's poroelastic friction ($\mathbf{d} \neq \mathbf{0}$ in equations (3.13)), the density matrix $\boldsymbol{\rho}$ also becomes complex-valued by virtue of the correspondence principle (Morozov and Deng, 2016a).

Frequency-domain models of squirt and more general pore-fluid flow effects (Thomsen, 1985; Murphy et al., 1986; Mavko and Jizba, 1991; Dvorkin et al., 1995; Pride et

al., 2004; Rubino, et al., 2009; Gurevich et al., 2010; Müller, et al., 2010) focus on expressing the frequency-dependences of phase velocities and attenuation rates of plane harmonic waves (Figure 4.2 and Figure 4.3). By contrast, the goal of the GLS model is much broader and consists in solving these and also any other mechanical problems. For example, Appendix A outlines a 1-D numerical scheme obtained by finite differencing (FD) of the equations of motion (4.1). The solid viscosity simply gives an additional viscous stress field ξ proportional to the strain rates, and no memory variables are needed. In agreement with Biot consistency (Thomsen, 1985), the FD scheme is of matrix form and models the stiff-pore fluid flows along with the deformation of the porous frame (Appendix A). For comparison, FD modeling of pore-fluid flow requires construction of as many as five Zener's bodies in the effective-moduli models (Carcione and Gurevich, 2011; also see section 4.2). With zero P-wave viscosity ($\boldsymbol{\eta}_K + 4\boldsymbol{\eta}_\mu / 3 = \mathbf{0}$), this FD scheme reduces to Biot's poroelasticity.

In Figure 4.7, a FD solution is illustrated for a P wave in a brine-saturated sandstone (Table 4.1). An explosive source is simulated by a Gaussian function $s(t) = \exp\left(-\pi f_0 t^2\right)$, with dominant frequency f_0 =1 kHz and peak pressure occurring at time zero. The source pressure is partitioned between the fluid- and solid-phase pressures as $p_2(t) = \phi s(t)$ and $p_1(t) = (1-\phi)s(t)$ respectively, where ϕ is the porosity (Table 4.1). The time step and spatial interval are selected in the usual manner, in order to suppress numerical dispersion. The FD modeling predicts both the fluid- and solid-phase pressures in the GLS model (Figure 4.7).

In Figure 4.7, note that compared to the pulse of average rock particle velocity being

always positive, the fluid flow is bipolar and changes from positive to negative upon passage of a wave. With the solid viscosity (squirt flows) present, both of these displacement pulses are attenuated during propagation, which can be observed from reducing amplitudes and increasing durations of the wavelets (Figure 4.7). The attenuation is dominated by solid viscosity, because the dominant frequency f_0 is far below Biot's characteristic frequency. The slow P wave appears to dissipate quickly and is not visible in the first snapshot shown at 5 ms (Figure 4.7).

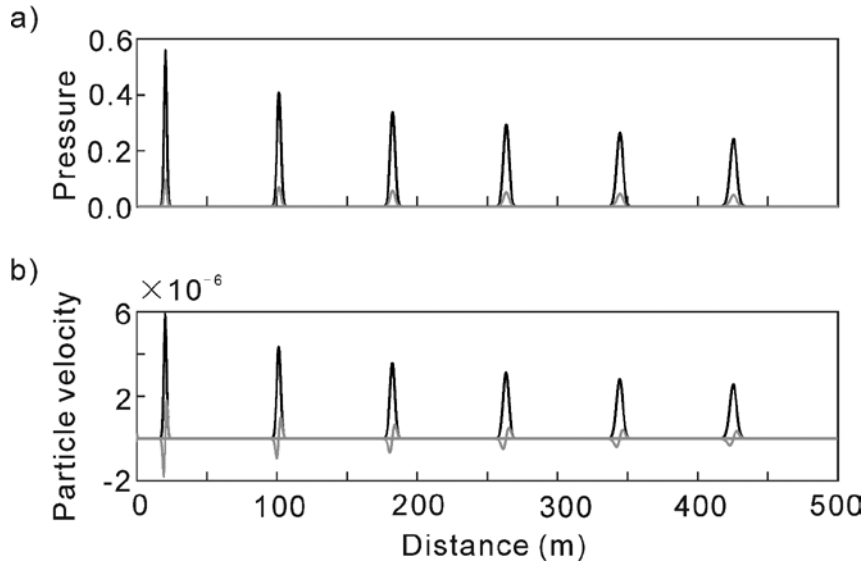

Figure 4.7. Plane P-wave waveforms modeled at times t = 5, 25, 45, 65, 85 and 105 ms: a) Pressure within the rock frame (black) and pore fluid (gray); b) Particle velocities of rock frame (black) and pore fluid (gray). Pore-fluid velocities are multiplied by scalar 1000 for display.

The traditional effective-moduli based models can be difficult to use and ambiguous when applied to heterogeneous media or deformations different from harmonic plane waves. For example, wave propagation in a finely-layered poroelastic medium (the case of wave-induced flows; Müller et al., 2010) depends on boundary conditions for pore flows between the layers (Morozov, 2015; Morozov and Deng, 2016b). Such boundary conditions cannot be specified in effective-moduli models. For another example, consider a standard creep

experiment with a specimen of porous, fluid-saturated rock. To describe such quasi-static deformation by an effective-moduli theory, one would need to construct an elaborate arrangement of five time-dependent poroelastic moduli (Carcione and Gurevich, 2011; also section 4.2). This arrangement would depend on whether the rock specimen or its parts are hydraulically insulated or not, which could become an intractable problem. By contrast, in the GLS model (equations (3.3), (4.3) and (4.4)), such problems are solved by routine equations of mechanics (equation 3) with the appropriate boundary and initial conditions (Landau and Lifshitz, 1986). All variables and parameters in equations (3.3) and (3.13) are well-defined quantities measurable in physical experiments. The GLS method is entirely based on first-principle physics and is consequently much simpler, powerful and more dependable than effective-moduli calculations.

The recognition of solid viscosity as a true physical property of the material behind the effective frequency-dependent moduli should have numerous practical applications. First, this recognition shows in what way the different squirt-flow models are equivalent. When interpreting field and laboratory observations, matrix solid viscosity could be a useful link and a common language for describing other internal-friction phenomena, such as wave-induced fluid flows (Müller et al., 2010; Morozov and Deng, in review). Further, if solid viscosity is an independent physical property similar to the viscosity of fluids, it can manifest itself in observations different from the usual assessments of Q^{-1} and dispersion for waves (Figure 4.2 and Figure 4.3). For example, the solid viscosity could be measured in creep or some new types of rheometric measurements for solids. As a physical property similar to the viscosity of fluids, solid viscosity should directly depend on the temperature, mineral composition, fluid content, and pore structure of rock. All of these properties could be

important for enhanced oil recovery or seismic monitoring of CO_2 storage. In particular, one can expect that an increase in CO_2 content should increase the solid viscosity and consequently the attenuation rate, which could be observed by seismic methods. Bitumen sands (e.g., Spencer, 2013) are another type of rock representing a multi-phase viscous solid, which should benefit from the basic viscosity model (3.3)

4.6 Conclusion

In this Chapter, I propose a macroscopic model describing the effects of squirt flows in porous rock by its effective solid viscosity. The model is based on Lagrangian continuum mechanics, time- and frequency-independent constitutive properties, and time-domain differential equations for the medium. The model shows that for porous fluid-saturated rock, there exists elastic, viscous, and inertial coupling between the rock frame and pore fluids. The elasticity, viscosity, and densities of porous fluid-saturated rock are therefore matrix properties.

The elements of the squirt-flow solid-viscosity matrix for sandstone are of the order of 10^6–10^8 cP. For implementation in waveform simulation software, the model requires neither internal variables, equivalent linear solids nor material memory typical for VE formulations. At seismic frequencies below about 1 kHz, the P-wave velocities and attenuation predicted by this model agree with data and the existing squirt-flow models. Similarly to the viscosity of fluids and gases, the viscosity of porous rock should be sensitive to temperature, pore-fluid content, mineral composition, and microscopic heterogeneity. Due to its origin in rigorous continuum mechanics, the approach is much more powerful than effective-moduli models and is applicable to all problems involving wave propagation and transient deformations in heterogeneous media and finite rock bodies.

CHAPTER 5

NONLINEAR SEISMIC WAVE PROPAGATION IN HEAVY OIL

In this Chapter, I analyze the effects of heavy oil by considering ultrasonic laboratory experiments with a proxy of heavy oil recently conducted at the University of Calgary. The design and initial interpretation of these experiments (Lines et al. 2014) was based on the concept of *Q* and viscoelastic relations, and consequently, several key observations remained quantitatively unexplained. Similarly to other applications in this dissertation, I show that the GLS framework (Chapter 3) allows a comprehensive explanation of the experiments and suggests a nonlinear behavior of the material in the near-source regions. The presentation in this Chapter is based on the following paper:

***Deng, W.**, and I. B. Morozov. 2014, Nonlinear seismic wave propagation in heavy oil. GeoConvention 2014, Calgary, Canada, http://www.geoconvention.com/archives/2014/150_GC2014_Nonlinear%20Modeling%20for%20Heavy%20Oil.pdf*

 This Chapter represents an expanded version of the above paper, which is also included as modeling part in Morozov and Deng (submitted to *Canadian Journal of Exploration Geophysics*). The text was also modified and reformatted for incorporation in the present dissertation.

5.1 Abstract

The propagation, reflectivity, and attenuation of seismic waves in bitumen-rich rocks and heavy oils can be difficult to explain by traditional viscoelastic concepts such as the *Q* factor. Heavy oils are likely non-Newtonian, and both viscosity and elasticity in them can be

nonlinear. Recent lab experiments with Crisco vegetable shortening (Lines et al., 2014) produced several remarkable observations useful for understanding such media: 1) low amplitudes of directly propagating waves and 2) their low dominant frequencies, and 3) very strong negative reflectivity from the water-Crisco contact. Here, I propose a nonlinear model explaining these observations. The Crisco shortening is interpreted as a viscous (Voigt) solid/fluid with strongly nonlinear behaviour at high strains. This nonlinearity affects a narrow zone extending to 1-2 wavelengths from the source or from the water-Crisco boundary. This zone is responsible for all three key effects listed above. Beyond this zone, wave propagation is near-linear and similar to that in Crisco altered by melting and re-solidification. Notably, the reflections from unaltered Crisco in water are strong and of negative polarity, showing that they are caused by a dynamically-reduced effective modulus. By contrast, seismic reflections from altered Crisco are much weaker and phase-rotated, which suggests that they are caused by contrasts in viscosity. Thus, physical properties such as nonlinear moduli and viscosity (and not so much the *Q*) provide a good way for explaining the behaviour of seismic waves in viscous-fluid rich or fluid-like solids.

5.2 Introduction

When considering wave propagation and reflectivity in weakly attenuative media or corrections for attenuation effects in seismic data processing (Chapter 7 of this dissertation), the viscoelastic quality factor (*Q*) is a convenient property representing the internal friction within materials (Lines et al., 2008; Reine et al. 2012; van der Baan, 2012; Lines et al. 2014). The use of *Q* allows modeling the observed attenuation effects, and it is relatively easy to implement in numerical algorithms (e.g., Zhu, et al. 2013). However, as shown in Chapters 3 and 4, the viscoelastic *Q* is insufficient for describing global-flow effects in porous fluid-

saturated rock. For media without global flows but with strong dissipation, such as viscous heavy oil, specifying the Q alone is also incomplete and insufficient for describing the behavior of seismic waves. In such cases, we also need to look for a more complete physical picture and identify the true physical parameters responsible for seismic attenuation.

The difficulties of the conventional Q-based model for heavy oil can be demonstrated using the recent results of ultrasonic measurements of acoustic wave propagation and reflections in Crisco shortening (Wong and Lines, 2013 and Lines et al. 2014). Crisco shortening is a popular solidified (hydrogenated) vegetable shortening. In addition to cooking, Crisco is sometimes used to test acoustic-wave effects in viscous oils in the laboratory. Wong and Lines (2013) measured the reflectivity of the water-Crisco contact and found it to be of negative-polarity and surprisingly strong, close to about –0.7. This result could be explained neither by the difference in impedances (ρV, which is very small for Crisco and water) nor by the effect of a very low Q (which would cause a 90°-rotated reflection; Lines et al., 2014). In addition, the very low Q (~0.3 to 3) required for such reflectivity would also disagree with the observations of direct waves in Crisco, which only suggest moderate Q values of ~15–50 (Wong and Lines, 2013).

Another rarely noted limitation of the Q model is in its disagreement with poroelasticity (Biot, 1956). As shown in Chapters 3 and 4, the frictional stress field in a poroelastic medium is proportional to filtration velocities, whereas in order to be described by a Q, the stress must be proportional to the strain and/or strain rate. However, poroelastic effects should likely play some role in the behavior of fluid-saturated and bitumen-rich rocks. All this suggests that the physics of wave attenuation in Crisco (and therefore likely in heavy oils) does not easily reduce to the Q-type phenomenology.

Here, I try explaining the disagreements in Crisco experiments mentioned above by testing a broader model of nonlinear viscosity and elasticity. In this model, there is no unique *Q* parameter, and this parameter is also not needed for modeling wave attenuation effects. The observed frequency dependences of the wave *Q*s and effective moduli are explained by the dependences of the viscosities and elastic constants on strains and strain rates within the wave. This model is therefore fully consistent with mechanics and thermodynamics. I show how this model explains all experiments with both unaltered and altered Crisco (Wong and Lines, 2013) and constrains several physical parameters of this medium.

5.3 Method

Similar to fluids, solids possess viscosity (Chapter 3). This property means that in a deformed body, there exist stresses dependent on the strain rate (Landau and Lifshitz, 1986). In a Newtonian solid, the stress-strain relation contains two parts: 1) the elastic stress-relation (Hooke's law):

$$\sigma_{ij}^{\mathrm{el}} = \lambda \frac{\partial u_k}{\partial x_k} \delta_{ij} + \mu \left(\frac{\partial u_i}{\partial x_j} + \frac{\partial u_j}{\partial x_i} \right), \tag{5.1}$$

and 2) viscous stress with a similar dependence on strain rates (Naviér-Stokes law):

$$\sigma_{ij}^{\mathrm{visc}} = \eta_\lambda \frac{\partial \dot{u}_k}{\partial x_k} \delta_{ij} + \eta_\mu \left(\frac{\partial \dot{u}_i}{\partial x_j} + \frac{\partial \dot{u}_j}{\partial x_i} \right) \tag{5.2}$$

In equations (5.1) and (5.2), u_i, is the displacement λ and μ are the Lamé constants. Parameters η_λ and η_μ are analogous to μ and λ and represent the 'dynamic' (ordinary, or shear) and 'second' viscosities, respectively. The combined stress laws (5.1) and (5.2) describe the medium known as the Voigt solid (Kolsky, 1963). This is the simplest model of viscous friction within an isotropic solid without knowledge or assumptions about its internal

structure (Landau and Lifshitz, 1986).

Substitution of stresses (5.1) and (5.2) in the second Newton's law gives the equation of motion for the Voigt solid:

$$\rho \ddot{u}_i = \left(\sigma_{ij}^{\mathrm{el}} + \sigma_{ij}^{\mathrm{visc}} \right)_{,j} + f_i \ . \tag{5.3}$$

Equations (5.1) – (5.3) describe wave propagation in linear anelastic media. In the derivation of these equations, no notions of "relaxation mechanisms" or characteristic frequencies or time constants are used, and only rigorous principles of physics are followed.

For constant (λ, μ) and (η_λ, η_μ), equations (5.1) and (5.2) are linear with respect to the deformation magnitude. Heavy oils, however, are most likely non-Newtonian fluids, and bitumen-rich rocks may also exhibit nonlinear elastic properties, especially in the near-source regions of strong amplitudes. Minster et al. (1991) considered such nonlinear effects on the near-source attenuation, by assuming a dependence of the material Q on the strain. Coulman et al. (2013) proposed a power-law nonlinear viscosity for modeling the observed frequency-dependent Q spectra measured in lab experiments. In the GLS approach, the nonlinearity arises naturally by noting that the elastic parameters λ and μ can depend on the strain, and parameters η_λ and η_μ in (5.2) can depend on both the strain and strain rate. In particular, all observations by Wong and Lines (2013) can be explained by allowing different values of material constants λ, μ, η_λ and η_μ for low and high levels of strain, separated by some strain threshold ε_0. Such dependences can be modeled by using a sigmoid function $S(x) = \left[1 + \exp(-6x)\right]^{-1}$ (Figure 5.1):

$$p(x) = p_{\mathrm{low}} + \left(p_{\mathrm{high}} - p_{\mathrm{low}} \right) S\left(\frac{|\varepsilon|}{\varepsilon_0} - 1 \right), \tag{5.4}$$

where ε_0 is the strain level at which the transition from p_{low} to p_{high} occurs, and parameter p

represents either the modulus or viscosity in this expression. For simplicity, for viscosity parameters η_λ and η_μ, I only consider dependences on the combined strain and strain-rate magnitude, defined by $\tilde{\varepsilon} \equiv \sqrt{(\dot{\varepsilon}\tau)^2 + \varepsilon^2}$. Note that the time constant τ can be interpreted as a "relaxation time" or its inverse 1/t represents the "reference" or "characteristic frequency" that are commonly assumed in *Q*-based models of Earth's materials (e.g. Liu et al., 1976). This constant needs to be measured in experiments with variable strain and strain rates. In the absence of such experiments, I (arbitrarily) take τ equal 1 μs in the numerical examples below.

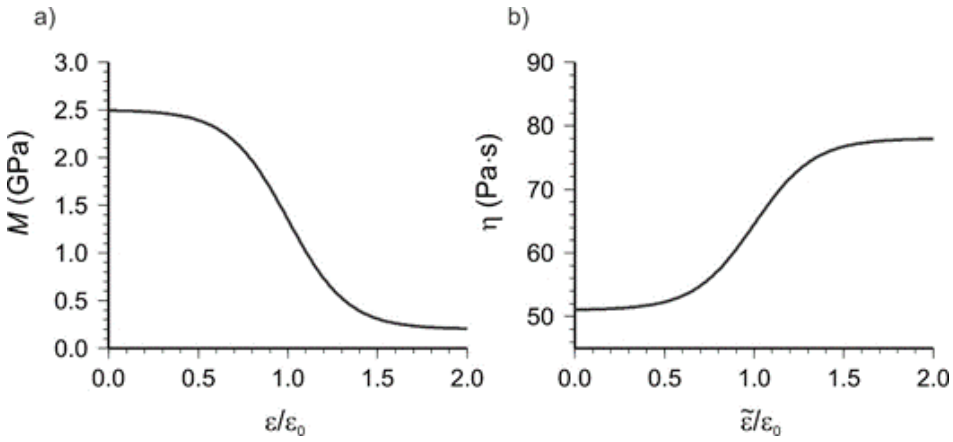

Figure 5.1. Schematic nonlinear strain-dependent model for unaltered Crisco: a) Strain dependence of the P-wave modulus *M*; b) Dependence of P-wave viscosity η on the combined strain and strain-rate magnitude.

5.4 Numerical Modeling

Let us consider propagation of a *P* wave in Crisco based on laboratory measurements by Wong and Lines (2013). For *P* waves, the elastic constants in eqs. (5.1) and (5.2) are combined into the P-wave modulus $M = \lambda + 2\mu$ and the corresponding P-wave viscosity $\eta = \eta_\lambda + 2\eta_\mu$. As discussed in detail by Morozov et al. (in preparation), the observations for unaltered and altered Crisco can be explained by the following values of these material

parameters:

1) For unaltered Crisco, the strain-dependent modulus M ranges from 0.2 GPa for high strains to 2.5 GPa for low strains. The strain-dependent viscosity η varies from 51 Pa·s for low strains to 78 Pa·s for high strains (Figure 5.1).
2) For altered Crisco, the modulus M ranges from 2.09 GPa for high strains to 2.32 GPa for low strains. The viscosity η varies from 16 Pa·s for low strains to 39 Pa·s for high strains.

The time-domain differential equations (5.1) – (5.3) can be readily implemented in a 1-D finite-difference algorithm (Appendix A). The source is modelled as a zero-phase Ricker wavelet with dominant frequency 800 kHz. Because of the nonlinearity a high η/M ratio near the source, the peak frequency drops within about two wavelengths, after which the peak frequencies drop to ~500 kHz and ~250 kHz for the altered- and unaltered-Crisco respectively. These frequencies are close to those observed for direct waves and reflections (Wong and Lines, 2013).

Figure 5.2 compares the direct-wave waveforms modeled in unaltered and altered Crisco. Note that the waves decay in amplitudes and have dispersive shapes. Interestingly, the shapes of the "far-field" waveforms are strongly different in these two cases. The waveform in altered Crisco is similar to the zero-phase source wavelet, whereas the waveform in unaltered Crisco is strongly phase-rotated. This rotation occurs within a thin near-source zone of very high nonlinear attenuation. This zone extends to ~1–2 wavelengths (several millimeters) from the source or water-Crisco boundary, after which the strain drops and the propagation and attenuation become linear and correspond to the low-strain regime (Figure 5.1).

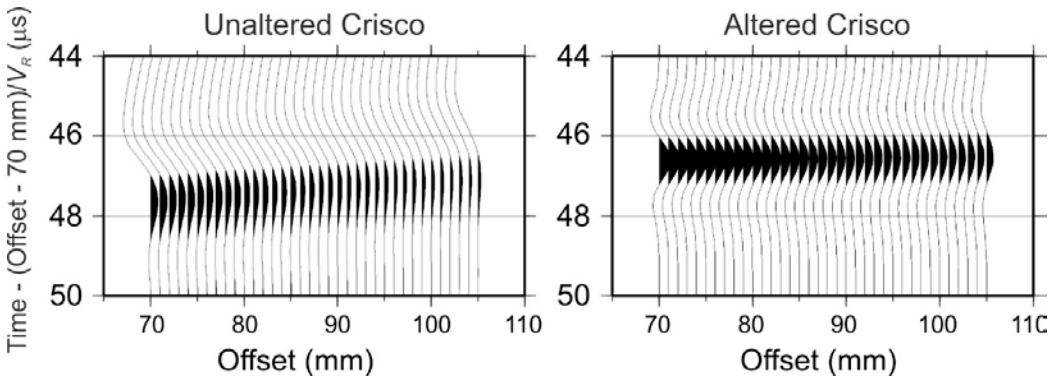

Figure 5.2. Direct-wave waveforms in unaltered and altered Crisco simulated by finite-difference modeling. Linear travel-time moveout with velocity V_R = 1540 m/s is removed.

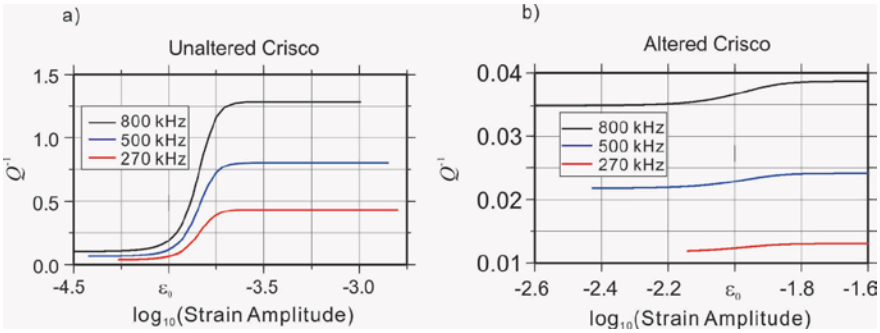

Figure 5.3. Frequency and strain-dependent nonlinear attenuation. a) Q^{-1} spectrum of unaltered Crisco with $\varepsilon_0 = 10^{-4}$; b) Q^{-1} spectrum of altered Crisco with $\varepsilon_0 = 10^{-2}$.

Figure 5.3 shows the attenuation rates (Q^{-1}) as functions of strain amplitudes, for harmonic waves modeled in unaltered and altered Crisco at three different frequencies. When strains are high, $\varepsilon > \varepsilon_0$, the levels of Q^{-1} are also high and show strong variation with frequency. For low strains $\varepsilon < \varepsilon_0$, Q^{-1} is much lower. This is the far-field regime. In this regime, the Q^{-1} values of both unaltered and altered Crisco are similar (Figure 5.3).

In the near field, the harmonic-wave attenuation in unaltered Crisco at 800 kHz is ~30–40 times higher than that in altered Crisco and corresponds to $Q \approx 0.8$. This ultra-low Q is an apparent property of the wave (Morozov and Baharvand Ahmadi, 2015), which simply describes a very rapid decay of the amplitude, a drop in the peak frequency, and a phase rotation within the near-source zone. These effects result in the observed much lower

amplitudes and dominant frequencies in the “far field” in Wong and Lines (2013).

Figure 5.4 compares reflections from three different interfaces, which are also very close to those observed experimentally by Wong and Lines (2013). The particle displacements of the reflections from a water-unaltered Crisco contact are almost the same in magnitude but of opposite polarity compared to those from aluminum (Figure 5.4). This opposite polarity is caused by the very low elastic modulus of the thin boundary of the unaltered Crisco ($M \approx 0.2$GPa at high strain). Therefore, the nonlinear modulus here dominates the reflectivity. However, the viscosity difference also contributes to the wavelet shape variations (red line in Figure 5.4).

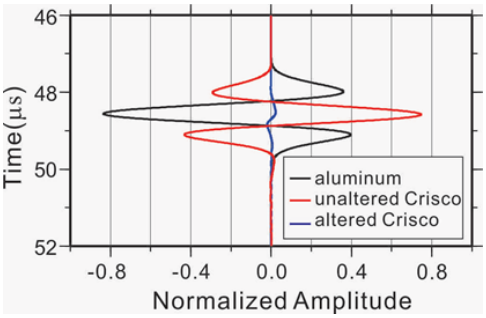

Figure 5.4. Displacement seismograms modeled for different media in contact with water. Black line shows a reflection from the water-aluminum contact, red line is a reflection from water-unaltered Crisco contact, and blue line shows a reflection from water-altered Crisco contact.

The altered Crisco has a weak (interpreted) variation of the modulus (from 2.09 to 2.32 GPa), which is very close to that of water. The model shows small-amplitude reflections from the water vs altered-Crisco contact (blue line in Figure 5.4). Unlike the reflection from water *vs* unaltered-Crisco contact, the reflection from altered Crisco shows a nearly 90° phase shift (blue line in Figure 5.4). Such phase-rotated reflection is controlled by the viscosity contrast. Note that similarly to altered Crisco, strong nonlinear viscosity causes phase-rotated direct waves in unaltered Crisco (Figure 5.2).

5.5 Discussion

The modeling described above successfully explains all three key observations with unaltered and altered Crisco by Wong and Lines (2013): 1) the amplitudes and attenuation of the direct waves, 2) reduction of dominant frequencies; and 3) strong and phase-shifted reflections in water. Thus, the physical, nonlinear viscosity-based approach provides us a greatly improved understanding of heavy-oil-like media.

The substantial advance in the theory of wave propagation and the ability to model the experiments in much greater detail than done by Wong and Lines (2013) also reveals additional questions. The proposed model suggests that acoustic wave propagation in Crisco (and particularly in unaltered Crisco) is highly nonlinear near the source and near the water-Crisco reflecting boundaries. However, the experiments by Wong and Lines (2013) did not explore this nonlinearity, and consequently I have no opportunity to test this hypothesis and to verify the estimates of parameters ε_0, τ, and the selected nonlinearity function (5.4). Thus, additional experiments addressing such nonlinearity are required. Also, both modeling in this Chapter and lab experiments (Wong and Lines, 2013) were conducted at ultrasonic frequencies. Because of the (inferred) nonlinearity, and also because of strong attenuation and dispersion of waves in viscous media, transferring these results to exploration seismic frequencies can be highly challenging. Further research of this subject is also definitely required.

5.7 Conclusions

Recent laboratory observations of acoustic wave propagation and reflectivity in a proxy for heavy oil (Crisco; Wong and Lines, 2013) can be explained by nonlinear elasticity and viscosity. The nonlinearity concentrates in a narrow range of about 1-2 wavelengths

(several millimeters at the ultrasonic frequencies used) near the source, where high strains ($\varepsilon > \varepsilon_0$) occur. The attenuation rate within this zone can be very high, causing a drop in the amplitude and peak frequency of the signal, and a phase rotation of the wavelet. Beyond this nonlinear range, the attenuation rate decreases, and wave propagation becomes linear. Modeling of reflections indicates that reflectivity from unaltered and altered (melted and re-solidified) Crisco in water occur differently. The strong negative reflections observed from unaltered Crisco are mainly due to the nonlinear reduction of the elastic modulus under high strain. For altered Crisco, the reflectivity is phase-rotated and principally explained by a contrast in viscosity.

CHAPTER 6

TRADE-OFF OF ELASTIC STRUCTURE AND Q IN INTERPRETATIONS OF SEISMIC ATTENUATION

Up to this point, I discussed several physics-based forward models allowing us to predict frequency-dependent *Q* for waves in uniform media. Broadly, these were models for "intrinsic *Q*" (Chapter 2). In Chapter 5, one of the estimates of this *Q* was performed by using phase-shifted reflections. In this Chapter, I further consider such measurements of *Q* below reflectors and show that it is very close (in fact, may be completely equivalent) to the "scattering *Q*", or "fluctuation *Q*" produced by sub-wavelength layering below or above the reflector. The presentation in this Chapter is based on the following paper:

***Deng, W.**, and I. B. Morozov. Trade-off of elastic structure and Q in interpretations of seismic attenuation, Pure and Applied Geophysics, doi: 10.1007/s00024-017-1581-3.*

6.1 Abstract

The quality factor *Q* is an important phenomenological parameter measured from seismic or laboratory seismic data and representing wave-energy dissipation rate. However, several types of *Q*s exist, depending on the types of measurements and models or assumptions about the elastic structure. I consider three general types of elastic structures that are commonly encountered in seismology: 1) shapes and dimensions of rock specimens in laboratory studies, 2) geometric spreading or scattering in body-, surface- and coda-wave

studies, and 3) reflectivity on fine layering in reflection seismic studies. For each of these types, the measured Q strongly trades off with the (inherently limited) knowledge about the elastic structure. For the third of the above types, the trade-off is examined quantitatively in this paper. For a layered sequence of reflectors (e.g., an oil or gas reservoir or a hydrothermal zone), reflection amplitudes and phases vary with frequency, which is analogous to a reflection from a contrast in attenuation. I demonstrate a quantitative equivalence between phase-shifted reflections from anelastic zones and reflections from elastic layering. Reflections from the top of an elastic layer followed by weaker reflections from its bottom can appear as resulting from a low Q within or above this layer. This apparent Q can be frequency-independent or have a practically arbitrary frequency dependence corresponding to the pattern of thin layering. Depending on the layering, the interpreted Q can be positive or negative, and it can depend on source-receiver offsets. Therefore, estimating Q values from frequency-dependent or phase-shifted reflection amplitudes always requires additional geologic or rock-physics constraints, such as sparseness and/or randomness of reflectors, absence of attenuation in certain layers, or specific physical mechanisms of attenuation. Similar conclusions about the necessity of extremely detailed models of the elastic structure apply to other types of Q measurements.

6.2. Introduction

Seismic waves are affected by energy dissipation and waveform (or velocity) dispersion, which are caused by the complexities of the real Earth compared to the idealized elastic media for which most wave equations are usually written. Such complexities, for example, include granularity, fracturing, presence of fluids within porous rocks, media with effective solid viscosity (Chapter 4), and heterogeneity at scales smaller than about ¼ of the

dominant wavelength used for seismic imaging. Waves in such complex media are characterized by attenuation of wave amplitudes and phase distortions, and it is therefore important to determine what type of information about subsurface complexities can be recovered from the wavefield recorded at the surface or in a borehole.

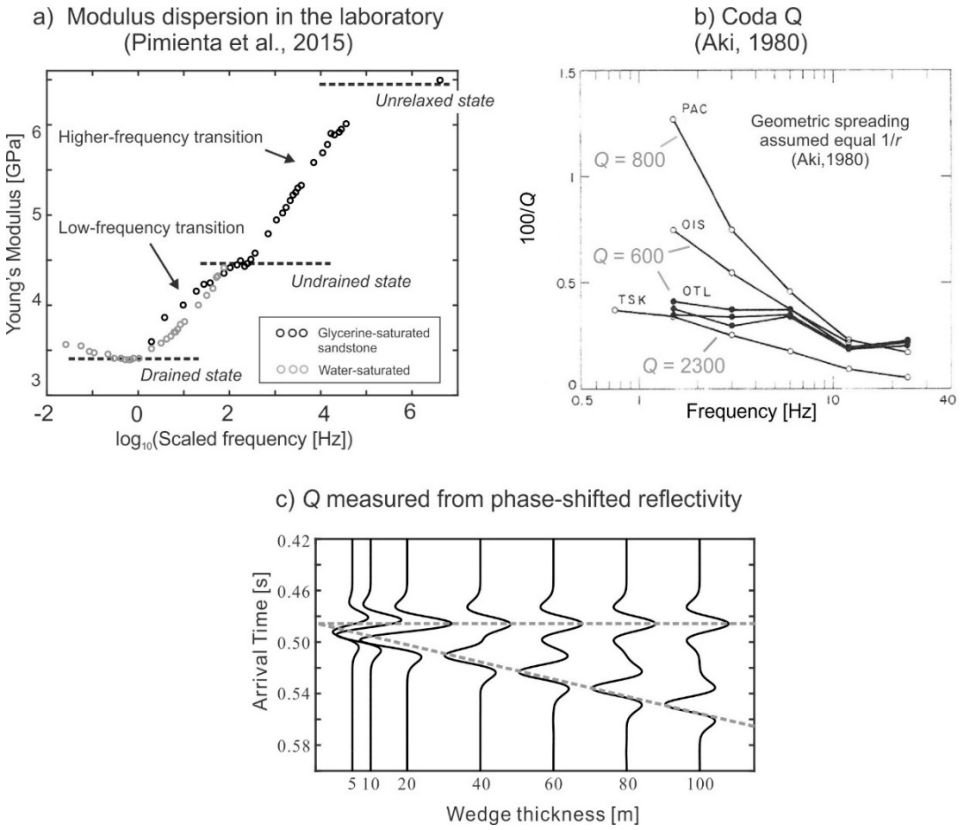

Figure 6.1. Illustrations of trade-off with assumed elastic structures in three types of Q measurements:

(a) Low-frequency laboratory measurements of Young's-modulus dispersion in sandstone (Pimienta et al., 2015a). Frequency values are scaled as $f_{\text{scaled}} = f\frac{\eta}{\eta_0}$, where η is the viscosity of pore fluid and $\eta_0 = 1$ Poise. Three states of the system are identified by low dispersion rates (dashed lines), between which the low-frequency and higher-frequency transitions occur (labeled). These transitions are also characterized by peaks in Q^{-1} (not shown).

(b) Observation of strongly frequency-dependent coda Q (Aki, 1980). Gray labels indicate alternate values of Q obtained after removing the assumption of $1/r$ geometric spreading (Morozov, 2010).

(c) Synthetic reflections of a Ricker wavelet in a wedge model. Dashed lines indicate the boundaries of the wedge. The waveforms at wedge thickness below or equal 20 m can be interpreted as phase-shifted reflections from a low-Q zone.

The mechanisms of attenuation are often poorly known, and their effects on seismic records overlap. The combined action of these mechanisms is usually described by a phenomenological quantity denoted Q (quality factor). The Q can be measured by various classical (Tonn, 1991) and newer methods, such as based on stress-strain ratios in low-frequency laboratory testing (Jackson and Paterson 1993; Lakes 2009), several groups of coda-based methods arising from the model by Aki and Chouet (1975), and many methods for body waves, such as spectral ratios (White 1992), central-frequency shifts (Quan and Harris, 1997), peak-frequency shifts (Zhang and Ulrych, 2002), or logarithmic spectral-area differences (Wang et al., 2015). Many of these methods measure the variations of the frequency spectrum with time or amplitude variations with distance at constant frequencies, both of which are expressed through Q-factors. Coming almost directly from measurements combined with only simple models, the Qs resulting from these procedures represent *apparent* quantities (Morozov and Baharvand Ahmadi, 2015). A very difficult task is therefore to determine whether and how these apparent Qs may depend on the measurement procedures and model assumptions, and what parts of them belong to the Earth' materials and structure.

For most if not all types of attenuation measurements, highly detailed knowledge of the underlying elastic structure is required before a reasonably accurate (and particularly frequency-dependent) estimate of Q can be made. Three illustrations of this requirement from different areas of seismology are shown in Figure 6.1. First, in low-frequency laboratory measurements with rock specimens, it is usually assumed that the observed strain-stress phase lags relate to the material's Q-factor as $\tan\phi = Q^{-1}$ (e.g., Jackson and Paterson, 1993; Lakes, 2009). However, recent measurements of extensional- and bulk-mode

deformations of sandstone show that a relation of $\tan\phi$ to material properties is not so direct. For example, Pimienta et al. (2015) reported an interesting low-frequency peak in $\tan\phi$ and the corresponding dispersion interval for bulk and Young's moduli (Figure 6.1a). These authors modeled these low-frequency effects by a Zener (Standard Linear, or SLS) solid and explained them by a transition from a "drained" specimen (when the pore-fluid flow penetrates the whole specimen) to its "undrained" state (when the pore-fluid occupies only a small part of it; dashed lines in Figure 6.1a). For the present discussion, it is most important that the low-frequency transition (Figure 6.1a) is primarily due to the design of the experiment: the relatively small (8-cm) specimen with ends open for pore-fluid flow and substantial dead volumes containing the saturating fluid in the apparatus (Pimienta et al. 2016). Therefore, this transition is apparent and represents a response of the measurement apparatus that should not be directly attributed to sandstone. In order to obtain the properties of the material, this transition should be accounted for along with other experimental corrections (Pimienta et al. 2015a, b); however, this is impossible to do without an accurate physical model within the rest of the frequency spectrum (Figure 6.1a).

In the second example, Figure 6.1b shows well-known coda Q measurements in several areas of the world by Aki (1980). Note the values of Q ranging from about 75 to 2000 and varying by 2 to 6 times across the 0.8- to 18-Hz frequency band. Nevertheless, this strong variation with frequency is only obtained when the distance dependence of geometric spreading is assumed to equal exactly $1/r$ (Figure 6.1b). This dependence corresponds to straight rays in a uniform space without velocity gradients and boundaries, which is unrealistic, particularly in areas of active tectonics in which these data were collected. The Q produced by this oversimplified model (Figure 6.1b) is therefore also apparent. Analogously

to the apparent resistivity commonly used in electrical imaging (Spies and Eggers, 1986), the apparent $Q(f)$ dependence in Figure 6.1b represents only a conventional way to plot experimental readings rather than a true property of the subsurface. By relaxing the $1/r$ assumption, the interpretation changes significantly: the Q becomes nearly frequency-independent and takes on only three and much larger values of about 600, 800, and 2300 (Morozov, 2010; labels in Figure 6.1b).

The third illustration of the sensitivity of Q to the underlying elastic models and assumptions relates to measurements of Q from seismic reflections. The VE theory (e.g., Aki and Richards, 2002) and also the more rigorous theory described in Chapter 5) predict that a low-Q zone within the subsurface should lead to phase-shifted reflections. Lines et al. (2008, 2014) and Han et al. (2015) suggested that such reflections can potentially be used for identifying oil and gas reservoirs in seismic sections. Leaving aside all (difficult) practical issues of noise and resolution, let us consider whether this Q would be apparent or real. A comparison with the standard wedge model (Figure 6.1c; Gochioco, 1991) indicates an apparent character of this Q as well. As shown in Figure 6.1c, two reflections that are separable in the thicker part of the wedge become inseparable with the thickness of the wedge decreasing below $\lambda/4$ ($\leq$ 20 m in Figure 6.1c). The waveform reflected from the thin edge of the wedge looks like a phase-shifted reflection that could be interpreted as a reflection from a low-Q zone (Lines et al. 2014). Nevertheless, the model is purely elastic, and therefore to infer a true Q with certainty, we have to know the structure of elastic layering down to sub-$\lambda/4$ detail and to relative magnitudes of about $1/Q$.

In this paper, I consider the third of the above examples in detail. I compare two types of attenuation mechanisms: 1) viscoelastic internal friction characterised by a Q,

and 2) elastic attenuation caused by thin layering within an elastic medium (O'Doherty and Anstey 1971; White et al. 1975). Reflections from the top and bottom of a layer of less than quarter-wavelength thickness are generally inseparable and look like a phase-shifted single reflection in a seismogram (Figure 6.1c). The peak frequency and phase of this reflection are shifted, and both its amplitude and phase are frequency-dependent. At the same time, such phase shifts and frequency dependences are also characteristic for reflections from contrasts in attenuation, and a Q value can be inverted for below this reflector (Lines et al., 2008, 2014; Han et al., 2015). As shown below, this Q would typically be frequency-dependent. Thus, there exists a fundamental equivalence between reflection seismic responses from thin layering and those from attenuation contrasts within the Earth. In order to constrain the true Q required for petrophysical interpretation, the elastic structure needs to be understood in great detail. As shown in this paper, the uncertainty of a Q measured from reflection data is so great that in an end-member approach, Q^{-1} can always be set equal zero and replaced with sub-wavelength scale elastic layering. This situation is similar to other types of attenuation measurements, where detailed structural and geometric-spreading models and/or rock-physics mechanisms are required (Figures 6.1a and 1b).

The structure of the Chapter is as follows. In section 6.3, I model the amplitude and phase responses produced by a thin layer and a single attenuative reflector. Based on these models, in section 6.4, I show that reflections from Q contrasts can *always* be accurately modeled as reflections from layered elastic sequences and vice versa. Quantitative relations between the thickness of the layer and the apparent Q (or conversely, between the true Q and the apparent thicknesses of the equivalent elastic layering) are obtained. These relations provide guidance for thin-layer detection and identification of attenuative layers. In

section 6.5, I discuss some combinations of observations and additional geologic and rock-physics data that may make it possible to distinguish between finely-layered structures and attenuative reflectors.

6.3. Method

To analyze the frequency-dependent reflection amplitudes and phase variations, I construct two simple models (Figure 6.2). Model I consists of three purely elastic layers, the middle one of which is considered as thin (Figure 6.2a), and Model II (Figure 6.2b) is composed of only two layers, one of which may contain a low Q. For both of these models, incident and reflected waves are modeled within the upper layer. The analysis is carried out in the frequency domain by considering a plane wave at frequency f normally incident on the boundaries (Figure 6.2). The corresponding waveforms in the time domain are obtained by inverse Fourier transforms using the Ricker wavelet as the source wavelet.

In the layered model Model I (Figure 6.2a), let us denote the acoustic impedances of the layers Z_1, Z_2 and Z_3. Because reflection coefficients only depend on ratios of impedances, the units of impedance can be selected so that $Z_1 = 1$, and Z_2 and Z_3 become the relative impedances between layers. Let us further consider two different structures: structure 1 with

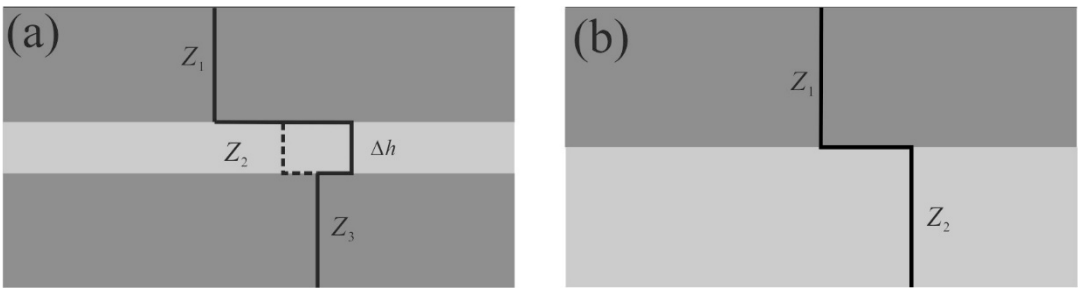

Figure 6.2. Layered models considered in this chapter: (a) Elastic Model I with a thin layer (b) Model II with attenuation present in either upper or lower layer. Quantity Δh is the thickness of the thin layer (shorter than a quarter of the wavelength), and Z_i denote the acoustic impedances of i-th layers.6.3.1 Layered Structure

$Z_1 < Z_2 > Z_3$ and structure 2 with $Z_1 < Z_2 < Z_3$ (Table 6.1). The thickness of the thin layer is denoted Δh, which can also be viewed as unit distance in the models. The two-way travel time (TWTT) through the middle layer Δt is then related to the wave period T, Δh, and the wavelength λ within it as $\Delta t/T = 2\pi f \Delta t = 2\Delta h/\lambda$. Only these relative quantities determine the reflected waveforms (Table 6.1).

Table 6.1. Parameters for the models in Figure 6.2

	Layer	Impedance	Q
Model I	Z_1	1.00	∞
	Z_2	1.17 (structure 1) or 1.10 (structure 2)	∞
	Z_3	1.11	∞
Model II	Z^*_1	1.00	10, 30, 100, or ∞
	Z^*_2	1.05	10, 30, 100, or ∞

The reflectivity of each boundary in Model I (Figure 6.2a) equals:

$$r_n = \frac{Z_{n+1} - Z_n}{Z_{n+1} + Z_n}. \tag{6.1}$$

The reflection amplitude received by the geophones at the surface can be written as $u(f) = r(f)\exp(-i2\pi f \Delta t_1)$, where $r(f)$ is the refection amplitude at the upper boundary, and $\exp(-i2\pi f \Delta t_1)$ is the phase shift due to the wave-propagation time Δt_1 above this boundary. As everywhere in this dissertation, I follow the sign convention commonly used in wave mechanics (Aki and Richards 2002; Deng and Morozov 2016), in which the complex-valued wave is defined as $u(x,t) = A\exp(-i\omega t + ikx)$, where ω is the angular frequency and k is the wavenumber. The common phase shift due to Δt_1 is insignificant for the present problem, and $r(f)$ consists of a reflection from the top middle layer, with amplitude $r_{top} = r_1$, and a phase-shifted reflection from its bottom, with amplitude $r_{bottom} = (1 - r_1^2) r_2$:

$$r\left(\bar{f}\right)=\left[r_{top}+r_{bottom}\exp\left(-i2\pi\bar{f}\right)\right], \tag{6.2}$$

where $\bar{f}=f\Delta t=2\Delta h/\lambda$ is the non-dimensional frequency. For simplicity, I do not consider multiples and reflections from the outer boundaries of the layers.

From eq. (6.2), the amplitude and phase of the reflection coefficient from the middle layer equal:

$$A\left(\bar{f}\right)=\left|r\left(\bar{f}\right)\right| \ ,\phi\left(\bar{f}\right)=-\arctan\left[\frac{\xi\sin\left(2\pi\bar{f}\right)}{1+\xi\cos\left(2\pi\bar{f}\right)}\right], \tag{6.3}$$

where $\xi\equiv r_{bottom}/r_{top}$ is the ratio of the reflectivities at its boundaries. Considering a "thin" middle layer with $\Delta h/\lambda$ ranging from 0 to 0.25 (i.e., $\bar{f}$ ranging from 0 to 0.5), these dependences of $A\left(\bar{f}\right)$ and $\phi\left(\bar{f}\right)$ are shown in Figure 6.3. For structure 1 (Table 6.1), the amplitude increases with frequency (Figure 6.3a). The phase shift equals zero at the ends of this interval and shows a peak of about 20º near $\Delta h/\lambda\approx 0.1$ (Figure 6.3a). By contrast, for structure 2, the reflectivity amplitude monotonously decreases with frequency by about 20%,

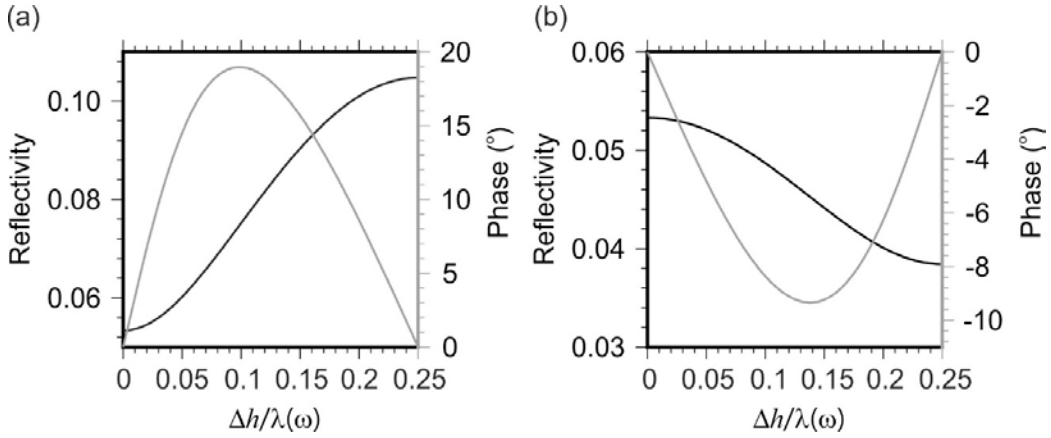

Figure 6.3. Amplitude (black lines) and phase (gray) of complex-valued reflectivity in layered model (Figure 6.2a) as function of the ratio between the thickness of the thin layer and the wavelength ($\Delta h/\lambda$): (a) the case of high-impedance thin layer (structure 1; $Z_1 < Z_2 > Z_3$); (b) progressive increase in the impedances (structure 2; $Z_1 < Z_2 < Z_3$).

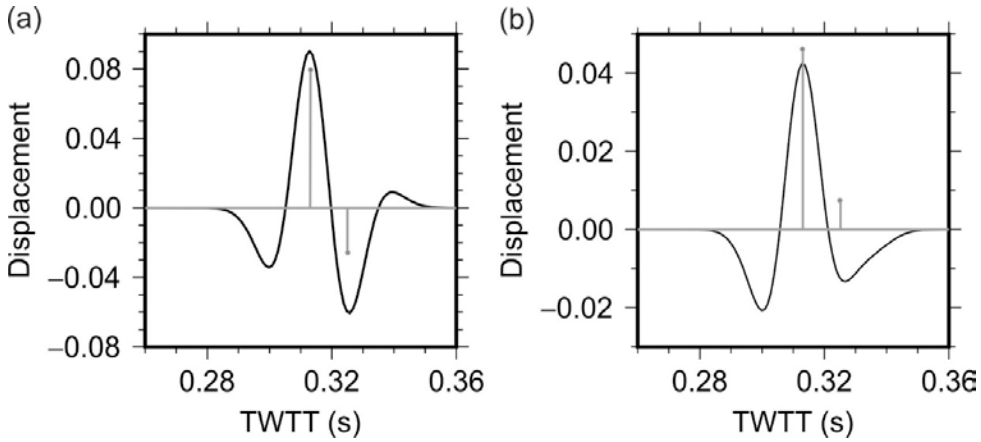

Figure 6.4. Reflected waveforms for a 30-Hz Ricker wavelet incident on the thin layer in Model I: (a) structure 1 between the impedances ($Z_1 < Z_2 > Z_3$) and (b) structure 2 ($Z_1 < Z_2 < Z_3$). Vertical gray bars show the individual reflection coefficients of the upper and lower interfaces (r_{top} and r_{bottom} in eq. (6.2)).

and the phase has a negative peak of about -10° near $\Delta h/\lambda \approx 0.14$ (Figure 6.3b). Note that in these examples (Table 6.1), I only illustrate the basic effect of dispersion $r\left(\overline{f}\right)$ and do not explore its dependence on ξ.

To examine the time-domain response of this layered structure, I use relation (6.1) to construct the reflected seismogram for a 30-Hz Ricker wavelet (Ricker, 1953). The thickness of the thin layer is chosen equal 20 m, which is approximately a quarter of the dominant wavelength. The reflected waveforms for the two model types are shown in Figure 6.4. For structures 1 and 2, the two reflections from the top and bottom of the thin layer (gray bars in Figure 6.4) are merged into single reflections that are phase-rotated in opposite directions. For both structures, the Ricker wavelets reflected from the top and bottom of the thin layer overlap for over 75% of their durations and cannot be separated without a priori knowledge of the structure. The phase shifts are positive for structure 1 and negative for structure 2 (Figure 6.4), and they can be measured by various methods, such as complex spectral decomposition (Bonar and Sacchi, 2010). As shown in the next subsection, similar waveforms would be obtained in reflections from an anelastic medium (with lower layer

assumed to be anelastic) with a negative and positive Q, respectively.

6.3.2 Viscoacoustic Reflector

Seismic attenuation within the layers is another factor that could cause variations in reflection phases and amplitudes. According to the viscoelastic model of attenuation, the impedance for a medium is obtained as (Aki and Richards, 2002):

$$Z^*(f) = Z(f)\left[1 - \frac{i}{2Q}\right], \tag{6.4}$$

where $Z(f) = \rho V(f)$, $V(f)$ is the phase velocity of the wave, ρ is the density, and Q is the seismic quality factor. As it is often done, let us assume that Q is constant across the seismic frequency band and the frequency-dependent $V(f)$ is given by Kjartansson's (1979) dispersion law:

$$V(f) = V_0 \bar{f}^{\frac{1}{\pi Q}}, \tag{6.5}$$

where $\bar{f} = f / f_0$ is a non-dimensional scaled frequency, f_0 is some reference frequency, and V_0 is the phase velocity at $f = f_0$. Thus, similar to the layered case (Model I), attenuative-media models also contain inherent characteristic frequencies.

Let us consider the single-boundary Model II (Figure 6.2b), assuming that the upper layer is elastic ($Q^{-1} = 0$) and the lower one is anelastic with a finite Q. The frequency-dependent reflectivity (6.1) at the boundary becomes (again recalling our selection of units $Z_1 = 1$):

$$r^*(f) = \frac{Z_{02}\zeta - 1}{Z_{02}\zeta + 1}, \text{ where } \zeta \equiv \bar{f}^{\frac{1}{\pi Q}}\left(1 - \frac{i}{2Q}\right), \tag{6.6}$$

and Z_2 is the relative impedance of the second layer at the reference frequency. Similarly to the thin-layer case in the preceding section, the attenuation and phase-shift properties of this

model are determined by the non-dimensional frequency $\overline{f}$.

With Model II parameters given in Table 6.1, the modulus and phase of this complex reflectivity are shown in Figures 6.5a and b, respectively. The selection of reference frequency f_0 is consequential for the results, and in this example, I chose it equal to the dominant frequency of the signal (30 Hz) (Morozov et al., in revision, *Geophysics*). With this selection for f_0, with Q = 30 or 100, the amplitude continuously increases with frequency, but with Q = 10, the reflectivity also sharply rises toward zero frequency (solid black line, Figure 6.5a). With decreasing Q, the increase of reflection amplitude with frequency becomes stronger. These variations of reflection amplitudes are due to combined effects of velocity dispersion and Q, both of which effectively increase the impedance of the lower medium.

With regard to the phase response, when Q approaches infinity (lower layer is almost elastic), the complex-valued reflectivity becomes

$$\lim_{Q\to\infty} r^*(f) = \frac{Z_2 - 1}{Z_2 + 1}\ , \tag{6.7}$$

which means that the phase shift equals zero when $Z_2 > 1$ and ±180° when $Z_2 < 1$. The phase

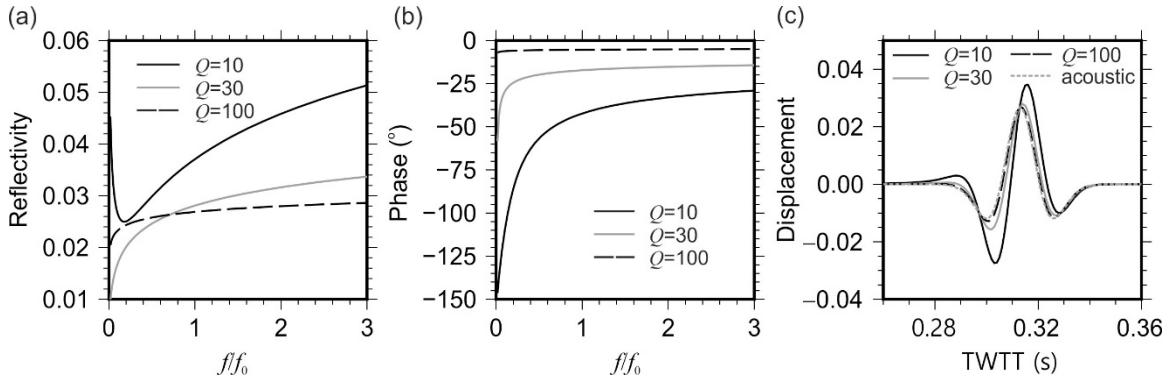

Figure 6.5. Reflections from an attenuative half-space (Model II). The lower layer is anelastic, the upper layer is elastic: (a) amplitude response; (b) phase response; (c) reflection waveforms. The reference frequency f_0 is 30 Hz.

and amplitude variations are strong when Q is low (for example, Q = 10 shown by black line in Figure 6.5). The negative phase shifts reduce with increasing frequencies. With Q = 100, the phase variations are within −10º and remain near constant (dashed lines in Figure 6.5b).

Considering time-domain reflections, if no inelastic effects are considered for Model II (Table 6.1), the reflection would be a zero-phase Ricker wavelet with amplitude equal about 0.03. In the presence of attenuation, the reflected waveform is close to a negatively phase-rotated Ricker wavelet with increased amplitude (Figure 6.5c). The stronger the attenuation, the more significant is the phase rotation. The interpreted amplitudes of reflections increase with increasing attenuation. For example, with Q = 10, the peak amplitude increases by about 20% (Figure 6.5c).

It is also interesting to consider the case when the upper layer is anelastic with attenuation Q^{-1} and phase-velocity dispersion $V(f)$ while the lower layer is elastic and non-dispersive. In this case, the impedance of the upper layer equals ζ, and similar to eq. (6.6), the reflected amplitude measured from surface observations is:

$$r^*(f) = \frac{Z_2 - \zeta}{Z_2 + \zeta} \ . \tag{6.8}$$

The frequency-dependent reflectivity and phase for this case are shown in Figures 6.6a and b. Similar to the results in Figure 6.5, with increasing Q, the intensities of reflectivity and phase variations are reduced. For Q = 10, the phase performs an over 360° rotation near frequency $f/f_0 \approx 1.8$. Figure 6.6c shows the time-domain reflectivity for a 30-Hz Ricker wavelet obtained by applying relation (6.8).

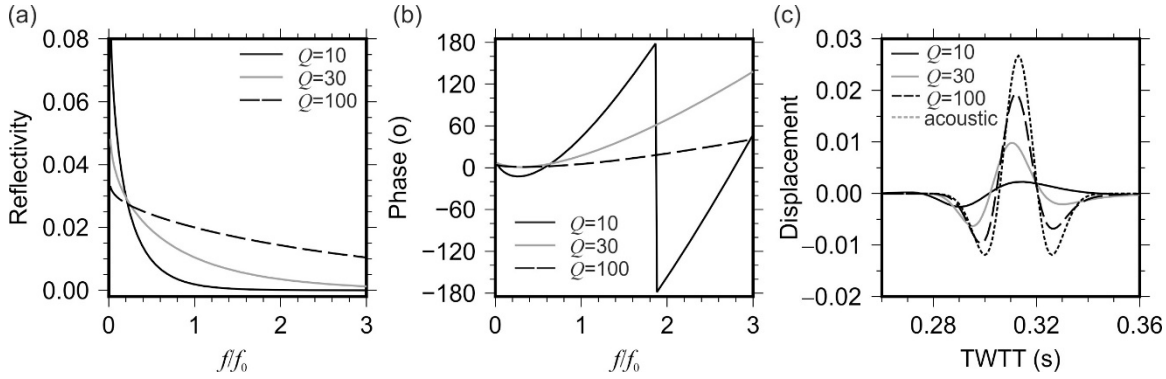

Figure 6.6. Reflections from the boundary in Model II in which the lower layer is elastic and the upper layer is anelastic: (a) amplitude response; (b) phase response; (c) reflection waveforms. The reference frequency f_0 is 30 Hz.

6.4. Equivalence of Layered and Anelastic Reflectors

Figures 6.4, 6.5c, and 6.6c show that layered reflectors and reflectors involving attenuative media lead to similar frequency-dependent and phase-shifted reflections. It is therefore useful to see what kinds of constraints could be obtained if we interpreted reflections from elastic layering as "reflections from *Q*" or vice versa. I only consider the more common case of the upper layer being elastic and the lower layer (*e.g.*, a reservoir) being anelastic.

6.4.1 Interpreting Layered Reflectors as Anelastic

Any reasonable frequency-dependent reflectivity $r_n^*(f)$ can be modeled as caused by a contrast in frequency-dependent complex impedance below n^{th} boundary (eq. (6.1)) inferred by the following relation:

$$Z_{n+1}^*(f) = Z_n^*(f)\frac{1+r_n^*(f)}{1-r_n^*(f)}. \tag{6.9}$$

For example, the reflectivity in Model I (Figure 6.3) can be accurately reproduced by a single reflection from a contact between an elastic medium (impedance Z_1) with another medium with complex-valued impedance (6.9). This complex impedance leads to phase velocity

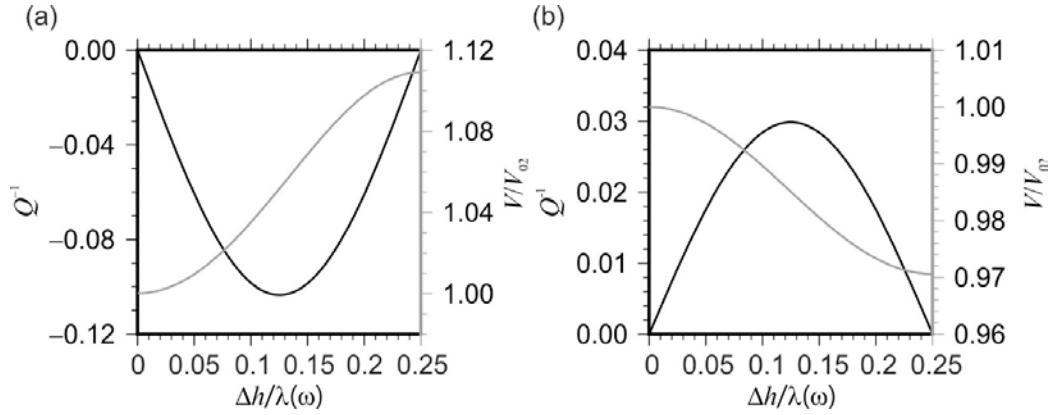

Figure 6.7. Q^{-1} and phase velocity dispersion V/V_{02} for Model II that would reproduce the reflection responses of Model I (Figure 6.4): (a) for structure 1 (high-impedance thin layer), (b) is for structure 2 (intermediate-impedance thin layer) (Figure 6.2).

$$V_2(f) = \frac{\mathrm{Re}\, Z_2^*}{\rho_2}, \tag{6.10}$$

and Q-factor:

$$Q_2^{-1}(f) = -2\frac{\mathrm{Im}\, Z_2^*}{\mathrm{Re}\, Z_2^*}. \tag{6.11}$$

The resulting inverse $Q(f)$ and frequency-dependent $V(f)$ are shown in Figure 6.7.

Again note that the $Q(f)$ and $V(f)$ in relations (6.10) and (6.11) are apparent, *i.e.* only arising from a certain way of interpreting the seismogram and not directly related to internal friction within the material. This type of Q (produced by a short packet of reflections) was called "fluctuation" Q by Morozov and Baharvand Ahmadi (2015). This Q (somewhat related to "scattering Q" but lacking its statistical character) can have arbitrary values, and in particular, it can be negative.

From Figure 6.7, in the case of a high-impedance thin layer (the case $Z_3 < Z_2$), an alternate interpretation by using Model II would yield a negative Q but positive velocity dispersion for its bottom layer. These properties of the reflected waves indicate an influx of energy caused by increased reflectivity at higher frequencies and correspond to the case of anomalous dispersion in optics. Conversely, for progressively increasing impedances within

the reservoir ($Z_3 > Z_2 > Z_1$), Model II results in a positive Q and negative $V(f)$ dispersion within its bottom layer. This case represents normal dispersion in optics, which is also observed for surface seismic waves (Aki and Richards, 2002).

Finally, in practical observations, the approximation $Q(f) \approx$ const is often used, and it is therefore useful to invert the phase-rotated elastic reflections (Figure 6.4) for such types of Qs. To obtain such Q estimates, I simulated reflections in Model II for multiple Q values (Figures 6.5c, and 6.6c) and matched them with the time-domain waveforms in Model I (Figure 6.4). The reflection from a high-impedance layer (Figure 6.4a) cannot be explained by a positive Q below the reflector because of its opposite sense of phase shift. For a reflection from structure 2 in Model I (Figure 6.4b), a reasonable match of the waveform is obtained by setting $Q = 18$ below the reflector (Figure 6.8). The optimal Q value was selected to ensure close durations and shapes of the waveforms, although the reflection amplitude is overestimated by this constant-Q approximation (Figure 6.8).

6.4.2 Interpreting Anelastic Reflectors as Layered

Conversely to the preceding case, any frequency-independent reflection

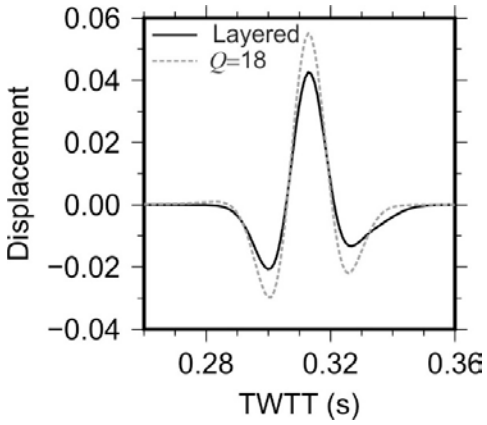

Figure 6.8. Modeling a reflection (black line) from a thin-layer Model I (Figure 6.4b) by a single reflector with frequency-independent $Q = 18$ below it (dotted line).

seismogram $\{r_i\}$ acquired over an anelastic medium can always be interpreted as resulting from pure elastic layering. Again disregarding the multiples for simplicity, the elastic impedance series for this layering can be given by a recursive inverse of relation (6.1):

$$Z_{n+1} = Z_n \frac{1+r_n}{1-r_n}. \tag{6.12}$$

To illustrate this observation in time domain, let us consider the lower layer of Model II with Q = 10. The corresponding reflection signature (black line, Figure 6.5c) can be closely approximated by a superposition of several reflections reflected from a thin-layered elastic structure shown in Figure 6.9.

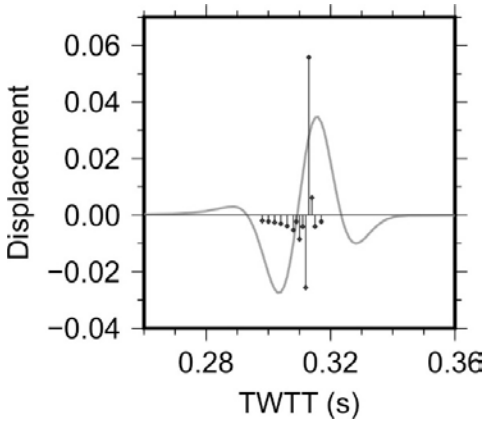

Figure 6.9. Alternative explanation of a single reflection from a low-Q medium (gray line; Q = 10 in Figure 6.5c) by a purely elastic layered structure. Vertical bars represent densely-spaced elastic reflectors yielding the same reflected waveform.

6.4.3 Effects of Offset-Dependent Reflections

The next question important for (potential) measuring of Q from reflections is related to its variations with offset in pre-stack seismic imaging. To assess a simple and realistic model, I simulated offset-dependent reflections for single-step and layered structures (Figure 6.10) by using the "reflectivity" method by Fuchs and Müller (1971). This mode-summation ("propagator") based (Aki and Richards 2002) method accounts for all multiples and arbitrary layering, and produces 3-component synthetics in a 1-D layered model. The

source wavelet is a 6-ms Müller-Fuchs wavelet (Fuchs and Müller, 1971), and the modeling was conducted within the frequency window from 1 to 440 Hz. The parameters of the depth model were chosen by using Gardner's et al. relation (1974) and assuming the P- to S-wave velocity ratio equal $\sqrt{3}$. The thickness of the layer immediately below the reflector was selected slightly below the dominant half-period (and therefore $\Delta h < \lambda/4$ at the dominant frequency; columns on the right in Figure 6.10).

In the panels on the left in Figure 6.10, these vertical-component reflection seismograms are aligned to match the zero-offset reflections for all models. As in Figure 6.4,

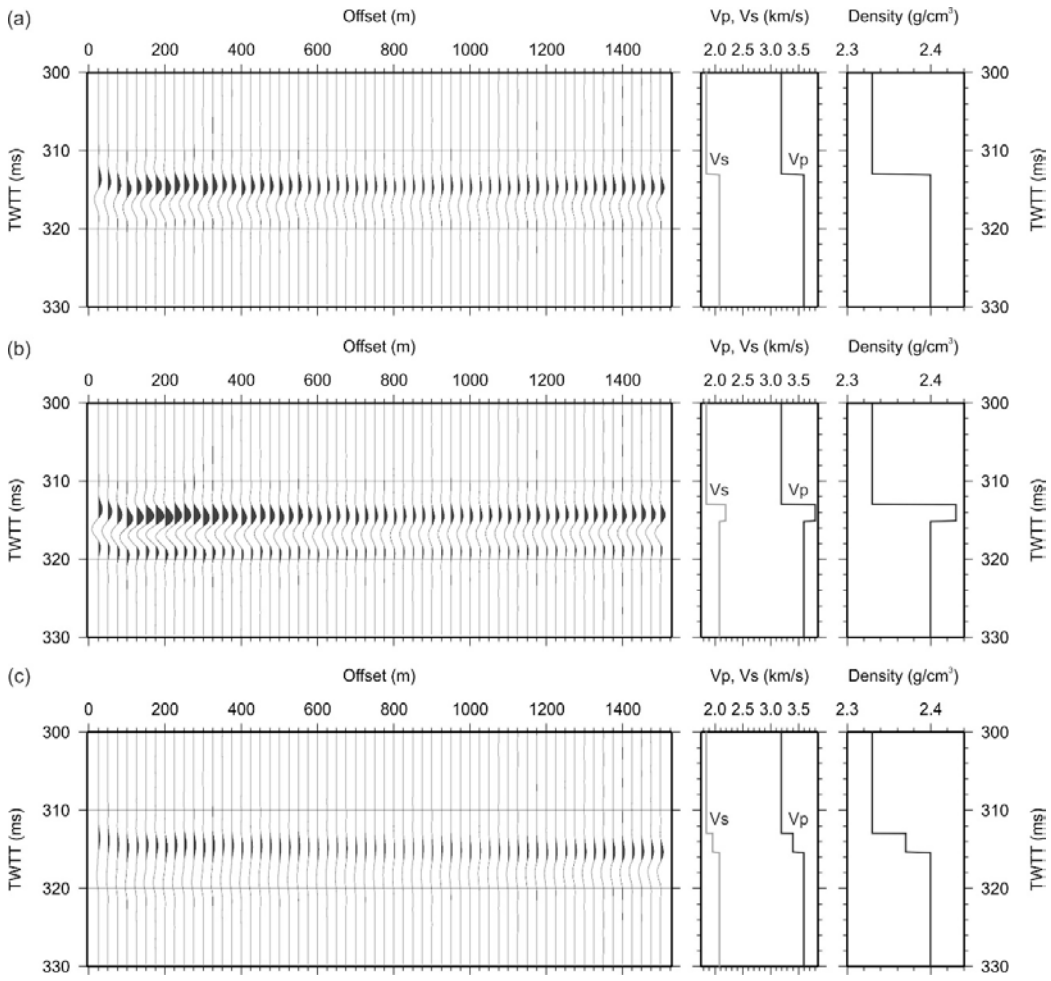

Figure 6.10. Offset-dependent elastic P-wave reflections synthetics: (a) from a single-step velocity and density model; (b) in model I with a high-velocity and density thin layer; (c) in model I with progressive increase in velocity and density.

reflections from layered structures (Figures 6.10b and 6.10c) are similar to those from a single boundary (Figure 6.10a), have slightly different amplitudes and dominant frequencies, and appear slightly phase-rotated. Similar to the preceding subsection, I can try explaining these modifications of the waveforms by a single anelastic reflector. For an illustration, I selected three traces at offsets of 150 m, 275 m and 775 m. Figures 6.11a to 11c show the alternative interpretations of these waveforms by using relations (6.10) and (6.11) and assuming structure 1 for the anelastic reflector, and Figures 6.11d and 6.11f are similar interpretations assuming structure 2.

The results of inversion for the apparent Q^{-1} (Figures 6.11b and e) and velocity dispersion (Figures 6.11c and f) are consistent with the normal-incidence analysis (Figure 6.7)

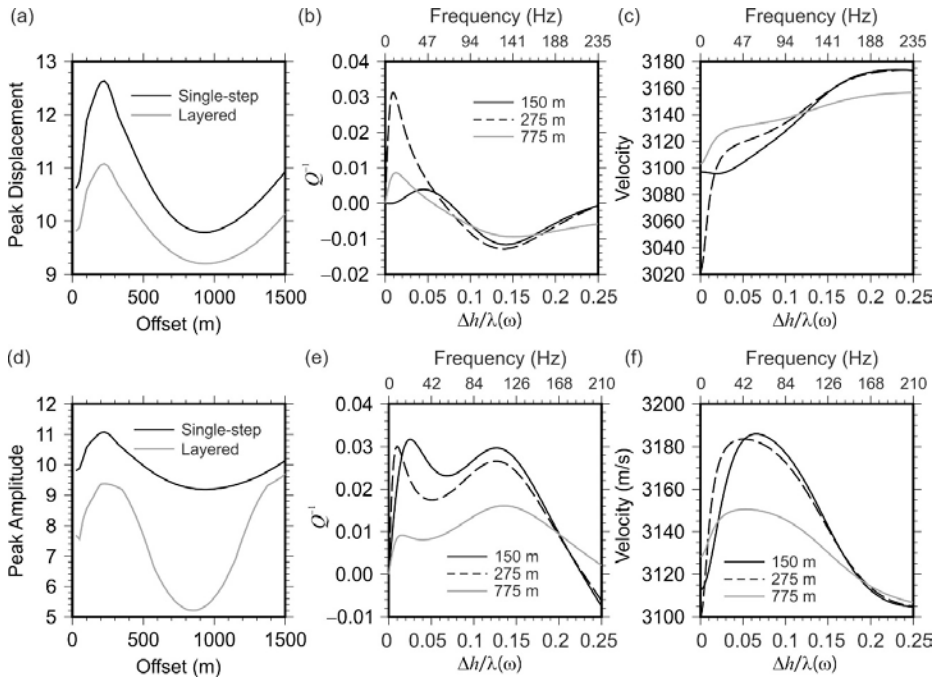

Figure 6.11. Measurements of the apparent Q and velocity dispersion from offset-dependent reflectivity synthetics: (a) Peak amplitude variation with offset of reflections in the single-step model (Figure 6.10a; black line) and layered model with structure 1 (Figure 6.10b; gray line); (b) Equivalent Q^{-1} interpretations at three offsets (legend); (c) the associated velocity dispersion for layered-structure reflections (Figure 6.10b) at different offsets (legend); (d) – (f): same as (a) – (c) for structure 2. In plots (b), (c), (e), and (f), the unscaled modeling frequencies are shown along the top.

but indicate additional complexities due to multiples, geometric spreading, and oblique-incidence related effects. For structure 1, a negative Q and anomalous dispersion is derived, with a low dependence on offset at scaled frequencies $\Delta h/\lambda$ above about 0.05 (47 Hz; Figures 6.11b and c). For structure 2, a positive Q with normal dispersion is suggested, with significant variations with offset (Figures 6.11e and f). These variations of the apparent Q and dispersion with offset (which can be called QVO and DVO, respectively) could create additional complexities in inverting for a consistent attenuation model of the subsurface.

The additional peaks in $Q^{-1}(f)$ at low frequencies ($\Delta h/\lambda$ below 0.02–0.05 in Figures 6.11b and 6.11e) as well as the drop in the amplitudes at source-receiver offsets below ~200 m (Figures 6.11a and 6.11d) may be related to some limitations of the modeling procedure.

6.5. Discussion

The simple models in this paper show that based on reflection seismic data alone, it is impossible to tell whether short-scale anelasticity or layering is present within the medium. Both the Q and finely layered structure (thinner than quarter of the dominant wavelength) are *apparent, i.e.* dependent on the imaging paradigm and assumptions about the structure and mechanics of the medium. The above modeling shows that in realistic environments, it is possible to interpret reflection seismograms as either caused by purely elastic and finely-layered structures with amplitude variations with offset (AVO) or as less layered but anelastic structures with (potentially) offset-dependent Q and velocity dispersion (QVO and DVO). In reality, the true structure should lie somewhere between these end-member models.

Measurements of Q and/or velocity dispersion $V(f)$ always require additional constraints, which can come from geology or rock physics. For example, theoretical analysis

of anelasticity and derivation of all basic relations for Q causality is typically based on assuming a fairly unrealistic case of a uniform medium without ray bending or reflectivity (Aki and Richards, 2002). More realistic (but still debatable by geologists and stratigraphers) constraints include sparseness of reflectors or their "sharpness", *i.e.* relative absence of thin layers and gradational zones of reflectivity. A preference for the Q-type explanation of phase-shifted reflectivity may be justified if one expects only a single sharp contact between two quasi-uniform media. Geological constraints can be of statistical type, for example requiring "stationarity" or "whiteness" of the elastic part of reflectivity, or smoothness of the depth distribution of Q. Such constraints are most difficult to satisfy at short depth scales.

More realistic constraints relevant to reflection imaging could come from rock physics considering specific models of materials, such as the poroelastic model, squirt- or wave-induced fluid flows, solid viscosity (Deng and Morozov, 2016), or thermoelasticity. Such constraints are most consistent physically, but they are also the most difficult to apply, because they require extremely detailed models of the subsurface. The Q factor derived from physics-based models is guaranteed to be non-negative, and therefore cases of fluctuation $Q < 0$ (Figures 6.7a or 6.11b) should definitely be attributed to layering (Morozov and Baharvand Ahmadi, 2015). Rock-physics models could constrain the frequency dependences of $Q(f)$ and $Z(f)$, which would reduce the ambiguity of interpreting thin-layer reflectivity.

In practical field and laboratory studies, realistic constraints inferred from well logs or rock-physics models are rarely available. In their absence, *ad hoc* assumptions are often used, such as a perceived simplicity of the model, frequency-independence or power-law dependence of Q on frequency, or specific relations for velocity dispersion. Such assumptions were also used in the present paper, for example in the form of the Kjartansson's

(1979) dispersion law and impedance formula (6.4). A strong assumption that is so widespread that it often remains unnoticed is the adherence to the viscoelastic model of attenuation. However, the viscoelastic model is inaccurate for fluid-saturated porous rock important for reflection seismology (Morozov, 2015). In particular, this model does not explain the specimen-size related attenuation peak mentioned in section 6.2 (Figure 6.1a).

Unfortunately, the impact of inaccurate models of elastic structures on the quality of interpretations of attenuation is difficult to assess. If significant anelastic attenuation is expected in a study area, we need to be prepared to observe a trade-off between the images of thin-layer reflectivity and Q variations, and between AVO, QVO, and DVO. Similar uncertainties related to crudely simplified models of elastic structures involved in measurements exist in other areas of seismology. In addition to those shown in Figure 6.1, an important example is the scattering Q. This quantity is also apparent (Richards and Menke 1983), and because the transmission coefficient is directly related to the reflection coefficient discussed above, the scattering Q similarly trades off with fine structure of reflectivity. However, because of its statistical nature, the scattering Q trades off not with deterministic thin layering but with geometric spreading (Morozov, 2010) and with statistical attributes of reflectivity distribution.

6.6. Conclusions

In order to measure the Q factor, particularly its frequency dependency, an adequately accurate model of the underlying elastic structure is required. In different types of measurements, the elastic structure can be represented by geometric spreading, layering, or the construction of the measurement apparatus used in the laboratory. In practical studies, accurate models of such elastic structures are rarely used and may be difficult to attain, which

may result in an apparent character and gross uncertainties of the resulting *Q*s.

The trade off with the elastic structure is illustrated for *Q* estimation by using seismic reflections at normal-incidence and offset recording. Reflections from thinly layered structures can look like viscoelastic reflectors and vice versa. Both of these models produce frequency-dependent reflection amplitudes and phases, from which the velocity dispersion and *Q* can be measured. However, both of these quantities are to a certain degree apparent and trade off with each other. Observations of phase-shifted reflectivity can be explained by either thin layering or anelasticity below the reflector. In particular, the apparent *Q* is positive (and therefore likely more expected in practice) for a stepwise increase of impedance at the top of high-impedance reflector. For a high-impedance lid on top of the reflector, the apparent *Q* will be negative, or alternatively a low positive *Q* can be placed above it. The attenuation and velocity-dispersion phenomena are concomitant but may not necessarily agree with the constant-*Q* or other standard relations commonly used in seismic interpretation. Knowledge of such relations from geology, laboratory experiments, or rock physics are required in order to differentiate between layered and anelastic zones within the Earth.

CHAPTER 7

SEISMIC-*Q* COMPENSATION BY ITERATIVE TIME-DOMAIN DECONVOLUTION

In this Chapter, I switch from the topic of physics and attenuation modeling to its correction in reflection seismic records. Morozov et al. (*Geophysics*, in revision) recently suggested that because of the fundamental properties of seismic *Q* (Chapter 2) its correction in seismic records (*Q*-compensation) can be achieved in two separate steps: 1) modeling by many methods, such as discussed in Chapters 2–6, and 2) deconvolution, also by multiple methods. In this Chapter, I explore a new time-domain deconvolution method that has not yet been used for *Q*-compensation. The presentation in this Chapter is based on the following paper:

***Deng, W.**, and I. B. Morozov. 2016 Seismic-Q compensation by iterative time-domain deconvolution, Geophysical Prospecting, in revision*

 My contribution in this co-authored paper consisted in participation in the development of the approach and development of numerical algorithms and examples and preparing the manuscript. The text was modified and reformatted for incorporation in the present dissertation.

7.1 Abstract

Attenuation is often significant during seismic wave propagation in the subsurface, leading to reduced resolution and narrower bandwidth of seismic images. Traditional corrections for such effects, such as inverse-*Q* filtering and deconvolution, are performed in the frequency domain or by using time-spectral decompositions. Here, I propose a pure time-

domain method offering significant advantages in the resolution and interpretational quality of the resulting images. Similar to wavelet transforms, the iterative time-domain deconvolution (ITD) represents the seismogram by a superposition of non-stationary source wavelets modeled in the appropriate attenuation model. Arbitrary frequency-dependent Q and velocity dispersion laws can be used, as well as non-Q type attenuation caused by focusing, defocusing, scattering, effects of fine layering, and fluctuations of the wavefield. Owing to the time-domain formulation, the method does not boost high-frequency noise and is less sensitive to the accuracy of the Q model. I illustrate and compare this method to inverse-Q filtering by using several synthetic and real data examples. The tests include noise-contaminated data, inaccurate Q models and variable source wavelets. The examples show that the ITD is a practical and effective tool for Q-compensation with a broad scope of potential applications. An important benefit of ITD could be the ability to utilize geological information, such as locations and sparseness of major reflectors or the presence of interpreted Q contrasts.

7.2 Introduction

Seismic waves are affected by attenuation and dispersion caused by the inelasticity of the subsurface. In reflection seismic imaging, these effects are adverse and result in frequency-dependent amplitude reduction, narrowing down of the frequency bandwidths, and phase distortions. Attenuation effects decrease the resolution of reflection seismic data, especially within deeper parts of the sections (Wang, 2008; van der Baan, 2012). Attenuation effects may also cause difficulties in imaging and interpretation, such as in horizontal event tracking and identification of small faults.

By studying the attenuation and dispersion in seismic records, two complementary

objectives can be achieved: 1) measuring these effects and including them in interpretation, and 2) their removal from final images. For the first objective, detailed knowledge of attenuation mechanisms is required. However, in most practical studies, detailed knowledge of the layering or rock-physics mechanisms of internal-friction is not available, and their determination is a subject of many studies. Nevertheless, even when the physical mechanisms are poorly known, attenuation and dispersion effects can be modelled (and corrected for) empirically by constructing time-dependent attenuation operators (section 8.3). Generally, this correction represents some type of deconvolution of the empirical attenuation filter (Hale, 1981; Morozov et al., in revision) from the data.

Deconvolution of attenuation and dispersion effects is an inverse filtering process that attempts removing the linear filtering imposed on the wavelet by the Earth. By removing such linear filtering, deconvolution results are likely to provide more recognizable reflection events with higher resolution (Sheriff, 2002). Numerous methods of deconvolution exist, each offering certain advantages in specific applications. In particular, for amplitude-only corrections in *Q*-compensation, time-variant spectral whitening is a simple and convenient method not requiring the knowledge of a *Q*. In this case, the time-variant deconvolution is zero-phase, with power response approximated by an inverse of the time-variant power of the data (which is close to Wiener deconvolution). To implement this deconvolution, time-domain seismic data are first decomposed into time-frequency panels by using a series of narrow band-pass filters, and then the spectral amplitudes are equalized at all times (Yilmaz, 2001). Another broadly used method for correcting for attenuation and dispersion effects is the inverse-*Q* filtering (Hale, 1981). This procedure can also be viewed as deconvolution (Bickel and Natarajan, 1985), although Hargreaves and Calvert (1991) note that its treatment

of frequency components is also analogous to Stolt migration. As in all types of frequency-domain deconvolutions, this method faces the problems of noise and instabilities related to amplifying high-frequency components of the records.

In this Chapter, I draw attention to another broad class of deconvolution methods that is useful and offers several unique features for *Q* compensation. Instead of time-varying frequency-domain inverse filtering, I propose using time-domain methods, and in particular a simple iterative algorithm popular in earthquake seismology (Kikuchi and Kanamori, 1982; Ligorría and Ammon, 1999). This algorithm is called the Iterative Time-domain Deconvolution (ITD) further in this paper. ITD represents the seismogram as a superposition of non-stationary source wavelets modeled using an appropriate empirical attenuation model. Because of the use of an iterative data-fitting procedure in time domain, this approach can be viewed as a wavelet transform or matching pursuit algorithm based on modeling the source waveform propagating through the section. Time-domain formulation encourages application of numerous ideas beyond the traditional *Q*-compensation, such as combining multiple physical mechanisms of attenuation, scattering, or geometrical spreading, or deconvolution starting from stronger reflectors (as done by ITD). As shown in section 8.4, ITD is less sensitive to the accuracy of the *Q* model and of the estimated source wavelet. As a method using time-domain waveform matching, ITD can (in principle) incorporate additional information derived from geology, stacked seismic data or well logs, such as positions and sparseness of major reflectors or their sharp or gradational characters.

In the following, I briefly review the concepts of inverse-*Q* filtering in relation to the formulation of the ITD (section 8.3). In section 8.4, I examine and illustrate the flexibility and power of ITD by comparing it to the inverse-*Q* filtering of synthetic and real seismic data.

7.3 Method

In time-variant deconvolution, a recorded seismic waveform can be regarded as a function $d(t, t_0)$ of two times defined at different scales: the two-way reflection time t_0 characterizing the depth of recording and the "local" wave time t near t_0. The phase of the wave quickly varies with t whereas the amplitude and spectral attributes (such as Q) vary comparatively slowly with t_0. I implement this hierarchy of time scales by windowing the data using a sequence of overlapping time windows, as it is often done in time-variant filtering of seismic records (Yilmaz, 2001). Each window is characterized by the time of its center t_0 and contains a Hanning taper applied to the data record. The continuous reflectivity series represents a sum of windowed records: $r_{\text{complete}}(t) = \sum_{t_0} r(t, t_0)$, with analogous relations for date records $d_{\text{complete}}(t)$ before and after compensation (Morozov et al., in revision).

Linear interpolation of the windowed records allows producing the dependences $d(t, t_0)$ at relatively sparsely sampled times t_0, which greatly reduces the computational cost (Morozov et al., in revision). The sufficiency of a sparsely-sampled sequence of times t_0 implies a relatively smooth variability of Q with depth. This requirement may appear somewhat stringent and unexpected, considering that layered Q models are often used in inverse Q filtering (e.g., Hargreaves and Calvert, 1991; Wang, 2008). However, based on fundamental observations by White (1992), Morozov and Baharvand Ahmadi (2015) pointed out that the Q is not a property of the medium but always an *apparent* property of a wave in it. Because of this wave character, the Q cannot be defined as a combination of some localized physical parameters of the medium, and it can only be measured by averaging over significant time intervals (coherence length of the wave; White (1992)). Thus, measurable Q

models are always apparent and inherently smooth in time and space. However, physical models of attenuation (such as solid viscosity, thermoelasticity, or poroelasticity) can have arbitrary variations in space, which will again produce a smoothly-varying apparent Q (Morozov et al., in revision). Also, arbitrary layered viscoelastic-Q models and dense sampling of t_0 can still be *formally* used in ITD, similarly to inverse-Q filtering (Hargreaves and Calvert, 1991; Wang, 2008).

The seismogram within a window centered at time t_0 can be represented by a convolution of the propagating source waveform $w(t, t_0)$ and the reflectivity series $r(t,t_0)$:

$$d(t_0) = w(t_0) * r(t_0), \tag{7.1}$$

where dependences on t are now implied in all factors, and symbol '$*$' denotes the usual convolution operation with respect to time t. For simplicity, I omit the additive noise in this convolutional model. Note that the "reflectivity" series $r(t_0)$ may not necessarily represent only the normal-incidence reflection coefficients within the subsurface. The only definitive property required by eq. (7.1) is that the record $r(t_0)$ contains all information from $d(t_0)$ that is not accounted for by the modeled attenuating source waveform $w(t_0)$. For example, $d(t_0)$ can be the propagating waveform of a direct wave, in which case the $r(t_0)$ would represent the near-source reverberations and multiples. If $w(t_0)$ contains amplitude and/or Q variations with offset (AVO or QVO) effects (Dasgupta and Clark, 1998), multiples, or other types of coherent noise, these effects would be corrected for in $r(t_0)$. However, in common practice and examples in this paper, predominantly layered Q models are considered, and consequently the AVO and QVO effects remain in $r(t_0)$ and the resulting Q-compensated $d_{el}(t_0)$ that would be observed by seismic recording in a purely elastic medium.

The notion of the "source waveform" $w(t_0)$ in eq. (7.1) also needs to be carefully understood. The seismic wavefield is formed at a significant distance from the source ("far

field"), where the medium deformation becomes linear and the reflections, conversions, and reverberations within the near-surface structure form a consistent spreading pattern (Sheriff 2002). Scattering, attenuation (Q^{-1}) and spectral-fluctuation effects (Morozov and Baharvand Ahmadi, 2015) can also be extremely high in the proximity of the weathering layer (Al-Shukri et al., 1995; Wilson and Pavlis, 2000). Thus, $w(t_0)$ can only be assessed at a certain distance from the source. As a practical proxy for this distance, I use the time of the uppermost portion of the reflection record. As discussed below and in section 7.5, this source waveform can generally be estimated from the data and denoted $w(t_0 \approx 0)$. With increasing two-way time t_0, this waveform modifies through multiple propagation mechanisms (refraction, reflection, mode conversion, and attenuation) (Morozov et al., in revision) and becomes the time-variant waveform $w(t_0)$.

Let us now denote $w_{el}(t_0)$ an analogous source waveform (defined in the sense of the preceding paragraph) that would have been observed in the absence of attenuation. The corresponding seismic record $d_{el}(t_0)$ would be related to it by the same convolutional model:

$$d_{el}(t_0) = w_{el}(t_0) * r(t_0). \tag{7.2}$$

The actual $w(t_0)$ and $d(t_0)$ can then be related to $w_{el}(t_0)$ and $d_{el}(t_0)$ by a linear attenuation filter $a(t_0)$ (Hale, 1981; Morozov et al., in revision):

$$w(t_0) = a(t_0) * w_{el}(t_0), \text{ and } d(t_0) = a(t_0) * d_{el}(t_0). \tag{7.3}$$

The goal of attenuation compensation is to invert the second equation in (7.3) for "elastic" data $d_{el}(t_0)$. This inversion is conventionally done in the frequency domain, in which the local time t is replaced with angular frequency ω and the convolution becomes multiplication:

$$D(\omega, t_0) = A(\omega, t_0) D_{el}(\omega, t_0). \tag{7.4}$$

According to the usual convention, uppercase letters represent Fourier transforms of the corresponding time-domain functions. Note that in contrast to the Fourier formulation of time-variant filtering by Margrave (1998), I do not transform t_0 to its counterpart frequency variable, and the multiplication in the right-hand side of eq. (7.4) does not become convolution).

Frequency dependences of the complex-valued attenuation/dispersion spectrum $A(\omega, t_0)$ can be complex and contain effects such as source-receiver coupling, geometric spreading, tuning, as well as inelasticity. Morozov et al. (in revision) described all these effects as a superposition of linear filters. In this paper, I only focus on the "attenuation" filter whose action can be lumped in a phenomenological quality factor Q. Such filters are usually taken in several standard forms determined by the Q-factor alone (Wang, 2008). For example, the constant-Q model is (Kjartansson, 1979):

$$A(\omega, t_0) = \exp\left(i\omega t_0 \gamma - \frac{\omega t_0 \gamma}{2Q} \right), \text{ where } \gamma = \left(\frac{\omega}{\omega_0} \right)^{\frac{-1}{\pi Q}}, \tag{7.5}$$

where ω_0 is the reference frequency. Wang (2008) recommends taking ω_0 above the seismic frequency band, and Morozov et al. (in revision) argue that dispersion law should be formulated irrespectively to such reference parameters. However, discussions of the specific forms of dispersion law are beyond the scope of this paper.

Relation (7.5) shows that in an anelastic medium, wavelet and data amplitudes are reduced by a factor of $\exp(\omega t_0 \gamma / 2Q)$ after a two-way travel time t_0. The phases of the wave are shifted by $\omega t_0 \gamma$, which needs to be compared to ωt_0 for an elastic medium. Therefore, the phase shift due to dispersion equals $\omega t_0 (\gamma - 1)$. From relations (7.4) and (7.5), the Q-compensated waveform is:

$$D_{\mathrm{el}}\left(\omega,t_0\right)=A^{-1}\left(\omega,t_0\right)D\left(\omega,t_0\right), \tag{7.6}$$

where
$$A^{-1}\left(\omega,t_0\right)=\exp\left(-i\omega t_0\gamma+\frac{\omega t_0\gamma}{2Q}\right). \tag{7.7}$$

The frequency-domain inverse (7.6) is used in inverse-Q filtering of seismic data (Hale 1981; Wang, 2008). However, evaluation of A^{-1} in eq. (7.7) contains a division of the spectra, which is often unstable and increases noise at high frequencies. Such undesirable effects can be reduced by restricting the maximum amplitude of (7.7) or using other regularization approaches (Hale, 1981; Hargreaves and Calvert, 1991; Zhang and Ulrych, 2007; Wang, 2008). For the following discussion, note that this regularization is always achieved by replacing the exact inverse operator (7.7) with some approximation reducing its response at high frequencies.

Here, I propose a different approximate solution for Q-compensated data (7.6) by using an iterative time-domain deconvolution (ITD) method. Instead of solving the inverse problem for operator A^{-1} in (7.7) in frequency domain, this method performs the transformation $d\left(t_0\right)\rightarrow d_{\mathrm{el}}\left(t_0\right)$ (or equivalently, $D\left(\omega,t_0\right)\rightarrow D_{\mathrm{el}}\left(\omega,t_0\right)$) directly, by iteratively performing cross-correlations with the forward-modeled wavelet in time domain. In this method, the "reflectivity" series $r(t, t_0)$ within a window centered at t_0 is approximated by a series of pulses with amplitudes $r_i(t_0)$ located at times $\tau_i(t_0)$:

$$r\left(t,t_0\right)=\sum_{i=1}^{N}r_i\left(t_0\right)\delta\left(t-\tau_i\left(t_0\right)\right), \tag{7.8}$$

where $\delta(t)$ is the delta function. The number of pulses N per time window is either set by the analyst or selected adaptively based on waveform energy criteria described below. With few pulses, only the strongest reflections are reproduced, and with large N, the complete reflection series $r(t,t_0)$ is retained. By substituting eq. (7.8) into (7.1), the seismic record is

presented by a superposition of wavelets of amplitudes r_i and placed at times τ_i:

$$d\left(t,t_0\right)=\sum_{i=1}^{N} r_i\left(t_0\right) w\left(t-\tau_i\left(t_0\right),t_0\right). \tag{7.9}$$

Instead of looking for a potentially unstable inverse of the wavelet (7.7), I solve equation (7.9) for "reflectivity" series by using a synthetic wavelet $w(t_0)$ modeled at time t_0 by utilizing an appropriate combination of attenuation mechanisms. The search for $r_i(t_0)$ and $\tau_i(t_0)$ is iterative, starting from the strongest value of $r_1(t_0)$ (Ligorría and Ammon, 1999). The corresponding time τ_1 is found by the maximum cross-correlation between the data and the modeled (attenuated) source waveform: $\int d\left(t,t_0\right) w\left(t-\tau_1,t_0\right) dt$. The associated reflectivity amplitude r_1 is then given by the peak of cross-correlation:

$$r_1 = \frac{\int d\left(t,t_0\right) w\left(t-\tau_1,t_0\right) dt}{\int w^2\left(t-\tau_1,t_0\right) dt}. \tag{7.10}$$

The rest of the reflectivity parameters $r_i(t_0)$ and $\tau_i(t_0)$ are found by subtracting the prediction of the first peak from the waveform:

$$d\left(t,t_0\right) \rightarrow d_1\left(t,t_0\right) \equiv d\left(t,t_0\right) - r_1\, w\left(t-\tau_1,t_0\right), \tag{7.11}$$

repeating the same operations with $d_1(t, t_0)$, and continuing iteratively, with residual waveforms at n-th step defined by $d_n\left(t,t_0\right) \equiv d_{n-1}\left(t,t_0\right) - r_n\, w\left(t-\tau_n,t_0\right)$.

In the ITD procedure (7.10) and (7.11), the strongest contributions to the signal (7.9) are found first and the iteration can be stopped based on several criteria. The simplest practical approach is to restrict the number of pulses N in the resulting solution (eq. (7.9)). The selection of N does not only help to promote the sparsity of the restored signal but also possesses the advantage of preferential recovery of the strongest reflections. The residual energy after n-th iteration is defined by

$$\varepsilon(n) \equiv \frac{\int d_n^2(t,t_0)\,dt}{\int d^2(t,t_0)\,dt}, \tag{7.12}$$

and can be used to evaluate what portion of the input signal is passed by the ITD filter. This parameter can also be used as a threshold for stopping the iterations.

By convolving the resulting "reflectivity" series $r(t_0)$ with the "elastic" source waveform $w_{\text{el}}(t_0)$, the desired Q-compensated data record d_{el} is obtained:

$$d_{\text{el}}(t_0) = w_{\text{el}}(t_0) * r\,. \tag{7.13}$$

As shown in eqs. (7.9) – (7.11) and (7.13), the result of ITD depends on the estimated source waveform $w_{\text{el}}(t_0)$. Thus, the ITD can be described as not purely a Q-correction procedure but rather an attenuated-signal detection or shaping to the signal that would have been observed in an elastic medium. This difference leads to additional requirements to the algorithm but also somewhat different goals and advantages compared to the inverse-Q filtering. The additional requirements to ITD consist in the need to set the waveform $w_{\text{el}}(t_0)$ and to specify the parameters of iterative search, such as the selection of $\varepsilon(n)$ cut-off. In reflection seismic data processing, the source waveform can be estimated by blind or well-log based methods for stationary and non-stationary signals (Oppenheim and Schafer, 1975; van der Baan, 2008). Some of these methods are discussed in section 7.5. In real-data examples (section 7.4), I bypass the complications due to signal non-stationarity by measuring the near-source waveform ($w_{\text{el}}(t_0)$ at small t_0) in inverse-Q filtered records (Morozov et al., in revision). After inverse-Q filtering, the underlying source waveform becomes near-stationary and can be estimated with greater confidence by making zero- or minimum-phase assumptions (Oppenheim and Schafer, 1975). Once the near-source waveform is estimated, the ITD can be used to produce an "elastic" section.

The key advantages of deconvolution (7.13) compared to (7.6) are the absence of inverse operator A^{-1} and identification of the underlying "reflection" sequence $r(t_0)$ that can be analyzed and potentially interpreted. As shown in sections 7.3 and 7.4, spectral properties of the ITD-corrected wavefield are principally controlled by the source waveform, and hence the ITD does not boost the high-frequency noise more than the low-frequency one. Because of its working from the stronger reflections to weaker ones, the procedure is also less sensitive to errors in Q.

7.4 Numerical Experiments

To illustrate the operation and performance of ITD in reflection imaging, I conduct a series of simple numerical tests using 1-D synthetic seismograms (subsections 7.4.1 to 7.4.5) and a more realistic example using one common mid-point (CMP) from Marmousi-II model (subsection 7.4.6). In the sparse-reflector tests, 1500-ms long records contain five reflectors (Table 7.1) illuminated by a 30-Hz zero-phase Ricker wavelet as the source. Elastic waveform with $Q = \infty$ is shown in Figure 7.1a. The lengths of overlapping time windows are selected equal 200 ms.

Table 7.1. Reflection amplitude model for numerical experiments

Two-way travel time (ms)	344	790	860	1087	1390
Amplitude	1	0.66	–0.59	0.52	0.26

7.4.1 Test with Noise-Free Data

For the noise-free attenuated data in Figure 7.1a, the ITD results are shown in Figure 7.1c and d and compared to inverse-Q filtering results (Figure 7.1b). The inverse-Q filtering result is obtained by using the method by Wang (2008) with the stabilization factor equals 0.005.

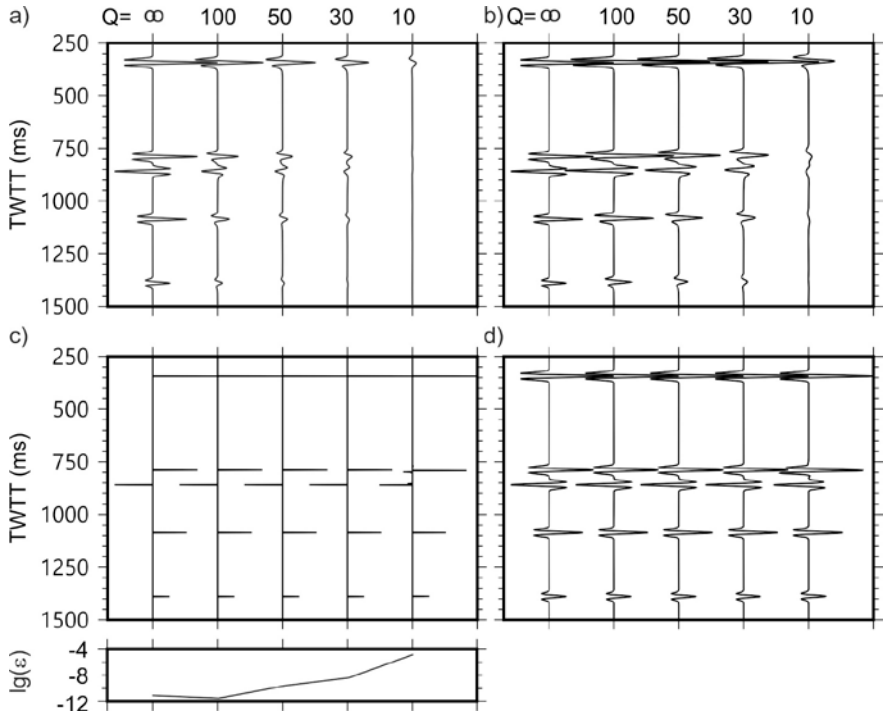

Figure 7.1. Test of Q-compensation methods using noise-free data: a) data with Q equal ∞, 100, 50, 30 and 10 (trace labels) obtained by forward modeling in the reflectivity model in Table 1; b) inverse-Q filtering; c) waveforms Q-corrected by ITD; d) reflectivity model produced by ITD. For $Q \geq 30$, this model also exactly corresponds to the input reflectivity model labeled by $Q = \infty$. Below plot c), which is logarithms of residual data energies are shown (eq. (7.12)).

Inverse-Q filtering results show good corrections for most of the energy loss for weak attenuation (Q = 100; Figure 7.1b). For relatively strong attenuation (Q = 50, 30, and 10), the inverse-Q filter recovers the shallow parts of the records well, but the deeper parts are recovered more poorly (Figure 7.1b). With Q = 100, the amplitude is recovered well but the phase is not, which can be seen by comparing the deepest reflections (the recovered reflections are non-zero phase). By using the same input waveforms (Figure 7.1a), the ITD with a low iteration limit of $N = 8$ accurately recovers the sparse reflectivity series (Figure 7.1d). This is expected, because the times of reflections are accurately identified already in the first iteration of the procedure (7.11). The amplitudes recovered by ITD equal the true reflectivities at all attenuation rates $Q > 10$ (Figure 7.1d). For Q =10, the reflectivities of the two opposite-polarity reflections within the range of t = 790 to 860 ms are

over-estimated (Figure 7.1d). This over-estimation is caused by the interference of these reflections at low frequencies. By convolving the ITD-inverted reflectivity with the source wavelet known from modeling, Q-corrected waveforms are obtained (Figure 7.1c). Low levels of the residual energy shown in Figure 7.1c indicate that all the events are detected in the data well. Comparison of Figures 7.1b and c shows that ITD accurately corrects both the amplitudes and phases of the high-frequency components that have been affected by the regularization in inverse-Q filtering.

7.4.2 Tests with Noisy Data

To test the sensitivity of the method to additive noise, I add several levels of white Gaussian noise to the seismograms with Q = 10 and 50 in Figure 7.1a. The signal to noise ratio (SNR) is defined in dB as

$$\mathrm{SNR}=10\log_{10}\left(\frac{P_{\mathrm{signal}}}{P_{\mathrm{noise}}}\right), \tag{7.14}$$

where P_{signal} and P_{noise} are the powers of the signal and noise, respectively, evaluated over the entire time interval. With strong attenuation (Q = 10, Figure 7.2a), all levels of noise strongly affect the reflections below 0.5 s. When Q = 50, the reflections are strongly affected

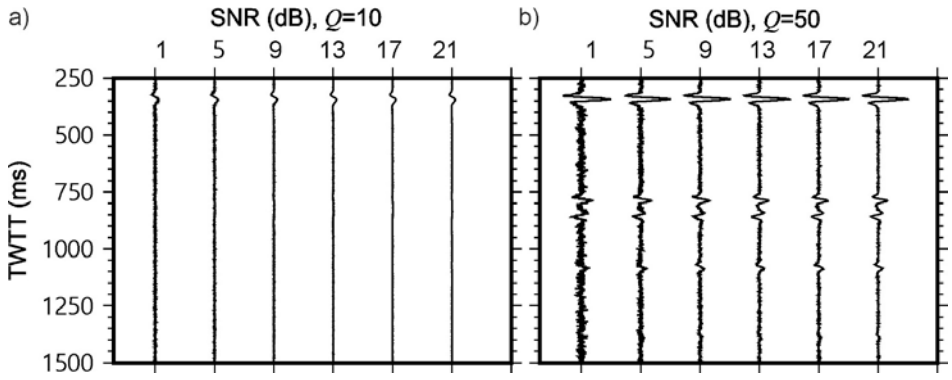

Figure 7.2. Seismograms with different attenuation rates (Figure 7.1) with added Gaussian random noise: a) Q = 10, b) Q = 50. Trace labels show the signal to noise ratios (SNR) in the records.

when the SNR is below 9dB.

Figures 7.3 and 7.4 compare the results of *Q*-compensation of the data in Figure 7.2 by using the inverse-*Q* filtering and ITD approaches, respectively. Prior to inverse-*Q* filtering, the records were filtered by using Ormsby bandpass filters within frequencies of 4−8−50−60 Hz to reduce the high-frequency noise increase due to inverse-*Q* filtering. Compared to Figure 7.3, the ITD with $N = 8$ achieves better results (Figure 7.4). For $Q = 10$, the inverse-*Q* filtering recovers the reflection at $t = 344$ ms (Figure 7.3a) reasonably well, but reflections below this time level are barely recovered, and the noise is also amplified. Even with high SNR, the reflections below 0.5 s still cannot be recovered well. Apparently because of the selected length of the inverse-*Q* filter and its regularization, the records resemble those processed by automatic gain control (AGC), i.e. the high-frequency noise is boosted where the reflections are weak (Figure 7.3). By contrast, ITD recovers the first three reflections well at all SNR levels (Figure 7.4a). When SNR > 5 dB, ITD recovers the first four reflections, and for SNR = 21 dB, all reflections are recovered.

For weaker attenuation with $Q = 50$, inverse-*Q* filtering recovers the first four reflections at almost all SNRs. However, at low SNR levels, the inverse-*Q* filter still over-

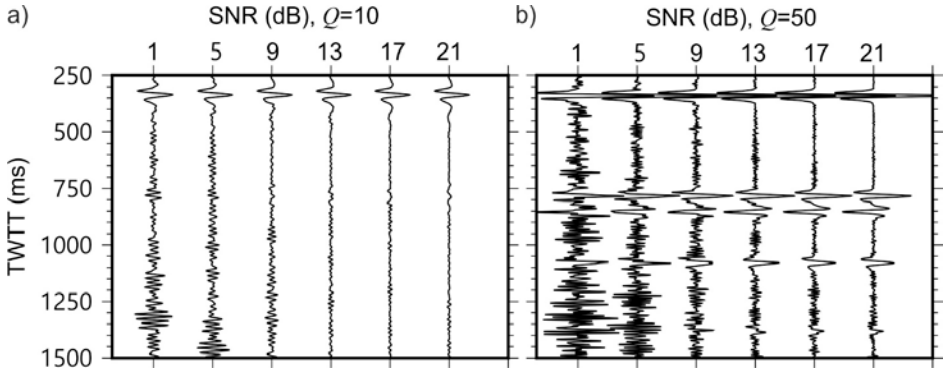

Figure 7.3. Results obtained by stabilized inverse-*Q* filtering: a) $Q = 10$, b) $Q = 50$. Note that apparently because of the effective length of the inverse-*Q* filter and its regularization, the amplitudes of noise increase to the bottom of the section, resembling an automatic gain control (AGC) effect.

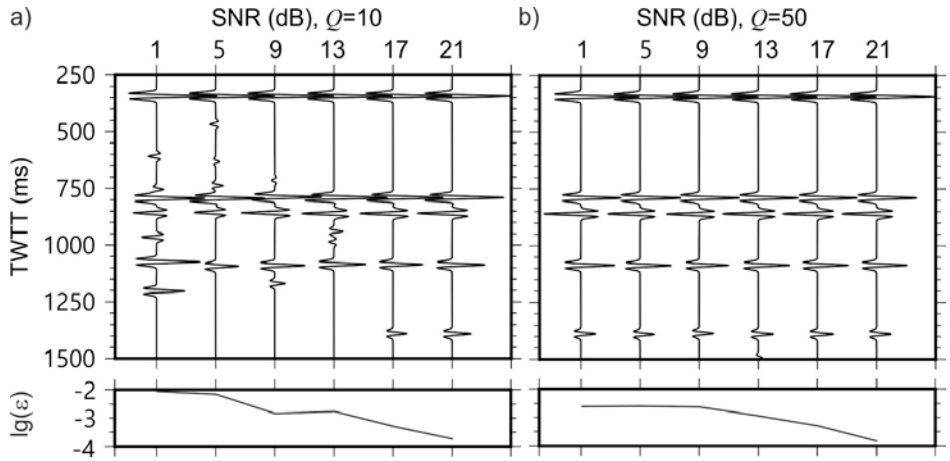

Figure 7.4. Seismograms obtained by ITD inversion of the data in Figure 7.3: a) model with Q = 10, b) Q = 50. The curve below each graph is the logarithm of the residual energy defined by eq. (7.12).

amplifies the noise (for example, for SNR < 13 dB). By contrast, the ITD not only recovers the reflections but also filters out the noise, which helps improving the images (Figure 7.4b).

The residual data error $\varepsilon(n)$ below each graph in Figure 7.4 shows a decreasing trend with increasing SNR levels but does not depend on Q. For low SNR levels, the increased $\varepsilon(n)$ values are due to two factors: biases in measuring reflectivity amplitudes and mis-detection of noise pulses as signal. With increasing SNRs, the signal is recovered more accurately, and the noise is rejected.

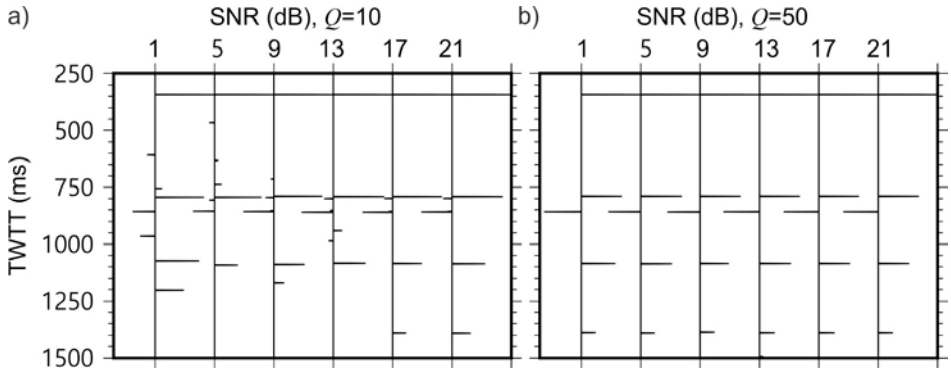

Figure 7.5. Reflectivity records obtained by ITD inversion, corresponding to Q-compensated waveforms in Figure 7.4: a) Q = 10, b) Q = 50.

Seismic data interpretation can benefit not only from corrections for Q effects but also from direct deconvolution for reflectivity, which is an intermediate step of ITD (eq. (7.10)). Figure 7.5 shows that, as expected, with increasing SNR and Q, such reflectivity images become clearer and more accurate. Such reflectivity images with emphasized stronger reflectors can be useful for interpretation.

7.4.3 Test of Inaccurate Q

The causes for wave attenuation are complex and often poorly understood. As a result, the Q is usually an apparent (wave-dependent) property, and its measurements have an inherently limited accuracy (White 1992; Morozov and Baharvand Ahmadi 2015). It is therefore important to check how the different Q-compensation methods respond to inaccurate Q models. In Figure 7.6a, I re-plot the noise-free waveform with $Q = 50$ (Figure 7.1a). Then, I assume that the Q used in ITD forward modeling and inversion equals 20, 40, 50, 60, or 80 (section 2; Figure 7.6b to f). In each case, the error in the modeled level of attenuation is defined as

$$error = \frac{Q_{est}^{-1} - Q_{exact}^{-1}}{Q_{exact}^{-1}} \times 100\%, \tag{7.15}$$

which ranges from −38% to +150%.

Both inverse-Q filtering and ITD are applied to the synthetic data with variable assumed Q levels (Figure 7.6). When the assumed Q is much smaller than the correct one (*error* = +150%), inverse-Q filtering shows very good compensation results in the deeper part (Figure 7.6b) but overcorrects the shallow part. To measure the quality of compensation, I use the correlation coefficient c defined by

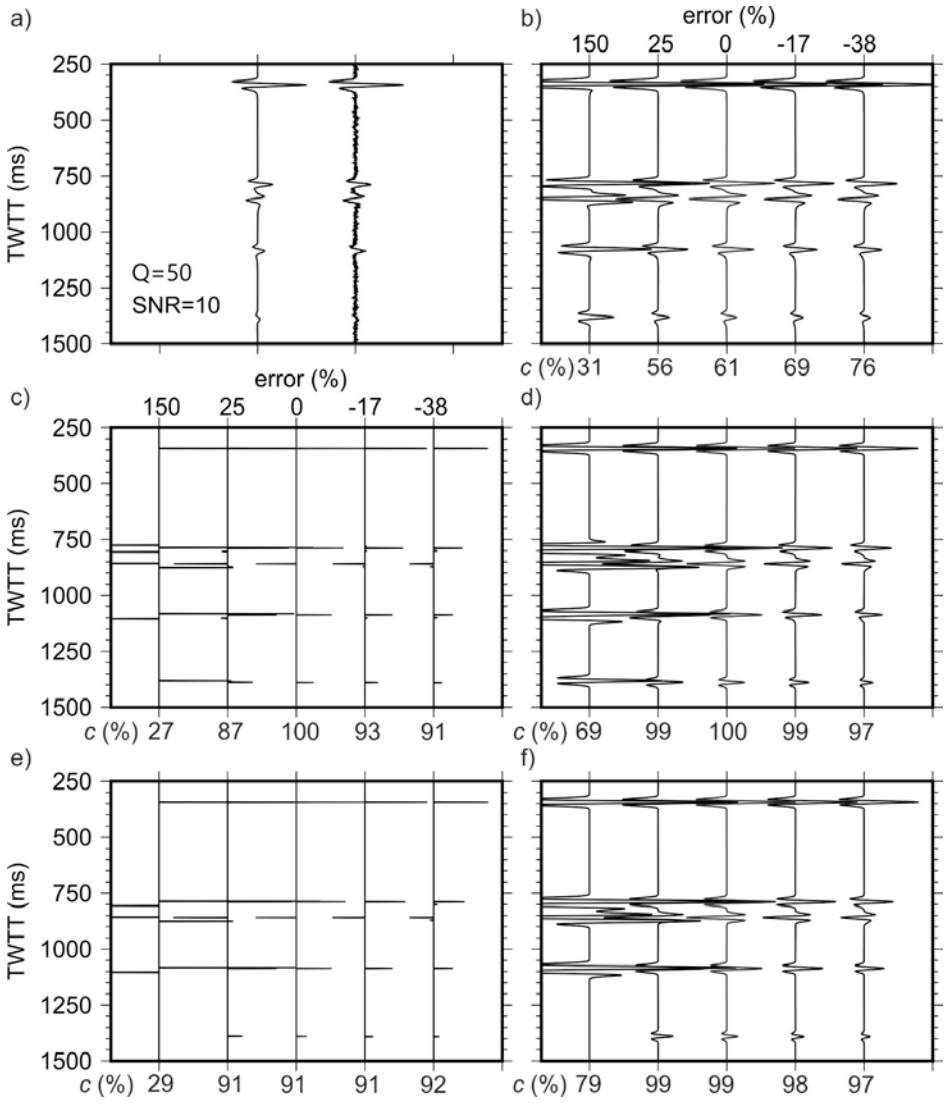

Figure 7.6. Test for an inaccurate Q used in ITD: a) noise-free and noise-contaminated data with $Q = 50$ and SNR = 10 dB; b) inverse-Q filtering result using noise-free data; c) reflectivity model inverted by ITD; and d) ITD-corrected waveform using noise-free data; e) reflectivity model inverted by ITD with noise-contaminated data, and f) the corresponding ITD-corrected waveforms. Trace labels show the relative errors of the Q^{-1} used for modeling and inversion.

$$c = \frac{\mathbf{d} \cdot \mathbf{d}_{\mathrm{el}}}{\|\mathbf{d}\| \|\mathbf{d}_{\mathrm{el}}\|}. \tag{7.16}$$

Here, $\mathbf{d}$ and $\mathbf{d}_{\mathrm{el}}$ denote the vector form of $d(t, t_0)$ and $d_{\mathrm{el}}(t, t_0)$ respectively, '$\cdot$' denotes the inner product of two such vectors, and "$\|\mathbf{v}\|$" is the Euclidean norm of vector $\mathbf{v}$. The correlation coefficient (in the bottom of each graph denotes by c in Figure 7.6) shows that with error ranging from +150% to −38%, the similarity between source waveform and those

obtained by inverse-Q filtering is increasing (Figure 7.6b) and the correlation coefficient changes from 0.31 to 0.76.

With the same Q that is much lower than the correct one (*error* = +150%), ITD over-amplifies the reflection from the deeper parts of the record but reasonably recovers the shallower reflections (Figure 7.6c and 6d). When the assumed Q approaches the correct Q, both the waveforms and reflectivity are close to the reference waveform and reflectivity, and the correlation coefficient approaches 1. For Q errors from –38% to +25% (Figure 7.6d), the correlation coefficient c for waveforms is above 0.90. This appears to be a good level of tolerance to Q uncertainty for practical applications, and therefore I suggest that the correlation level of $c \geq 0.90$ can be used as a waveform criterion of model-parameter sensitivity. When applied to inverting for reflectivity (Figure 7.6c), this criterion shows that ITD can tolerate –38% to almost +25% errors in Q.

It is also important to assess the influence of noise in the presence of inaccurately known Q within the subsurface. To measure this influence, white Gaussian noise is added to the record in Figure 7.6a with SNR = 10 dB, which is also shown in Figure 7.6a. With these strongly noise-contaminated data, the corrected waveforms and reflectivity with inaccurately known Qs are shown in Figures 7.6c and 7.6f. Again, considering the correlation coefficient above 90% as acceptable, the ITD tolerates Q^{-1} errors from –38% to 25% for waveforms and for reflectivity. Because random noise is suppressed by ITD deconvolution, even with accurately estimated Q (error equals 0% in eq. (7.15)), the correlation coefficient for reflectivity is only 91%. A closer inspection of the records shows that this reduced correlation is mainly because of the inverted reflectivity within the deeper part being shifted by one or two milliseconds in the presence of noise. However, Figure 7.6e shows that when

the error in Q^{-1} ranges from about –38% to +25%, the reflectivity is recovered very well except for several weak spurious values. The restored waveform has a high correlation coefficient (between 97% and 99%) if the estimated Q lies from –38% to 25% away from the exact Q (Figure 7.6f). This lower sensitivity to Q is because the convolution with the source wavelet reduces the effects of high-frequency differences among the reflectivity series in Figure 7.6e. This reduced sensitivity is related to the limited accuracy of measuring Q from time-range limited records (White, 1992; Morozov and Baharvand Ahmadi, 2015).

In summary of the above noise and Q testing, compared to inverse-Q filtering, the ITD appears to be less sensitive to inaccurate Q models even in the presence of random noise. Also, the character of noise remaining in ITD-filtered sections differs from the one in inverse-Q filtered records. Instead of amplifying high-frequency noise, the ITD makes the noise more “sparse” and looking like uncorrelated random pulses in the seismic section. Interestingly, uncertainties in the assumed background Q lead to inverting for fine layering with alternating polarities near the reflectors (Figure 7.6c and e; Deng and Morozov, 2017). Because of the absence of direct sensitivity to frequency, the ITD does not increase the “ringiness” of seismic records.

7.4.4 Test of Inaccurate Source Wavelet

ITD requires the knowledge of a source wavelet, and the wavelet estimated from seismic data may be inaccurate (a discussion of wavelet estimation methods is given in section 5). Therefore, it is necessary to understand how the accuracy of wavelet parameters influences the performance of ITD. In this sub-section, two numerical tests for the influence of wavelet phase and peak frequency are discussed. For these two experiments, a noise-free record with a 30-Hz zero-phase Ricker wavelet is utilized. The quality factor Q of the

propagating medium is set equal 50. The reflectivity model for forward modeling is given in Table 7.1. In contrast to the preceding numerical experiments, two values of the number of iterations $N = 20$ and $N = 1000$ are tested (Figures 7.7 and 7.8). The results using unperturbed source wavelets are shown by gray lines in Figures 7.7 and 7.8.

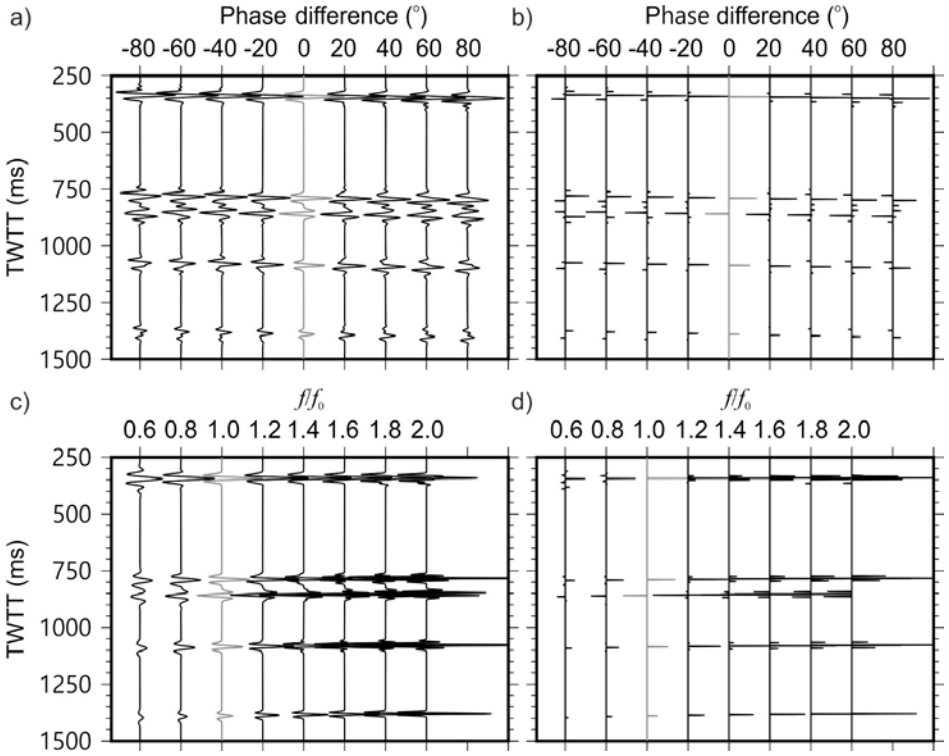

Figure 7.7. ITD results with $N = 20$ of iterations by using variable source wavelets (black lines): a) ITD compensation results with inaccurate wavelet phases and b) the associated reflectivity model; c) ITD compensation results with inaccurate dominant frequency; d) the associated reflectivity model. Trace labels show the phase rotations (plots a) and b)) or dominant-frequency variations (plots c) and d)) applied to source wavelets. Gray lines show the results for an unperturbed wavelet.

In Figures 7.7 and 7.8, two parameters are used for characterizing the shape of the inferred wavelet: its phase and the characteristic length, which is represented by the dominant frequency. Note that it is generally insufficient to only constrain the amplitude spectra of the source waveform, and the phase may have a significant impact on the recovered seismic section. For the maximum iteration limit $N = 20$, ITD results with wavelet phases varying from -80^{o} to $+80^{o}$ are shown in Figure 7.7a, and the inverted reflectivity series are shown in

Figures 7.7b. The waveforms (Figures 7.7a) show that the corrected reflection at t = 344 ms is closer to the accurate source-wavelet shape than those from the deeper parts. This could be due to dispersion effects increasing with time and being added to the phase rotations of the source waveforms. Figures 7.7b suggests that the reflectivity series can be identified accurately by ITD with phase errors of up to ±20º. With phase errors beyond ±20º, the reflectivity series are significantly different from the exact one at $\phi = 0$º. This sensitivity of $r(t)$ to wavelet phase is of course expected and common for all types of deconvolution.

In the second test, I assume the correct zero phase of the wavelet and check the influence of inaccurately estimated peak frequency (Figures 7.7c and 7.7d). For Ricker wavelet, the peak frequency determines the scaling of every part of the waveform. Figure 7.7c shows that with N = 20, if the assumed peak frequency is above or below the exact value, and the result is respectively over- or under-compensated. This bias occurs because of the waves with higher dominant frequencies attenuating faster than those at lower frequencies. Overall, Figures 7.7c and 7.7d show that ITD performs very well with assumed dominant frequencies lying within 0.8 to 1.4 times of the true values.

7.4.5 Sensitivity to the Number of ITD Iterations

As described in section 7.3, ITD filtering is based on an approximate deconvolution (eq. (7.9)), which is controlled by the number of iterations N and/or the data-error threshold ε. With $N \to \infty$, the deconvolution becomes exact and perfectly reproduces the seismic record ($\varepsilon = 0$). Figure 7.8 shows that for noise-free data, a large N = 1000 also allows recovering the "elastic" response even with inaccurately estimated phases and peak frequencies of the source wavelet. With increasing number of iterations, the ITD becomes progressively less sensitive to wavelet estimates (Figure 7.8).

Depending on the number of iterations, the ITD behaves differently and achieves somewhat different goals. For N relatively small compared to the number of samples within the analysis window, the ITD represents a signal-detection method extracting a set of the strongest, usually "sparse" events and correcting them for attenuation and dispersion. By contrast, for large N, the inverted events are no longer sparse but still corrected for attenuation, and therefore the ITD becomes analogous to frequency-domain Q-compensation. Similar to inverse-Q filtering, large-N ITD is independent of the choice of the source wavelet but sensitive to noise and errors in Q. Nevertheless, large-N ITD still does not boost the noise above the frequency band of the source waveform.

7.4.6 Realistic Waveform Synthetic

To illustrate the performance of the algorithm on a realistic reflection waveform, a

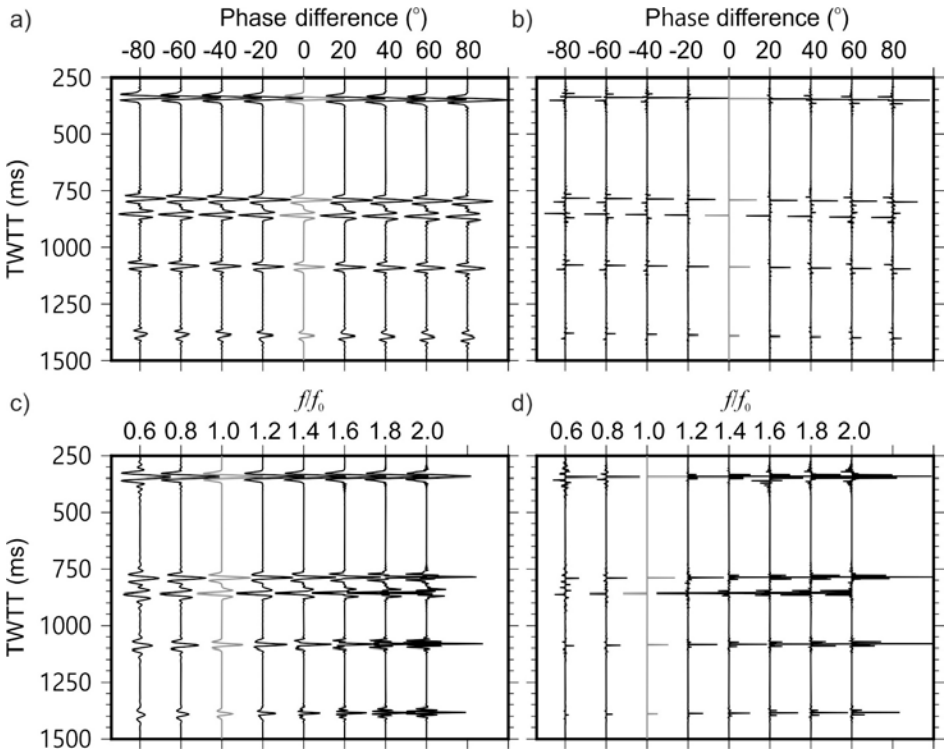

Figure 7.8. ITD results with N =100 iterations by using variable source wavelets. Panels a) – d) have the same meanings as in Figure 7.7.

single 1200 ms-long trace was selected from Marmousi-II synthetics (Martin et al., 2006) modeled for $Q = \infty$, 10, and 50 (Figure 7.9). The synthetics were modeled by using the convolutional model and only considering the primary reflections. The noise level in this example is low (as resulting from numerical synthetics), and here we are interested in the recovery of complex waveforms. Both modeling and ITD were performed by using a 30-Hz Ricker wavelet. To perform the ITD iterations, I selected 200-ms time windows and threshold parameters $N = 200$ and residual energy $\varepsilon = 10^{-7}$. In the inverse-Q algorithm, the stabilization factor was set equal to 0.005 (Wang 2008).

For $Q = 50$ (Figure 7.9b), comparisons of the filtered records (black lines) to the record modeled in an elastic model (gray lines) show that ITD accurately recovers practically the complete elastic record (Figures 7.9b). For very strong attenuation ($Q = 10$; Figure 7.9a), ITD recovers well the reflections above about 700 ms and the stronger reflections from the

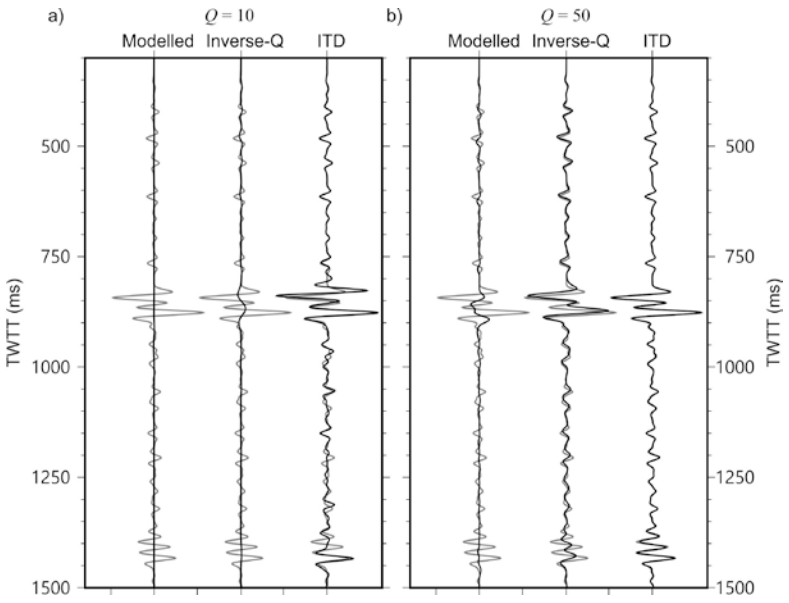

Figure 7.9. Comparisons between the attenuated reflection records modeled in Marmousi II model, its inverse-Q filtered record and ITD-corrected records (black lines, labels). Panels a) and b) correspond to modeled $Q = 10$ and 50, respectively. The identical gray lines in all plots are the models in an elastic structure ($Q = \infty$). All records are scaled equally, and therefore the attenuated records (labels "Modeled") show low amplitudes in these plots, particularly in a).

deeper part of the trace (for example, near 1050, 1150, and 1450 ms) (Figure 7.9a). As expected in section 7.2, with large number pulses in $r(t)$ series (N = 200), the ITD shows no instabilities, requires no regularization, and recovers the elastic waveform with good accuracy.

Compared to inverse-Q filtering the ITD results appear to be preferable in both cases (Figure 7.9a and b). For Q = 50, the quality of inverse-Q correction is good above about 800 ms and reduces with depth (Figure 7.9b). The strong reflection packages near 850–-900 ms and 1400 ms are somewhat under-corrected in amplitudes and shifted in phases. For very strong attenuation the inverse-Q filtering result is unsuccessful (Figure 7.9a). These difficulties in inverse-Q filtering of these records are apparently caused by the selections of the stabilization factor or gain limiting required for suppressing the high-frequency noise. In this low-noise example, this gain limiting could of course be adjusted and results comparable to those of ITD achieved. However, our goal in this example was to illustrate the inverse-Q and ITD filtering with "typical" parameters not tailored for a noise-free case.

7.5 Application to Real Data

To illustrate the ITD method on field seismic data, I apply it to a stacked 2-D seismic line (the owner and location of the data are confidential; Figure 7.10a). The line contains 400 CMPs with two-way travel times ranging from 400 to 5000 ms (Figure 7.10a). Standard 2-D seismic processing was applied to the data, with emphasis on preserving the attenuation characteristics (time-variant spectra) for Q-compensation. The stacked data (Figure 7.10a) show significant attenuation effects, which results in the dominant frequency of about 15 Hz for the whole data. The data are somewhat contaminated with linear large-moveout noise, which can be seen above 1000 ms, around 1500-ms, and below 2500-ms travel times. This

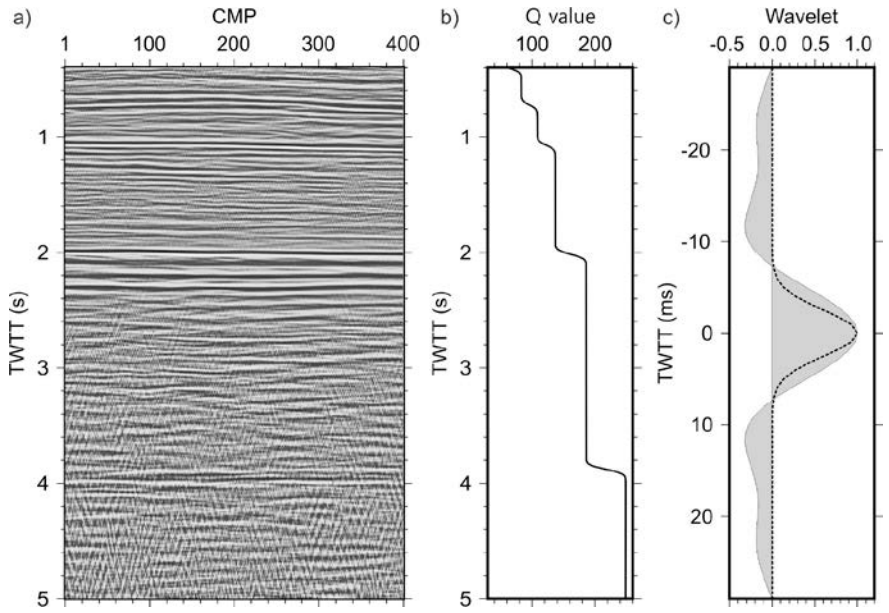

Figure 7.10. Field data example: a) a fragment of stacked real-data section; b) interval Q model at CMP = 200, and c) the estimated wavelet (gray shading) and a simplified Gaussian wavelet (dotted line) used for shaping in ITD.

noise likely arises from slant-filtering of the stacked section in order to enhance near-horizontal reflections. Here, I do not attempt reducing this or any other types of noise and only focus on Q-compensation.

As for many other reflection datasets, no independent measurements of Q are available, and the spatially-variable Q is estimated from seismic-processing velocities by using the following empirical relation (Li, 1993):

$$Q = 14V^{2.2}, \tag{7.17}$$

where V is the interval velocity in km/s. Although this Gardner-type relation is certainly inaccurate, it reproduces the commonly observed positive correlation of seismic velocities with Qs (Zhang and Stewart, 2007). Sharp layering resulting from relation (7.17) was smoothed in accordance with the expected smooth Q variability (section 7.2). A vertical profile of $Q(t_0)$ at the location of CMP = 200 is shown in Figure 7.10b.

Figure 7.11 shows Q-compensation results by using the inverse-Q filtering method

(Wang 2008) and ITD. As described in section 2, the inverse-*Q* filtered records (Figure 7.11a) can be used for estimating the source wavelet for ITD. I estimated a wavelet from the upper part of the section in Figure 7.11a, assuming it to be zero-phase and using the statistical average wavelet estimation method by Oppenheim and Schafer (1975). This wavelet is shown by gray shading in Figure 7.10c. Further, because the *Q* values in the upper portion of the section are relatively low (Figure 7.10b), a significant attenuation is present between the effective "source" zone and the times at which the wavelet was measured. To account for this attenuation, I constructed a simplified Gaussian wavelet (dotted line in Figure 7.10c), which was utilized for ITD.

Figure 7.11 shows that the appearance, resolution, and apparently the SNR of the data section was improved after both inverse-*Q* filtering and ITD. The ITD appears to recover more reflectors and enhance their sharpness, although in the deeper parts of the section, the

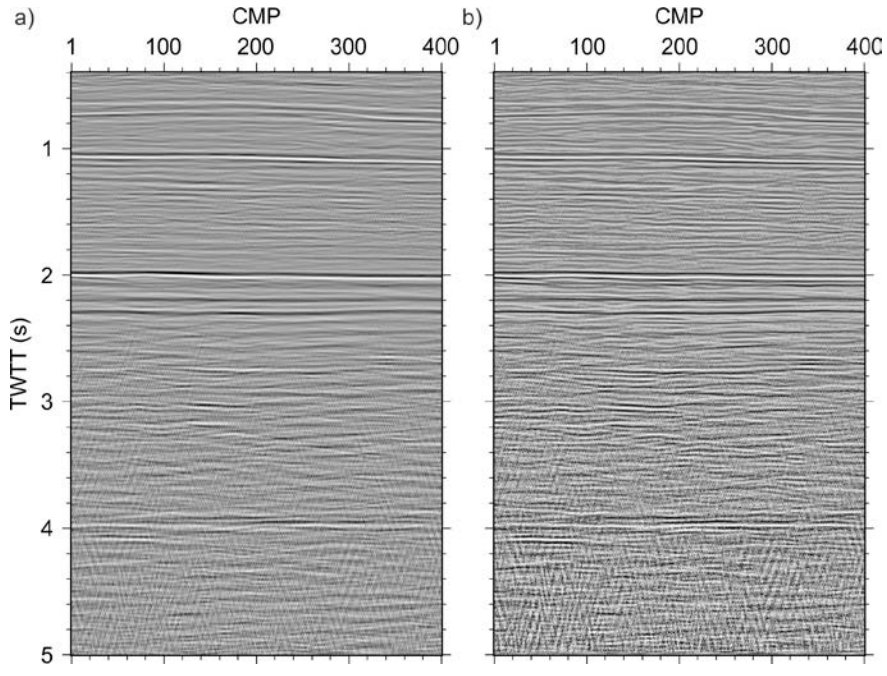

Figure 7.11. A fragment of stacked data section (Figure 7.10a) after corrections by using: a) inverse-*Q* filtering (Wang, 2008), and b) ITD.

intensity of the large-moveout linear noise remains comparable to the original section (Figures 7.11b and 7.10a). Apart from this linear noise, the improvements by ITD compared to inverse-*Q* filtering appear significant throughout the whole section (Figures 7.11a and 7.11b). The reflections in the ITD-filtered section become zero-phase because of the zero-phase wavelet used for deconvolution (Figure 7.10c).

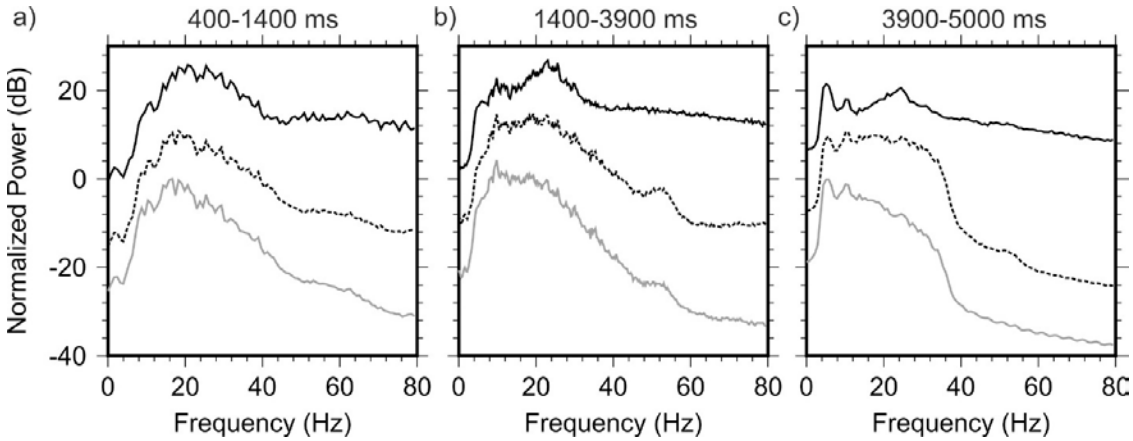

Figure 7.12. Spectra comparison of data before (gray lines) and after (black lines) compensation with depth ranges from a) 400-1400 ms, b) 1400-3900 ms and c) 3900-5000 ms. The black solid lines indicate the spectra measured for ITD compensation while the dashed lines are the spectra measured for inverse-*Q* filtering.

Figure 7.12 compares the average spectra of the data before and after compensation by using inverse-*Q* filtering and ITD. These average spectra are normalized by the peak power of the data before compensation within 400–1400 ms. Prior to *Q*-compensation, the high-frequency components (above about 40 Hz) decay with reflection time faster than the low-frequency components (below about 40 Hz). Consequently, the peak spectral powers are shifted to lower frequencies at increased depths (gray lines in Figure 7.12). Both the inverse-*Q* filtering and ITD boost the frequency components of the attenuated data (black solid and dotted lines in Figure 7.12). For the shallow part (400–1400 ms, Figure 7.12a), inverse-*Q* filtering and ITD achieve similar compensation results in the power spectra. However, it should again be noted that this compensation is achieved differently for these methods: for

inverse-*Q* filtering, it is a result of *Q* correction, but for ITD, this is principally done by selecting the shaping wavelet. At the intermediate and deeper parts of the section (1400 to 5000 ms, Figure 7.12b and c), inverse-*Q* filtering may under-correct the high-frequency components (above 40 Hz), where the SNR is low, and ITD provides a stronger enhancements of the spectra (Figure 7.12b and c). The time-domain images in Figure 7.11 also show that in the intermediate and deeper parts (1400–5000 ms), of the ITD-filtered records reveal more and sharper reflected events, albeit with some enhancement of the high-moveout linear noise.

7.6 Discussion

Selections of time-, frequency- or mixed-domain (such as wavelet-based) deconvolution methods emphasize different aspects of the data and may be significant for the success of deconvolution. The conventional inverse-*Q* filtering is performed in frequency domain, so that each frequency component of the data is restored independently. However, for long enough wave propagation, the highest-frequency components can become lost in noise and cannot be recovered by inverse-*Q* filtering (Figure 7.1b). By contrast, due to its time-domain (or wavelet-based) algorithm (eqs. (7.10) and (7.11)) the ITD method detects reflections principally by their dominant-frequency components. Thus, the ITD operates in the most advantageous part of the spectrum and has lower sensitivity to frequencies at which signal is weak. By identifying the time of the signal, this method is able to recover all frequency components (Figures 7.1c and 7.1d). At the same time, the ITD makes no selective use of any frequencies, and consequently it is stable and does not boost high-frequency noise.

The principal advantage of ITD is due to the fact that this algorithm focuses on recovering the strongest reflections first, but if necessary, the entire waveform can be

transformed (by taking large cutoff values N). The ITD looks for the highest similarity of the recorded signals with the propagating source waveforms. Such similarity is expected from true reflections and not expected from (random) noise. By contrast, the inverse-Q filtering does not differentiate the signal from noise, and consequently always boosts and phase-shifts the high-frequency noise.

Although offering some advantages over the frequency-domain inverse-Q filtering, the ITD also has some limitations when applied to low-SNR data. As shown in Figures 7.4 and 7.5, in cases where the inverse-Q filtering strongly boosts noise (low Q and/or low SNR), ITD images can contain noise in the form of spurious random reflectivity (Figures 7.4b and 7.5b). This effect is of course unavoidable in a single-channel record, where weak (attenuated) reflection waveforms cannot be differentiated from strong noise. However, with multichannel recording and data processing, the SNR can be improved by various techniques (such as slant filtering or f-x deconvolution), before or after applying the Q-compensation. In addition, as a time-domain waveform processing method, the ITD can readily be extended to fully multichannel operation.

Although the ITD requires an estimate of the source wavelet, such estimates can be produced in seismic processing. Assuming randomness of the reflectivity and zero phase of the wavelet, a statistical wavelet can be derived from the autocorrelation of the recorded data (Clayton and Wiggins 1976; Yilmaz 2001). By tying seismic data to well logs, the phase and amplitude spectrum of the wavelet can be further adjusted (Walden and White 1984). Stone (1984) reviewed several approaches for estimating the phase of the wavelet from seismic data alone based on statistical models of reflectivity. Recently, van der Baan and Pham (2008) and Berkhout and Verschuur (2011) proposed further developments of these

methods, and Edgar and van der Baan (2011) compared them with well-log guided deconvolution. All of the above methods derive stationary wavelets that remain invariant through the data record. In the presence of attenuation, this requirement of stationarity is not satisfied; however, the source wavelet becomes stationary *after* a correction for attenuation. Therefore, to derive a source wavelet for ITD corrections, I propose to: 1) perform iterative analysis starting from an initial wavelet estimated by one of the methods above, 2) repeat the determination of the source wavelet after ITD filtering, and 3) repeat both steps until a consistent estimate of the wavelet is obtained. Because attenuation effects are usually relatively weak, this iteration should converge in 2−3 steps. A simple example of such estimation was given in section 7.4.

Although playing similar roles in seismic data processing, the ITD is conceptually different from inverse-*Q* filtering. The ITD can be described as adaptive signal detection rather than correcting for the *Q*-factor in the model. In inverse-*Q* filtering, the high-frequency components of noise are taken as signal and become amplified. Stabilization and gain limiting reduce this noise amplification (Wang, 2008; van der Baan, 2012), but it also reduces the accuracy of *Q*-compensation and makes it approximate. In ITD, the restriction on the number of iterations similarly reduces the accuracy of waveform matching, but this reduction is not for stabilization but for promoting identification of stronger reflections. A significant portion of the noise (especially incoherent one) is rejected by ITD because it does not match the source waveform (Figure 7.4). Because of looking for the strongest events first, the major events are secured early in the processing and weaker secondary events can be filtered out on processor's demand. Compared to frequency-domain methods (such as inverse-*Q* filtering), this may be a major advantage of time-domain waveform decomposition

methods. This advantage appears to be most important and analogous to the advantage of τ-p filtering over f-k.

The numerical experiments with inaccurate Qs and source waveforms (section 3) show that accurate dispersion relations are required in order to constrain detailed structures. As in any other seismic processing method, Q-compensation cannot exceed the resolution limits imposed by the bandwidth of seismic data and by limited knowledge of the subsurface structure. However, the character of uncertainties and noise in the images produced by inverse-Q filtering and ITD are different, which may be useful in interpretation. Inverse-Q filtering and other frequency-domain methods are insensitive to the shape of the source wavelet but rely on accurate models of Q and dispersion relations which may be difficult to measure from the data. Such accurate Q models may not even exist *ab initio* (Morozov and Baharvand Ahmadi, 2015). Frequency-domain methods are also prone to boosting noise and exhibiting instabilities at high-frequencies, and may sometimes increase ringiness of the sections. By contrast, the ITD is stable, less sensitive to model uncertainties, and its noise has the appearance of misdetected reflections rather that increased high-frequency waveforms. Generally, it appears best using a combination of such methods, as in the examples in this paper.

7.7 Conclusions

In this Chapter, I presented a case for using a broad class of time-variant, time-domain deconvolution methods for Q-compensation of reflection seismic records. In particular, a simple scheme called the iterative time-domain deconvolution (ITD) appears to offer a number of unique advantages. A series of numerical experiments are conducted to evaluate the performance of ITD. Tests on noise-contaminated data suggest that compared to

inverse-Q filtering, ITD is stable and has the ability to filter out the noise. By virtue of its time-domain operation, the ITD can increase the sparseness of the Q-compensated images, which may be an attractive feature for interpretation. ITD is performed on a trace-by-trace basis, and consequently it can be used in both post- and pre-stack processing and potentially included in migration. The method is illustrated on numerical examples and real data. Numerical experiments show that ITD is relatively weakly sensitive to inaccurate attenuation and velocity models. For example, with $Q \approx 50$, ITD can tolerate about ±40% errors in Q with or without noise in the data. Because ITD requires an estimate of the source wavelet, I recommend combining this method with inverse-Q filtering and wavelet estimation.

CHAPTER 8

CONCLUSIONS AND RECOMMENDATIONS FOR FUTURE RESEARCH

The principal goals of this dissertation were: 1) to study several attenuation mechanisms by using rigorous, physics-based wave-propagation models, 2) to study one aspect of measurement of Q related to the equivalence of scattering and viscoelastic attenuation, and also 3) to develop a pure time-domain deconvolution method for correcting for effects of attenuation in seismic records. All three of these topics were novel and yet unexplored in the existing literature. The analysis was based on the new, very broad framework of the General Linear Solid (GLS; Morozov and Deng, 2016a, b), which was applied to viscoelastic and poroelastic media, poroelastic media with squirt flows, and visco-poroelastic media. Within the framework of GLS, I developed the concept of solid viscosity for bitumen sands and estimated nonlinear elastic and viscous properties for very viscous materials. In addition to inelasticity, I also studied several typical elastic structures that may cause seismic-wave attenuation and dispersion.

In the following, I present two groups of conclusions related to the general methodology (GLS; section 8.1) and also to the practical results from several models developed in this dissertation (section 8.2). None of the three research areas was (or possibly could be) explored comprehensively in this short study. Following the conclusions, Section 8.3 therefore outlines some unsolved questions and promising directions of further research based on the concept of GLS and on the proposed attenuation modeling and compensation methods.

8.1 Methodological Conclusions from this Study

1) The most basic methodological conclusion of this dissertation is that Lagrangian continuum mechanics (the GLS formulation; Chapter 3) allows rigorous and compact derivations of macroscopic equations of motion for all practical cases in seismology:
    a) All conventional linear viscoelastic models, such as the Standard Linear Solid (SLS), Maxwell's and Kelvin-Voigt solids, and also the Generalized Standard Linear Solid (GSLS);
    b) Biot's poroelastic model, and its extensions to multiple porosities and partial saturation. Specifically, I extended Biot's poroelasticity to create several new models of squirt flows within sandstone.
2) Based on the GLS framework, I also extended the SLS to include internal inertial effects and explored some of its properties.
3) By combining the Lagrangian model of the SLS with poroelasticity, I obtained a model that I called visco-poroelasticity, and also apply it to modeling of squirt flows.
4) Squirt-flow effects can also be modeled by a different type of a GLS model. Rather than considering additional internal variables, the internal friction within rock (such as caused by squirt flows and bitumen effects) can be modeled by the effects of solid viscosity of the rock frame.

8.2 Practical (Applied) Conclusions

The general methodological results listed in section 8.1 were applied to several practical problems of laboratory and field seismology. Their key results are briefly as follows:

1) Based on the time-domain GLS formulation, a finite-difference scheme for modeling attenuative seismic waveforms was developed (Appendix A). This scheme uses no

mathematical “memory variables” and does not require specification of *Q* spectra.

2) Physical interpretations were found for the “memory variables” and “material memory” broadly used in time-domain viscoelastic models of materials. In contrast with the conventional methodology which considers memory variables only as a mathematical instrument, these variables were shown to represent actual physical internal variables corresponding to certain physical properties or macroscopic heterogeneity of the medium. Lagrangian formulations were given for the macroscopic mechanics of these variables.
3) A solid-viscosity model was proposed, which represented an extension of Biot’s poroelasticity consistent with most existing squirt-flow models.
4) For a very viscous material such as heavy oil or Crisco (vegetable shortening) used as its proxy in some lab experiments (Chapter 5), the behavior of the material may be nonlinear near the source or at the edge of a linear zone. For large strains and/or strain rates the moduli and viscosity can be considered as strain and strain-rate dependent. This nonlinearity gives us a very good explanation for the experimental data with Crisco.
5) The observed wave attenuation and dispersion may not only be due to the inelasticity of the material, but certain elastic structures can also produce such effects. In particular, there exists a fundamental equivalence between the phenomenological *Q* inferred from reflection observations and fine elastic layering (Chapter 6).
6) Based on any GLS-based model of wave propagation and multiple deconvolution approaches, an effective and flexible algorithm for compensating attenuation effects in reflection seismic data can be formulated. In particular, a numerical scheme based

on iterative time-domain deconvolution (ITD) offers improved resolution and additional image enhancements (Chapter 7). This method is less sensitive to noise and inaccurate Q models. With increasing numbers of iterations, ITD also become less dependent on the selected source wavelet. These advantages make ITD a practical and efficient method for attenuation compensation.

8.3 Directions of Future Research

Because of the fundamental and novel concept of GLS lying at its basis, this study of seismic attenuation mechanisms and compensation leads to numerous extensions and applications. Because of time and resource limitations, these subjects could not be included in this dissertation. Seismic attenuation and dispersion data are limited, and they typically cannot definitively point to only one attenuation mechanism. One needs to consider multiple possibilities while taking into account the effects of observational procedures such as the dimensions of the samples and boundary conditions used in laboratory experiments. For performing such detailed modeling of field and laboratory experiments, Lagrangian mechanics (i.e., the GLS framework) seems to be by far the most appropriate tool.

Several directions of such modeling of laboratory experiments follow from the present study. Some of these directions are already being explored in recently submitted manuscripts and papers in preparation, and approaches to others still need to be created:

1) Elastic potential and dispersion of elastic moduli in fluid-saturated rock with double porosity, (Morozov and Deng, Geophysics, in review). To date, in squirt-flow models, the velocity dispersion caused by soft pores is explained applying “Betti’s reciprocal theorem” and Gassmann’s equation to viscoelastic (VE) moduli at nonzero frequency. The GLS model explains this dispersion accurately and actually reveals that the

existing VE model is of limited accuracy.

2) To date, subresonant laboratory experiments with rock samples are only loosely interpreted in terms of frequency-dependent *Q*s, VE moduli, and standard solids (e.g., Jackson and Paterson, 1993; Spencer, 2013; Spencer and Shine, 2016; Pimienta et al., 2015a, b, 2016a). It appears that the concept of wave-induced flows (WIFF) could be the most general and suitable for modeling such experiments. The elastic-potential and GLS framework allow performing such modeling rigorously and with an account for all details of the experimental apparatus (Morozov, 2015; Morozov, Geophysics, in review). Such modeling is currently underway for the recent experiments by Pimienta et al. (2015b) (Morozov and Deng, *Geophysics*, in preparation 1 and 2). Recent results (Morozov, 2015; Morozov, Geophysics, in review) generally show that such interpretations are much more specific and detailed, and they are often far from the conventional *Q*-based models. Many other experiments with sandstones and bitumen sands need to be modeled in similar ways.

3) The model of squirt flows proposed by Deng and Morozov (2016) (Chapter 4) explains how the existing squirt-flow models are related to macroscopic properties of the material. However, these properties are still phenomenological (frequency-dependent). Therefore, a first-principle mechanical (GLS) model is needed for explaining this phenomenology (Deng and Morozov, Geophysics, in preparation). Such a first-principle model would reveal the true material properties (such as the heterogeneity of the pore space and partial saturation) responsible for squirt-flow effects. In addition to the pure macroscopic (effective-medium) approach by Deng and Morozov (Geophysics, in preparation), a micromechanical Lagrangian model

similar to the existing squirt-flow models also needs to be considered.

4) The model of nonlinear elastic and viscous properties in heavy oil (Chapter 5) appears to be very important methodologically. In particular, it shows that although field seismic data are likely always acquired in the linear regime, laboratory observations may be nonlinear. Seismic frequencies also differ greatly from those used in the laboratory, and consequently comparisons of laboratory observations to field data require accurate theoretical descriptions. Additional laboratory experiments are required in order to validate and improve the theory presented in Chapter 5, and also to determine its parameters, such as the strain threshold ε_0 and the characteristic time τ.

5) Seismic attenuation within crustal and mantle rock was not considered in this study, which focused on internal-friction mechanisms due to free pore fluids. Nevertheless, crustal and mantle attenuation is clearly an immensely important topic containing numerous challenges related to both basic physics and high-pressure and temperature experimental techniques. The existing approaches to seismic-wave attenuation within the mantle (e.g., Dziewonski and Anderson, 1981) and mantle-rock samples (e.g., Jackson and Paterson, 1993) are based exclusively on assuming a frequency-dependent (and also pressure- and temperature-dependent) Q factor. From the viewpoint of the approach of this dissertation, this model is insufficient, and a physics-based model needs to be sought. However, the GLS approach appears to be applicable to arbitrary conditions (Coulman et al., 2013).

6) A finite-difference modeling scheme was only developed as a “pilot” 1-D illustration in this dissertation (Appendix A). Development of a production-quality algorithm for

modeling 3-D wavefield in media with solid viscosity and single or multiple porosities is required. Such an algorithm would allow realistic modeling of seismic wavefields in complex media with arbitrary boundary conditions and without assumptions about hypothetical properties such as "material *Q*". This topic could be extremely important, because seismic waveform modeling is routinely conducted in all areas of seismology and yet the differential equations used in their finite-difference schemes still rely on the hypothetical material properties such as the *Q*-factor and material memory.

7) The algorithm for attenuation-compensation by using the ITD or other types of time-domain deconvolution can and should be developed further and applied to other real datasets. Promising potential enhancements of this algorithm could include multichannel identification of reflected waveforms, applications to pre-stack data and pre-stack migration, and estimation of *Q* and source wavelet.

8) The analysis of the trade-off between the *Q* measured from a reflection section and thin (sub-wavelength) layering within it (Chapter 7) also needs to be explored further. This problem is related to the contrast between the conventionally-used models of seismic *Q* that is often layered (and possessing sharp variations of *Q*) and smooth *Q* models recommended by Morozov and Baharvand Ahmadi (2015). This contrast in interpretational style and its effects on geologic interpretations needs to be further explored on more realistic examples and real seismic data.

LIST OF REFERENCES

Aki, K., and B. Chouet, 1975, Origin of coda waves: source, attenuation, and scattering effects: J. Geophys, Res. 80, 3322–3342, doi: 10.1029/JB080i023p03322

Aki, K., 1980, Scattering and attenuation of shear waves in the lithosphere: J. Geophys. Res., 85, 6496–6504, doi: 10.1029/JB085iB11p06496

Aki, K., and P. G. Richards, 2002, Quantitative seismology, 2nd Edition: University Science Books.

Al-Shukri, H. J., G. L. Pavlis and F. L. Vernon, 1995, Site effect observations from broadband arrays: Bulletin of the Seismological Society of America, 85, 1758−1769.

Berkhout, A. J., and D. J. Verschuur, 2011, A scientific framework for active and passive seismic imaging, with applications to blended data and micro-earthquake responses: Geophysical Journal International, **184**, 777–792, doi: 10.1111/j.1365-246X.2010.04855.x

Berryman, J. G., and H. F. Wang, 2000, Elastic wave propagation and attenuation in a double-porosity dual-permeability medium: International Journal of Rock Mechanics and Mining Sciences, **37**(1), 63-78.

Bickel, S., and R. Natarajan, 1985, Plane-wave *Q* deconvolution: Geophysics, **50**(9), 1426-1439.

Biot, M. A., 1956, Theory of propagation of elastic waves in a fluid-saturated porous solid. I. Low-frequency range: Journal of the Acoustical Society of America, **28**, 168 – 178, doi: 10.1121/1.1908239.

Beresnev, I. A., 2014, Compressional-wave propagation in porous media saturated with two fluids: Geophysics, **79**(1), L1–L11.

Blanch, J. O., J. O. Robertsson, and W. W. Symes, 1995, Modeling of a constant Q: Methodology and algorithm for an efficient and optimally inexpensive viscoelastic technique. Geophysics, **60**(1), 176–184.

Bohlen, T., 2002, Parallel 3-D viscoelastic finite difference seismic modelling: Computers & Geosciences, **28**, 887–899.

Bonar, D. C., M. D. Sacchi, 2010, Complex spectral decomposition via inversion strategies, SEG Denver 2010 Annual Meeting, Denver, doi: 10.1190/1.351310

Bourbié, T., O. Coussy, and B. Zinsiger, 1987, Acoustics of porous media: Editions Technip, Paris, France.

Bouzidi, Y., and D. R. Schmitt, 2009, Measurement of the speed and attenuation of the Biot slow wave using a large ultrasonic transmitter: Journal of Geophysical Research: Solid Earth, **114**(B8).

Carcione, J. M. 1993, Seismic modeling in viscoelastic media. Geophysics, **58**, 110–110.

Carcione, J. M., 1998, Viscoelastic effective rheologies for modelling wave propagation in porous media: Geophysical prospecting, **46**(3), 249–270.

Carcione, J. M., and S. Picotti, 2006, P-wave seismic attenuation by slow-wave diffusion: Effects of inhomogeneous rock properties. Geophysics, **71**(3), O1–O8.

Carcione, J.M., 2007, Wave fields in real media: Wave propagation in anisotropic anelastic, porous, and electromagnetic media, Second Edition, Elsevier, Amsterdam.

Carcione, J., and B. Gurevich, 2011, Differential form and numerical implementation of Biot's poroelasticity equations with squirt dissipation: Geophysics, **76**(6), N55–N64, doi: 10.1190/GEO2010-0169.1.

Carcione, J., 2014, Wave fields in real media: Wave propagation in anisotropic, anelastic, porous and electromagnetic media. 3rd ed, **38**: Elsevier Science, ISBN: 9780080999999

Chapman, M., 2003, Frequency-dependent anisotropy due to meso-scale fractures in the presence of equant porosity. Geophysical Prospecting, **51**(5), 369–379.

Clayton, R.W., and R. A. Wiggins, 1976, Source shape estimation and deconvolution of teleseismic body waves: Geophys. J. R. astr. Soc., **47**, 151–177.

Coulman, T., W. Deng, and I. B. Morozov, 2013, Models of seismic attenuation measurements in the laboratory: Canadian Journal of Exploration Geophysics: **38**, 51–67. Dasgupta, R. and R. A. Clark, 1998, Estimation of Q from surface seismic reflection data. Geophysics, **63**, 2120−2128.

Day, S. M., J. Minster, and H. Xu, 1998, Numerical Modeling of Linear and Nonlinear Seismic Wave Attenuation. Scripps Institution of Oceanography La Jolla Ca.

Deng, W., and I. B. Morozov. 2014, Nonlinear seismic wave propagation in heavy oil: GeoConvention 2014, Calgary, Canada, http://www.geoconvention.com/archives/2014/150_GC2014_Nonlinear%20Modeling%20for%20Heavy%20Oil.pdf

————————, 2016, Solid viscosity of fluid-saturated porous rock with squirt flows at seismic frequencies, Geophysics: **81**(4), D381–D390.

————————, 2017, Trade-off of elastic structures with interpretation of seismic

attenuation: Pure and Applied Geophysics, doi: 10.1007/s00024-017-1581-3.

————————, Seismic-Q compensation by iterative time-domain deconvolution: *Geophysical Prospecting*, in revision

————————, Macroscopic mechanics of porous rock with local fluid flows, *Geophysics*, in preparation.

————————, Double-porosity models for squirt flows in sandstone, *Geophysical Prospecting*, in preparation.

Dutta, N., and H. Odé., 1979, Attenuation and dispersion of compressional waves in fluid-filled porous rocks with partial gas saturation (White model)-Part I: Biot theory. Geophysics, **44**(11), 1777–1788.

Dvorkin, J., and A. Nur, 1993, Dynamic poroelasticity: A unified model with the squirt and the Biot mechanisms: Geophysics, **58**, 524–533, doi: 10.1190/1.1443435.

Dvorkin, J., R. C. Nolen-Hoeksema, and A. Nur, 1994, The squirt-flow mechanism; macroscopic description: Geophysics, **59**(3),428–438.

Dvorkin, J., G. Mavko, and A. Nur, 1995, Squirt flow in fully saturated rocks: Geophysics, **60**, 97–107, doi: 10.1190/1.1443767.

Dziewonski, A. M., and D. L. Anderson, 1981.. Preliminary Reference Earth Model (PREM), Phys. Earth Planet. Inter. **25**, 297–356.

Edgar, J. A., and M. van der Baan, 2011, How reliable is statistical wavelet estimation?: Geophysics, **76**(4), V59–V68.

Eshelby, J. D., 1957, The determination of the elastic field of an ellipsoidal inclusion and

related problems: Proc. Roy. Soc. London, Series A, 241, 376–396, doi: 10.1098/rspa.1957.0133.

Fuchs, K., and G. Müller, 1971, Computation of synthetic seismograms with the reflectivity method and comparison with observations: Geophysical Journal International, **23**(4), 417–433.

Futterman, W. I., 1962, Dispersive body waves: Journal of Geophysical Research, 67, 5279–5291, doi: 10.1029/JZ067i013p05279.

Gardner, G., L. Gardner and A. Gregory, 1974, Formation velocity and density—The diagnostic basics for stratigraphic traps: Geophysics, **39**(6),770–780.

Gochioco, L. M., 1991, Tuning effect and interference reflections from thin beds and coal seams, Geophysics, **56**(8), 1288-1295, doi: 10.1190/1.1443151.

Graves, R.W., 1996, Simulating seismic wave propagation in 3-D elastic media using staggered-grid finite difference: Bulletin of the Seismological Society of America, **86**, 1091–1106.

Gurevich, B., D. Makarynska, M. Pervukhina, and O. De Paula, 2010, A simple model for squirt-flow dispersion and attenuation in fluid-saturated granular rocks: Geophysics, **75**(6), N109–N120, doi: 10.1190/1.3509782.

Hale, D., 1981, An inverse *Q*-filter: Stanford Exploration Project, **28**(1), 289–298.

Han, L., Liu, C., 2015. Can we use wavelet phase change due to attenuation for hydrocarbon detection?: 85th Annual International Meeting, SEG, Expanded Abstracts: 2962–2966, doi: 10.1190/segam2015-5890451.1

Hargreaves, N. D., and A. J. Calvert, 1991, Inverse Q filtering by Fourier transform: Geophysics, **56**(4), 519–527.

Jackson, I., and M.S. Paterson, 1993, A high-pressure, high-temperature apparatus for studies of seismic wave dispersion and attenuation: Pure and Applied Geophysics, 141 (2/3/4), 445–466, doi: 10.1007/978-3-0348-5108-4_12

Jones, T. and A. Nur, 1983, Velocity and attenuation in sandstone at elevated temperatures and pressures: Geophysical Research Letters **10** (2), 140–143, doi: 10.1029/GL010i002p00140.

Kikuchi, M., and H. Kanamori, 1982, Inversion of complex body waves: Bulletin of the Seismological Society of America, **72**(2), 491–506.

Kjartansson, E., 1979. Constant Q-wave propagation and attenuation: Journal of Geophysical Research 84, 4737–4748, doi: 10.1029/JB084iB09p04737

Knopoff, L., 1964, *Q*, Rev. Geophys., 2, 625–660.

Kuteynikova, M., N. Tisato, R. Jänicke, and B. Quintal, 2014, Numerical modeling and laboratory measurements of seismic attenuation in partially saturated rock: Geophysics, **79**(2), L13–L20.

Lakes, R., 2009, Viscoelastic materials: Cambridge Univ. Press, ISBN 978-0-521-88568-3.

Landau, L., and E. Lifshitz, 1986, Theory of elasticity: Pergamon Press, Oxford.

————1987, Fluid mechanics: Pergamon Press, Oxford.

Levander, A.R., 1988, Fourth-order finite-difference PW seismograms: Geophysics **53**(11), 1425–1436, doi: 10.1190/1.1442422.

Li, Q., 1993, The way to high precision exploration: Petroleum Industry Press, Beijing. ISBN 9787502109967. (*in Chinese*)

Ligorría, J. P., and C. J. Ammon, 1999, Iterative deconvolution and receiver-function estimation: Bulletin of the seismological Society of America, **89**(5): 1395–1400.

Lines, L., Vasheghani, F., Treitel, S. 2008. Reflections on Q, CSEG Recorder 34: 36–38.

Lines, L., Wong, J., Innanen, K., Vasheghani, F., 2014. Research note: Experimental measurements of Q-contrast reflections, Geophysical Prospecting, **62**, 190–195, doi: 10.1111/1365-2478.12081

Lo, W. C., G. Sposito, and E. Majer, 2005, Wave propagation through elastic porous media containing two immiscible fluids: Water Resources Research, **41**, W02025.

Masson, Y., S. Pride, and K. Nihei, 2006, Finite difference modeling of Biot's poroelastic equations at seismic frequencies: Journal of Geophysical Research: Solid Earth, **111**(B10305), doi:10.1029/2006JB004366.

Masson, Y. J., and S. R. Pride., 2007, Poroelastic finite difference modeling of seismic attenuation and dispersion due to mesoscopic-scale heterogeneity: Journal of Geophysical Research: Solid Earth, **112**(B3).

Margrave, G. F., 1998, Theory of nonstationary linear filtering in the Fourier domain with application to time-variant filtering: Geophysics, **63**, 244−259.

Martin, G. S., R. Wiley, and K. J. Marfurt., 2006, Marmousi2: An elastic upgrade for Marmousi: The Leading Edge, **25(**2), 156–166.

Mavko, G., and A. Nur., 1979, Wave attenuation in partially saturated rocks: Geophysics,

44(2), 161–178.

Mavko, G., and D. Jizba, 1991, Estimating grain-scale fluid effects on velocity dispersion in rocks: Geophysics, **56**, 1940–1949, doi: 10.1190/1.1443005.

Mavko, G., 2013, Relaxation shift in rocks containing viscoelastic pore fluids: Geophysics, 78(3), M19–M28.

Minster, J. B., S. M. Day, and P. M. Shearer., 1991, The transition to the elastic regime in the vicinity of an underground explosion: American Geophysical Union, **65**, 229–238.

Morozov, I. B., 2010, On the causes of frequency-dependent apparent seismological Q: Pure and Applied Geophysics, **167**, 1131–1146, doi 10.1007/s00024-010-0100-6.

———— Models of seismic-frequency laboratory experiments with porous rock cylinders, Geophysics, in review

————2015, Effective moduli and Poisson's ratios in poroelasticity: Canadian Journal of Exploration Geophysics, **40**, 21–34.

Morozov, I. B. and A. Baharvand Ahmadi, 2015. Taxonomy of *Q*: Geophysics **80**(1): T41–T49, doi: 10.1190/GEO2013-0446.1

Morozov, I. B., and W. Deng, 2016a. Macroscopic framework for viscoelasticity, poroelasticity and wave-induced fluid flows – Part I: General Linear Solid: Geophysics, **81**(1), L1-L13, doi: 10.1190/GEO2014-0171.1.

————2016b, Macroscopic framework for viscoelasticity, poroelasticity, and wave-induced fluid flows—Part 2: Effective media: Geophysics, **81**(4), D405–D417.

————, Elastic potential and dispersion of elastic moduli in fluid-saturated rock with

double porosity, Geophysics, in revision

————————, Biot-consistent mechanics of wave-induced fluid flows: I. Effective moduli, *Geophysics*, in preparation 1.

————————, Biot-consistent mechanics of wave-induced fluid flows: II. Lagrangian model, *Geophysics*, in preparation 2.

Morozov, I. B., W. Deng, and L. Lines, Ultrasonic wave propagation and reflections in "heavy oil" (Crisco), submitted to *Canadian Journal of Exploration Geophysics*

Morozov I.B., M. Haiba, and W. Deng W., Inverse attenuation filtering, *submitted to Geophysics, in review.*

Morse, P. M., and H. Feshbach, 1953, Methods of Theoretical Physics Part I: MacGraw Hill, ISBN: 0976202123.

Müller, T., B. Gurevich, and M. Lebedev, 2010, Seismic wave attenuation and dispersion resulting from wave-induced flow in porous rock – A review: Geophysics, **75**(5), 75A147–75A164, doi: 10.1190/1.3463417.

Murphy, W. F., K. W. Winkler, and R. L. Kleinberg, 1986, Acoustic relaxation in sedimentary rocks, dependence on grain contacts and fluid saturation: Geophysics, **51**, 757–766, doi: 10.1190/1.1442128.

Murphy, W. F. 1982, Effects of partial water saturation on attenuation in Massilon sandstone and Vycor porous glass: The Journal of the Acoustical Society of America, **71**(6), 1458–1468.

Nocedal, J. and S. J. Wright, 2000, Numerical Optimization. 2rd edition: Springer, ISBN-10:

0-387-30303-0

O'Connell, R., and B. Budiansky, 1977, Viscoelastic properties of fluid-saturated cracked solids: Journal of Geophysical Research, **82**, 5719–5735, 10.1029/JB082i036p05719.

O'Doherty, R., Anstey, N. A., 1971. Reflections on amplitudes, Geophysical Prospecting **19**(3): 430–458, doi: 10.1111/j.1365-2478.1971.tb00610.x

Oppenheim, A.V., and R.W. Schafer, 1975, Digital signal processing: Prentice-Hall, Inc., Englewood Cliffs, NJ, 584 pp., ISBN: 0-13-214635-5

Pimienta, L., J. Fortin and Y. Guéguen, 2015a, Experimental study of Young's modulus dispersion and attenuation in fully saturated sandstones: Geophysics, **80**(5), L57–L72, doi: 10.1190/geo2014-0532.1

——————————— 2015b, Bulk modulus dispersion and attenuation in sandstones. Geophysics, **80**(2), D111−D127, doi: 10.1190/geo2014-0335.1

Pimienta, L., J. Borgomano, J. Fortin and Y. Guéguen, 2016, Modelling the drained/undrained transition: effect of the measuring method and the boundary conditions: Geophysical Prospecting, **64**(4),1098−1111.

Partyka G., Gridley, J., Lopez, J., 1999. Interpretational applications of spectral decomposition in reservoir characterization. The Leading Edge: 353-360.

Plona, T. J., 1980, Observation of a second bulk compressional wave in a porous medium at ultrasonic frequencies, Applied Physics Letters, **36**(4), 259–261.

Pride, S.R., J.G. Berryman, and J.M. Harris, 2004, Seismic attenuation due to wave-induced flow: Journal of Geophysical Research: Solid Earth, **109**(B1), 1978–2012, doi:

10.1029/2003JB002639.

Quan, Y., J. M. Harris, 1997. Seismic attenuation tomography using the frequency shift method: Geophysics **62**, 895–905

Quintal, B., H. Steeb, M. Frehner, S. M. Schmalholz, and E. H. Saenger., 2012, Pore fluid effects on S-wave attenuation caused by wave-induced fluid flow: Geophysics, **77**(3), L13–L23.

Quintal, B., J. G. Rubino, E. Caspari, and K. Holliger, 2016, A simple hydromechanical approach for simulating squirt-type flow: Geophysics, **81**(4), D335-D344.

Reine C., R. Clark, and M. van der Baan, 2012, Robust prestack Q-determination using surface seismic data: Part 1 — Method and synthetic examples: Geophysics, **77**(1), R45–R56, doi: 10.1190/geo2011-0073.1.

Richards, P.G., and W. Menke, 1983, The apparent attenuation of a scattering medium: Bulletin of the Seismological Society of America, **75**, 1005–1021.

Ricker N., 1941. A note on the determination of the viscosity of shale from the measurement of wavelet breadth: Geophysics, **6**, 254–258, doi: 10.1190/1.1443722.

Ricker, N., 1953, The form and laws of propagation of seismic wavelets: Geophysics **18**, 10–40, doi: 10.1190/1.1437843

Rubino, J., J. E. Santos, S. Picotti, and J. M. Carcione, 2007, Simulation of upscaling effects due to wave-induced fluid flow in Biot media using the finite-element method: Journal of Applied Geophysics, **62**(3),193–203.

Rubino, J. G., C. L. Ravazzoli, and J. E. Santos, 2009, Equivalent viscoelastic solids for

heterogeneous fluid-saturated porous rocks: Geophysics, **74**(1), N1–N13, doi: 10.1190/1.3008544.

Rubino, J. G., and K. Holliger, 2013, Research note: Seismic attenuation due to wave-induced fluid flow at microscopic and mesoscopic scales: Geophysical Prospecting, **61**, 882–889.

Sahay, P. N., 2008, On the Biot slow S-wave: Geophysics, **73**(4), N19–N33, doi: 10.1190/1.2938636

Savage, J., 1966, Thermoelastic attenuation of elastic waves by cracks: Journal of Geophysical Research, **71**(16), 3929–3938.

Shapiro, S. A., 2003, Elastic piezosensitivity of porous and fractured rocks: Geophysics, **68**, 482–486, doi: 10.1190/1.1567215.

Sheriff, R. E., and L. P. Geldart., 1995, Exploration seismology: Cambridge university press, ISBN 0-521-46282-7.

Sheriff, R. E., 2002, Encyclopedic Dictionary of Applied Geophysics Geophysical References Series: Society of Exploration Geophysicists, ISBN (online) 978-1-56080-296-9.

Sleep, N. H., and N. Nakata, 2017, Nonlinear attenuation of S waves by frictional failure at shallow depths: Bulletin of the Seismological Society of America, doi: 10.1785/0120160334.

Spencer, J. W., 2013, Viscoelasticity of Ells River bitumen sand and 4D monitoring of thermal enhanced oil recovery processes: Geophysics, **78**(6), D419–D428, doi: 10.1190/GEO2012-0535.1

Spencer, J. W., and J. Shine, 2016, Seismic wave attenuation and modulus dispersion in sandstones. Geophysics, **81**(3), D211–D231.

Spies, B. R., and D. E. Eggers, 1986, The use and misuse of apparent resistivity in electromagnetic methods: Geophysics, **51**(7), 1462–1471.

Stone, D. G., 1984, Wavelet estimation: Proceedings of the IEEE, 72(10), 1394–1402.

Thomsen, L., 1985, Biot-consistent elastic moduli of porous rocks: low frequency limit: Geophysics, **50**, 2797–2807, doi: 10.1190/1.1441900.

Tisato, N., and B. Quintal. 2013, Measurements of seismic attenuation and transient fluid pressure in partially saturated Berea sandstone: evidence of fluid flow on the mesoscopic scale: Geophysical Journal International, 195, 342–351, doi: 10.1093/gji/ggt259.

Tisato, N., B. Quintal, S. Chapman, C. Madonna, S. Subramaniyan, M. Frehner, E. H. Saenger, and G. Grasselli, 2014, Seismic attenuation in partially saturated rocks: Recent advances and future directions: The Leading Edge, **33**(6), 640–646, doi: 10.1190/tle33060640.1

Tonn, R., 1991, The determination of the seismic quality factor Q from VSP data: a comparison of different computational methods: Geophysical Prospecting **39**, 1–27, doi: 10.1111/j.1365-2478.1991.tb00298.x

van der Baan, M., and D.T. Pham, 2008, Robust wavelet estimation and blind deconvolution of noisy surface seismics: Geophysics, **73**(5), V37–V46.

van der Baan, M., 2012, Bandwidth enhancement: Inverse Q filtering or time-varying Wiener

deconvolution?: Geophysics, **77**(4), V133–V142.

Varela, C. L., A. L. Rosa, and T. J. Ulrych, 1993, Modeling of attenuation and dispersion: Geophysics, **58**(8),1167–1173.

Walden, A. T., and R. E. White, 1984, On errors of fit and accuracy in matching synthetic seismograms and seismic traces: Geophysical Prospecting, **32**, 871–891.

Walsh, J., 1966, Seismic wave attenuation in rock due to friction: Journal of Geophysical Research, **71**(10), 2591–2599.

Wang, Y., 2008, Seismic inverse Q filtering: Blackwell, ISBN 978-1-4051-8540-0.

Wang, S., Yang, D., Li, J., Song, H, 2015. *Q* factor estimation based on the method of logarithmic spectral area difference: Geophysics **80**(6), V157–V171, doi: 10.1190/geo2014-0257.1

White, J. E., Mikhaylova, N. G., Lyakhovitsky, F.M., 1975. Low-frequency seismic waves in fluid-saturated layered rocks: The Journal of the Acoustical Society of America, **57**(S1), S30-S30, doi: 10.1121/1.1995164

White, J. E., 1986, Biot-Gardner theory of extensional waves in porous rods: Geophysics, **51**(3), 742–745.

White, R., 1992. The accuracy of estimating *Q* from seismic data: Geophysics **57**(11), 1508–1511, doi: 10.1190/1.1443218

Williams, M. L., R. F. Landel, and J. D. Ferry, 1955, The temperature dependence of relaxation mechanisms in amorphous polymers and other glass forming liquids: Journal of the American Chemical Society, **77**, 3701–3707.

Wilson, D. C. and G. L. Pavlis, 2000, Near-surface site effects in crystalline bedrock: A comprehensive analysis of spectral amplitudes determined from a dense, three-component seismic array: Earth Interactions **4**, 1−31.

Winkler, K.W. and A. Nur, 1982, Seismic attenuation: Effects of pore fluids and frictional-sliding: Geophysics **47**(1), 1−15, doi: 10.1190/1.1441276.

Wong, J., and Lines, L., 2013, Physical modeling of reflections from low-*Q* media: Can. J. Expl. Geophysics, **38**, 32–39.

Yilmaz, O., 2001, Seismic data processing: Doherty, S.M. (Ed.), Investigations in Geophysics, **1**, Soc. Exploration Geophysicists.

Zener, C., 1948, Elasticity and anelasticity of metals: University of Chicago Press.

Zhang, C., and Ulrych, T. J., 2002. Estimation of quality factors from CMP records: Geophysics **67**, 1542−1547, doi: 10.1190/1.1512799

Zhang C. and T. J. Ulrych, 2007, Seismic absorption compensation: A least squares inverse scheme: Geophysics, **72**(6), R109−R114.

Zhang Z. and R. R. Stewart, 2007, Seismic attenuation and rock property analysis in a heavy oilfield: Ross Lake, Saskatchewan: CREWES Research Report 19, 2007

Zhu, T., J. M. Carcione, and J. M. Harris, 2013, Approximating constant-Q seismic propagation in the time domain: Geophysical Prospecting, **61**, 931–940, doi: 10.1111/1365-2478.12044.

APPENDIX A

FINITE-DIFFERENCE SCHEME FOR GLS FORWARD MODELING

In this Appendix, I give a 2nd order in time and 8th order spatial finite-difference scheme for equations (3.4) and (3.5) in the text, subject to a constraint of strictly 1-D displacement **u**, as occurring within a P wave. With such a constraint and the constitutive parameter matrices in equations (4.20) and (4.24), equations (3.4) and (3.5) gives the second time derivative of the displacement field:

$$\boldsymbol{\rho}\ddot{\mathbf{u}} = -\mathbf{d}\dot{\mathbf{u}} + \left(\mathbf{K} + \frac{4}{3}\boldsymbol{\mu}\right)\mathbf{u}'' + \left(\boldsymbol{\eta}_K + \frac{4}{3}\boldsymbol{\eta}_\mu\right)\dot{\mathbf{u}}'' \ , \tag{A-1}$$

where the primes denote the spatial derivatives. Denoting the velocity field by $\mathbf{v} \equiv \dot{\mathbf{u}}$ and the elastic and viscous stress by $\boldsymbol{\sigma}$ and $\boldsymbol{\xi}$, respectively, equation A-1 becomes:

$$\begin{aligned} \boldsymbol{\rho}\dot{\mathbf{v}} &= -\mathbf{d}\mathbf{v} + \boldsymbol{\sigma}' + \boldsymbol{\xi}', \\ \dot{\boldsymbol{\sigma}} &= \left(\mathbf{K} + \frac{4}{3}\boldsymbol{\mu}\right)\mathbf{v}', \\ \boldsymbol{\xi} &= \left(\boldsymbol{\eta}_K + \frac{4}{3}\boldsymbol{\eta}_\mu\right)\mathbf{v}'. \end{aligned} \tag{A-2}$$

Using the staggered-grid finite difference (FD) method (Levander, 1988; Graves, 1996), equations (A-2) are discretized as follows:

$$\begin{aligned} \mathbf{v}_{i+1/2}^{n+1/2} &= \left[\frac{\hat{\boldsymbol{\rho}}}{\Delta t} + \frac{\hat{\mathbf{d}}}{2}\right]_{i+1/2}^{-1} \left\{\left[\frac{\hat{\boldsymbol{\rho}}}{\Delta t} - \frac{\hat{\mathbf{d}}}{2}\right]_{i+1/2} \mathbf{v}_{i+1/2}^{n-1/2} + \left[D\boldsymbol{\sigma} + D\boldsymbol{\xi}\right]_{i+1/2}^{n}\right\}, \\ \boldsymbol{\sigma}_i^{n+1} &= \boldsymbol{\sigma}_i^n + \Delta t\left[\left(\mathbf{K} + \frac{4}{3}\boldsymbol{\mu}\right)D\mathbf{v}\right]_i^{n+1/2} \ , \\ \boldsymbol{\xi}_i^{n+1} &= \Delta t\left[\left(\boldsymbol{\eta}_K + \frac{4}{3}\boldsymbol{\eta}_\mu\right)D\mathbf{v}\right]_i^{n+1/2} \ . \end{aligned} \tag{A-3}$$

In equations A-3, the subscripts denote the spatial indices of the grids and the superscript indicate the time steps. Quantities Δt and Δx (in the direction of propagation) denote the

interval of time stepping and the spatial grid spacing, respectively. The caps '^' denote the harmonic averages at adjacent points, for example:

$$\hat{\boldsymbol{\rho}}_{i+1/2} \equiv \left[\frac{1}{2} \left(\frac{1}{\boldsymbol{\rho}_{i+1}} + \frac{1}{\boldsymbol{\rho}_i} \right) \right]^{-1} . \tag{A-4}$$

The symbol D in eqs. (A-3) denotes the 8-th order discrete spatial differential operator, for example:

$$\left[D\mathbf{v} \right]_i^{n+1/2} = \frac{1}{\Delta x} \sum_{j=1}^{4} b_j \left(\mathbf{v}_{i+j-1/2}^{n+1/2} - \mathbf{v}_{i-j+1/2}^{n+1/2} \right) , \tag{A-5}$$

where the coefficients equal $b_1 = 1.1963$, $b_2 = -7.9753 \cdot 10^{-2}$, $b_3 = 9.570 \cdot 10^{-3}$, and $b_4 = -6.9754 \cdot 10^{-4}$. Extensions of this scheme to 2D and 3D are straightforward.